Development of Delayed Hydride Cracking Test Apparatus and Commissioning Tests for CANDU Fuel Bundle Assembly Welds

NWMO TR-2009-08 October 2009

Gordon K. Shek and Bogdan S. Wasiluk

Kinectrics Inc.

nwmo
NUCLEAR WASTE MANAGEMENT ORGANIZATION
SOCIÉTÉ DE GESTION DES DÉCHETS NUCLÉAIRES

Nuclear Waste Management Organization
22 St. Clair Avenue East, 6th Floor
Toronto, Ontario
M4T 2S3
Canada

Tel: 416-934-9814
Web: www.nwmo.ca

Development of Delayed Hydride Cracking Test Apparatus and Commissioning Tests for CANDU Fuel Bundle Assembly Welds

NWMO TR-2009-08

October 2009

Gordon K. Shek and Bogdan S. Wasiluk
Kinectrics Inc.

Disclaimer:

This report does not necessarily reflect the views or position of the Nuclear Waste Management Organization, its directors, officers, employees and agents (the “NWMO”) and unless otherwise specifically stated, is made available to the public by the NWMO for information only. The contents of this report reflect the views of the author(s) who are solely responsible for the text and its conclusions as well as the accuracy of any data used in its creation. The NWMO does not make any warranty, express or implied, or assume any legal liability or responsibility for the accuracy, completeness, or usefulness of any information disclosed, or represent that the use of any information would not infringe privately owned rights. Any reference to a specific commercial product, process or service by trade name, trademark, manufacturer, or otherwise, does not constitute or imply its endorsement, recommendation, or preference by NWMO.

ABSTRACT

Title: **Development of Delayed Hydride Cracking Test Apparatus and Commissioning Tests for CANDU Fuel Bundle Assembly Welds**
Report No.: **NWMO TR-2009-08**
Author(s): Gordon K. Shek and Bogdan S. Wasiluk
Company: Kinectrics Inc.
Date: October 2009

Abstract
A test apparatus was developed for performing delayed hydride cracking (DHC) tests on the assembly fuel element welds of a fuel bundle. Experimental procedures to measure the stress intensity factor (K_{IH}) for DHC initiation from the weld and the crack velocity (DHCV) were developed. A finite-element stress analysis methodology was developed to calculate the applied stress intensity factor at the weld discontinuity under the loading conditions of the experiment. Several K_{IH} and DHCV tests were successfully performed on the fuel element welds from unirradiated fuel bundles.

The following can be concluded:

(1) A test apparatus was developed and fabricated capable of measuring DHC properties such as K_{IH} and DHCV of the endplate/endcap welds of unirradiated fuel bundles.

(2) Test procedures to obtain K_{IH} and DHCV properties of the endplate/endcap welds were established.

(3) The methodology to determine the applied stress intensity factor at the weld discontinuity under the loading conditions of the DHC tests was developed.

(4) Four of the five samples tested in this program had K_{IH} values ranging from 7.6 to 8.3 MPa√m. The other sample had a K_{IH} value of 13.6 MPa√m, probably due to a difference in crack depth and the shape of the weld. The cracking mechanism was confirmed to be DHC by metallographic examination. Formation of hydrides at the crack tip was confirmed through SEM examination. Further, the response of the cracking process to temperature and the loading cycle was consistent with DHC behaviour.

(5) DHCV at 150°C of the endplate/endcap welds was found to increase after a heat-tinting cycle. DHCV ranged from 5.7×10^{-10} m/sec to 2.1×10^{-9} m/sec prior to heat-tinting and increased to 1.3×10^{-9} m/sec to 5.5×10^{-9} m/sec after the heat-tinting.

TABLE OF CONTENTS

Page

ABSTRACT ..... **v**

1. INTRODUCTION **1**

2. COMMISIONING PLAN **1**

3. TASKS IN COMMISIONING PLAN AND RESULTS **1**

3.1 DESIGN AND EVALUATION OF TESTS SAMPLES **1**
3.1.1 Source of Tests Samples 2
3.1.2 Hydrogen Concentration in Welds 2
3.1.3 Profile of Weld Discontinuity 3
3.1.4 Design of Test Sample 3
3.2 DESIGN AND FABRICATION OF TEST APPARATUS **3**
3.3 EXPERIMENTAL PROCEDURE **4**
3.3.1 K_{IH} Test Procedure 4
3.3.2 DHCV Test Procedure 5
3.4 TEST RESULTS **5**
3.4.1 Demonstration Test 5
3.4.2 K_{IH} Tests 7
3.4.3 DHCV Tests 10
3.4.4 SEM Examination of Fracture Surfaces 12
3.5 STRESS ANALYSIS METHODOLOGY AND RESULTS **13**
3.6 DISCUSSION **14**
3.6.1 Comparison with Literature Data 14
3.6.2 K_{IH} Tests on Unirradiated Zr-2.5Nb Pressure Tube Material 15

4. CONCLUSIONS **16**

ACKNOWLEDGEMENT **16**

REFERENCES **16**

APPENDIX A: NUMERICAL AND ANALYTICAL COMPUTATIONS OF STRESS INTENSITY FACTOR FOR DHC CRACK INITIATION **67**

LIST OF TABLES

Page

Table 1: "As-Received" Hydrogen Concentration in Endplate and Endplate Welds in the As-Received Conditions 18
Table 2: Results of TSSD Measurement of Hydrided Endplate Material 18
Table 3: Summary of Commissioning Tests....19
Table 4: Applied K_I in Test 07_09 Determined from Different Stress Analysis Approaches....20
Table 5: Stress Intensity Factors at Crack Initiation Computed using Finite Element Method (Model Type III-b)....20
Table 6: Stress Intensity Factors Estimated using the Analytical Approach (Method I) 21
Table 7: Comparison of K_{IH} Obtained under Load-Reduction and Increasing Load Conditions.21

LIST OF FIGURES

Page

Figure 1: Metallographic Section of a Weld Sample after the DHC Test Showing the Notch and Weld Discontinuity (The DHC Crack Deviates about 33° from the Plane of the Weld Discontinuity) (Test 07-09) 22
Figure 2: Fracture Surface on the Endcap after the DHC Test to Illustrate the Appearance of the Weld Discontinuity and Weld Spatter (Commissioning Test 07-104)....23
Figure 3: Sample for DHC Test....24
Figure 4: Drawing of DHC Test Sample which Includes the Collar for the Loading Cable and Showing the Nominal Dimensions....25
Figure 5: DHC Test Apparatus....26
Figure 6: Holding Blocks for DHC Test Sample 27
Figure 7: Design of Capping Block....28
Figure 8: Design of Backing Block. The Endplate Thickness about 1.63 mm....29
Figure 9: Photograph Showing the Sample in the Loading Rig under Load 30
Figure 10: Test Record of Demonstration Test Showing the Temperature, Load, Potential Drop (PD), and, Acoustic Emission Signals (AE) (Test 06-134)....31
Figure 11: Fracture Surface Appearance of Sample (Test 06-134)....32
Figure 12: Test Record (Commissioning Test 07-09)....33
Figure 13: Photograph of Sample Showing the Cut Location for Metallographic Sample Locations of Current and PD Leads are also Shown (Test 07-09)....34
Figure 14: Metallographic Section of Sample Showing the Weld Notch. Weld Discontinuity and DHC Crack (Test 07-09)....35
Figure 15: The Tip of the DHC Crack in the "as Polished" and "Etched" Condition Showing the Uncracked Hydride....36
Figure 16: Fracture Surface of DHC Crack of Sample (Test 07-09)....37
Figure 17: The Maximum Length of the Two DHC Crack Segments Measured from the Photograph (Test 07-09) 38
Figure 18: Test Record of DHC. The Heat-Tinting Cycle Performed at about 900 Hours (Commissioning Test 07-67) 39
Figure 19: Metallographic Section Showing the Weld Discontinuity and Hydrides along the Crack (Test 07-67) 40
Figure 20: DHC Fracture Surface of Sample (Test 07-67) 41

Figure 21: Test Record of K_{IH} Test (Test 07-104) 42
Figure 22: Fracture Surface Appearance of Sample (Test 07-104).....43
Figure 23: Test Record of K_{IH} Test (Test 07-140) 44
Figure 24: Fracture Surface of Sample from K_{IH} Test (Test 07-140).....45
Figure 25: Higher Magnification of Fracture Surface of Sample Showing the Two DHC Segments (Test 07-140) 46
Figure 26: Test Record of K_{IH} Test (Test 07-164) 47
Figure 27: Fracture Surface of Sample (Test 07-164).....48
Figure 28: Test Record of DHCV Test (Commissioning Test 07-78).....49
Figure 29: Fracture Surface Appearance of Sample (Test 07-78).....50
Figure 30: The Maximum Length of Each Crack Segment Was Measured from the Digitalized Picture (Test 07-78) 51
Figure 31: Test Record of DHCV Test (Commissioning Test 07-79).....52
Figure 32: Fracture Surface Appearance of Sample (Test 07-79).....53
Figure 33: The Maximum Length of Each Crack Segment Measured from the Digitalized Picture (Test 07-79) 54
Figure 34: Test Record of DHCV Test (Test 07-107).....55
Figure 35: Top View of Fracture Surface of Sample of DHCV Test (Test 07-107) 56
Figure 36: Side View of Fracture Surface (Test 07-107) 57
Figure 37: Test Record of DHCV Test (Test 07-113).....58
Figure 38: Fracture Surface of Sample from DHCV Test (Test 07-113).....59
Figure 39: Fracture Surface of Sample Showing the Two DHC Segments (Test 07-113) 60
Figure 40: Low Magnification SEM Micrograph of Fracture Surface on the Endplate of Sample Showing the Three Regions of Interest. Region “1” : DHC; Region “2” : Room Temperature Tearing; And Region “3”: Weld Discontinuity (Test 07-79) 61
Figure 41: Higher Magnification of the Three Regions (Test 07-79).....62
Figure 42: Higher Magnification of the Transition Region (Test 07-79) 63
Figure 43: Low Magnification SEM Micrograph of the Fracture Surface of Sample (Test 07-09) 64
Figure 44: Higher Magnification SEM Micrographs of the Different Regions of Sample (Test 07-09) 65
Figure 45: C-Shape Sample Machined from Zr-2.5Nb Pressure Tube 66

1. INTRODUCTION

The susceptibility of CANDU spent fuel bundles endplate/endcap welds to Delayed Hydride Cracking (DHC) while in long term dry storage is being assessed. In order to establish whether DHC is operative at the endplate/endcap welds, material properties such as the stress intensity factor (K_{IH}) for DHC initiation and delayed hydride crack velocity (DHCV) are required.

Kinectrics was awarded a contract by the Nuclear Waste Management Organization (NWMO) to develop a test apparatus and methodology to measure the required properties for DHC initiation at the bundle endplate/endcap welds. A commissioning plan by Shek (2007) for the DHC evaluation program was developed with the main objective of obtaining information which can be applied to testing irradiated materials. The plan included information about the design of the test samples, design of test apparatus and crack monitoring methodology, stress analysis methodology, design of DHC test procedures, post-test fracture surface examination, and interpretation of test record and data. In addition, the DHC properties of the welds in the unirradiated conditions would be determined.

A status report by Shek (2007) was issued on November 1, 2007 documenting progress of work to the end of July, 2007. This final report is an extension of the status report and includes the results of additional K_{IH} and DHCV tests, examination of the fracture surface of two samples by scanning electron microscopy as well as results from tests on Zr-2.5Nb pressure tube samples to validate the K_{IH} test procedure used for the endplate-to-endcap welds. The findings are discussed in Section 4. This report follows the structure and format of the status report with new information added where appropriate.

2. COMMISIONING PLAN

For the purpose of this report, the commissioning plan can be broken into several tasks.

(1) Design and evaluation of test samples.
(2) Design and fabrication of test apparatus.
(3) Design and establishment of test procedure.
(4) Performing commissioning tests on unirradiated endplate/endcap welds.
(5) Developing stress analysis methodology.
(6) Performing verification tests and establishing an acceptance criterion.

Results of each of these tasks are given in Section 3.

3. TASKS IN COMMISIONING PLAN AND RESULTS

3.1 DESIGN AND EVALUATION OF TESTS SAMPLES

3.1.1 Source of Tests Samples

Most of the test samples were obtained from an intact full size 37-element CANDU fuel bundle manufactured by Canadian General Electric Inc. to the usual manufacturing standards but without UO_2 fuel pellets included in the fuel elements. Also, the bundle does not have a serial number or a document for traceability. In addition to this full size bundle, a “single-endplate empty bundle”, also without UO_2 pellets, was available to get additional endplate/endcap welds for testing. This bundle has endplate on only one end, welded to the fuel elements. The elements on the other end are “loose” without an endplate. The single-endplate bundle has a serial number GE-L22222C stamped on the end-plate. Elements from the single-endplate empty bundle were used for hydrogen concentration measurements and weld characterization, as well as for the demonstration test and one K_{IH} test to be described in Section 3.4.

3.1.2 Hydrogen Concentration in Welds

In order for DHC to occur, the welds must have sufficient hydrogen for hydrides to form at the flaw tip. Two coupons from the assembly welds and one coupon from the endplate of the “single-endplate bundle” (GE-L22222C) were cut by a small wheel cutter from the single-endplate bundle for TSSD (Terminal Solid Solubility for hydride Dissolution) temperature measurements by differential scanning calorimetry (DSC). This method measures the temperature at which all the hydrides in the sample are dissolved. The hydrogen concentration can then be estimated from the TSSD equation in AECL Report (1991) which relates concentrations to the dissolution temperatures. After the TSSD temperature measurements, the hydrogen concentration of the coupons was measured by hot extraction analysis to verify the results from the DSC measurements.

The data are shown in Table 1 which indicates that the hydrogen concentration of the welds and endplate was about 10 ppm by weight. It should be noted that the TSSD equation is based on Zr-2.5Nb pressure tube material and may not be identical to that of the Zircaloy weld or endplate. In order for DHC to occur at 150ºC without being affected by hydrogen concentration, the hydrogen concentration should be higher than the TSSP (Terminal Solid Solubility for hydride Precipitation) concentration at 150°C of about 14 ppm, based on the Fitness-For-Service Guidelines (FFSG) by AECL (1991) TSSP equation for Zr-2.5Nb material. Although, DHC can still occur at 150ºC at hydrogen concentration lower than 14 ppm, the K_{IH} and DHCV values may be different than the samples with higher hydrogen concentration.

The assembly welds on one end of the full bundle were hydrided by the electrolytic hydriding/thermal diffusion technique to a target hydrogen concentration of 40 ppm. This is well in excess of the TSSP concentration of 14 ppm. Hydrogen in excess of 14 ppm will remain as bulk hydrides during the DHC tests and should have no significant effect on the DHC process. In this hydriding procedure, a solid hydride layer was deposited electrolytically on the surfaces at the end of the bundle submerged in a 0.1 Molar sulphuric acid electrolyte. The hydrogen was then diffused into the metal matrix from the hydride layer at the TSSD temperature of about 270°C for 40 ppm hydrogen for about 48 hours. After the diffusion anneal, the hydrogen concentration in the hydrided material was determined by DSC measurement of the TSSD temperature. The result is shown in Table 2 which indicates that the target hydrogen concentration of 40 ppm was achieved. The remnant of the hydride layer was left on the bundle. This should have no impact on the DHC test results as the peak temperature in the DHC thermal cycle does not exceed the TSSD temperature of the 40 ppm samples.

3.1.3 Profile of Weld Discontinuity

In order to calculate the K_I at the weld discontinuity, which is treated as an initiating crack, the depth and profile of the weld discontinuity need to be determined. This can be done by metallographic examination (and/or fractography) to determine the dimensions of the notch and weld discontinuity. Figure 1 is a metallographic section of the weld prepared after a K_{IH} test (details of the K_{IH} test will be provided in Section 3.4). The depth of the notch formed between the endplate and endcap and the depth of the weld discontinuity can be measured from the micrograph and used as input to calculate the applied K_I in the DHC test. It should be noted that in order to obtain the proper depths of the notch and weld discontinuity for K_I calculation, the metallographic section should be taken at a location near the middle of the weld.

Figure 2 shows an example of a DHC crack of a commissioning test to be described in Section 3.4. The diameter of the weld and the combined depth of the notch and weld discontinuity can be determined from the side-view of the fracture surface. Figure 2 also shows the presence of weld spatter on the endcap surface. However, the spatter does not appear to affect the depth of the notch and weld discontinuity or the load-bearing area.

3.1.4 Design of Test Sample

The test sample is designed to have the weld region loaded in bending in a cantilever loading system. In the K_{IH} tests, both the bending stress and applied K_I for DHC initiation will be determined. Figure 3 shows a test sample taken from the outer ring of the intact 37-element GE fuel bundle used in one of the commissioning tests described in Section 3.4. Figure 4 is a drawing of the sample showing the nominal dimensions and the distance from the loading collar to the weld. The sample consists of a portion of a single element with the weld assembly and endplate cut from the fuel bundle. The endplate has a nominal linear length of about 22 mm. The sample shown in Figure 4 has an overall length of about 76.8 mm. This length can be modified, depending on the design of the loading arrangement. For the irradiated fuel elements, an extension arm can be used to achieve the appropriate length if they were cut close to the endcap to facilitate removal of the fuel pellets.

3.2 DESIGN AND FABRICATION OF TEST APPARATUS

Figure 5 shows a schematic diagram of the test apparatus which consists of the loading rig, furnace for heating, crack monitoring system using both acoustic emission and direct current potential drop, and data acquisition and control system.

For the loading rig design, the sample is anchored by gripping the endplate strip between two machined blocks connected by threaded bolts (Figure 6). The capping block (Figure 7) has a 1 mm thick portion which goes into the gap between the endplate and spigot of the element so that the sample can be anchored close to the weld. The capping block was made with 17-4PH Stainless Steel. The backing block (Figure 8), which was made with 300 series stainless steel, has a machined groove for placing the endplate strip. Backing blocks with different machined grooves can be made to accommodate elements with different endplate strips (strip with different curvatures, widths or straight strip). The backing block is in turn supported in a platform through a threaded bolt and nut. The connection at the platform can be designed to

allow rotation of the sample holding blocks such that one can select the portion of the weld region under tensile bending stress. Figure 5 shows the support platform located inside the furnace. The support platform is anchored by a bolt through the furnace. The test apparatus can be designed to have the support platform outside of the furnace if a smaller oven is used to enclose the sample only.

Figure 9 shows that the sample is loaded by pulling up on the fuel element through a steel cable placed around a groove in an aluminum collar attached to the fuel element. This produces a tensile bending stress in the lower part of the weld. The pull rod is connected to a load cell and an actuator, controlled by a stepper-motor. The loading system is designed with a relatively short lever arm (e.g. 28.68 mm in the illustration shown in Figure 4) to avoid having a large bending moment at the weld. It should be noted that the loading system can be designed to pull down on the fuel element, in which case the top part of the weld will be under tensile bending stress.

Heating is provided by a furnace with a programmable temperature controller. The allowable temperature fluctuation in the isothermal K_{IH} or DHCV tests is ± 2ºC from the target temperature. Crack initiation and growth is monitored by acoustic emission and direct current potential drop techniques simultaneously. A wave guide is used to transmit the acoustic emission signals to the transducer outside of the oven. For the potential drop crack detection and monitoring system, microvolt resolution is required to detect cracking. A constant current of 3-4 amperes was used in the d.c. potential drop (PD) monitoring (location of current and PD leads will be shown in Section 3.4). The acoustic emission system is capable of detecting the breaking of a 0.5 mm H pencil lead when the background noise is low. It should be pointed out that the test procedure is designed to have continued crack growth after initiation, which would be easier to detect than just crack initiation.

The sample temperature, applied load, acoustic emission counts and potential drop voltages are monitored and recorded with a computerized data acquisition system.

3.3 EXPERIMENTAL PROCEDURE

This section provides the general test procedures for K_{IH} and DHCV tests. More specific details will be provided in Section 3.4 on the commissioning tests.

3.3.1 K_{IH} Test Procedure

The K_{IH} tests were performed under increasing load conditions, which is different than the more common load-reduction K_{IH} test procedure on Zr-2.5Nb pressure tube material. In the increasing load test procedure, the applied K_I is increased in small steps at regular time interval until cracking is detected. In the decreasing load test procedure, cracking is initiated at a load higher than K_{IH}, the load is reduced in steps until no cracking was detected in sufficient waiting time (such as two days for a test temperature of 150°C). For the decreasing load tests, the crack shape at the end of the test needs to meet certain requirements in order to provide a valid K_I calculation. For the endplate weld, crack growth may deviate from the plane of the weld discontinuity and hence it will be difficult to determine K_I using the load-reduction test procedure.

For the increasing load K_{IH} test, the sample is loaded to a nominal K_I below the estimated K_{IH} value, heated to a temperature of at least 60ºC above the test temperature at about 1-2ºC/minute and held for 1 hour, and then cooled at about 1-2ºC/minute to the specified test temperature (e.g. 150ºC) for cracking to occur. The 60°C difference between the peak and test temperature was chosen in order to obtain optimum level of hydrogen concentration in solution at the test temperature, as this is larger than the hysteresis between TSSD and TSSP temperatures, If no cracking is detected in about 50 hours, the applied load is increased by 5% and held for another 50 hours for cracking to initiate. This process is repeated until cracking is detected. After cracking has been detected, the load is maintained to obtain DHC crack growth for about 100 hours or more. The sample is then unloaded. A heat-tinting cycle (nominally at 200ºC for 5 hours) is performed to mark the DHC crack. K_{IH} is calculated by using the applied load at crack initiation and post-test measurement of the depth of the notch and weld discontinuity. Crack velocity can be calculated from the measured crack length and cracking time determined from the crack monitoring system. It should be pointed out that DHCV may be lower at a K_I level which is only slightly above K_{IH}. Nevertheless, the data can be compared to those from the DHCV tests obtained at higher applied K_I.

Depending on the results, the test parameters such as the initial applied K_I, amount of load increase in each step, duration of waiting interval, crack growth time and heat-tinting conditions may be modified for the testing on either subsequent unirradiated samples or irradiated samples.

3.3.2 DHCV Test Procedure

For the DHCV tests, the sample is loaded to an initial estimated K_I about 30% higher than the K_{IH} value. The sample is then heated to at least 60ºC above the test temperature, held for 1 hour and then cooled to the target test temperature of 150°C for DHC to occur. After DHC initiation is detected, the crack should be allowed to grow for about 0.5 mm or longer, based on an estimated crack velocity or by potential drop calibration. The DHC crack should be heat-tinted to facilitate measurement of the crack length. Crack velocity is determined by measuring the crack length from post-test examination, divided by the cracking time determined from the potential drop record.

3.4 TEST RESULTS

Three types of commissioning tests were formed in this test program: (1) demonstration test to show that the unirradiated endplate welds have sufficient yield strength for DHC to occur, (2) K_{IH} test and (3) DHCV tests. Results of these tests are described in the following sub-sections.

3.4.1 Demonstration Test

One sample was tested to demonstrate that DHC can occur in the endplate-to-endcap welds in unirradiated samples.

<u>Test 06-134</u>: This test was performed on the weld of element # 8 of the single-endplate bundle (GEL22222C) containing 10 ppm hydrogen. The element number was based on the standard numbering system of GE bundles. The objectives of the test were: (1) to demonstrate whether the unirradiated welds have sufficient strength for DHC to occur and (2) to serve as a pilot test

for subsequent commissioning tests to assess the sample design, test apparatus and procedure. The test procedure was not designed to measure K_{IH} under increasing load condition. The starting K_I was about 13.9 MPa√m which is expected to be higher than the K_{IH} value. The applied load to obtain the target K_I was based on the analytical method described in Appendix A using a nominal crack depth of 0.5 mm.

Figure 10 shows the records of load, temperature, acoustic emission and potential drop of Test 06-134. The acoustic emission output was given in voltage and 10 volts corresponded to 1000 of accumulative acoustic emission counts. For temperature monitoring, one thermocouple (P3) was placed at the sample near the weld and another thermocouple (P6) was placed at the sample holding block. The temperatures registered by the two thermocouple were similar. The potential drop (PD) increased with increasing temperature as a result of increase in material electrical resistance. At a constant temperature, an increase in PD was indicative of crack growth. The sample was first heat-tinted at 250°C for about 3 hours without load to mark the initial weld discontinuity. The heat-tinting thermal cycle also served to approach the test temperature by cooling. The sample was then loaded to about 100 N which corresponds to a K_I of 13.9 MPa√m or a nominal bending stress of 264 MPa at the weld location (refer to Section 3.5 and Appendix A for details of the calculation) and then cooled to the test temperature of about 130°C. There was an apparent steady increase in PD voltage a few hours after reaching the test temperature. However, no changes in acoustic emission (AE) signals were observed. The load was increased by about 10% at 100 hours. The PD continued to increase at a steady rate but there was no significant AE signal. In an attempt to obtain information on K_{IH}, the load was reduced in steps of about 5% every 100 hours or so to determine the load at which DHC stopped. The potential drop record indicated that cracking appeared to stop temporarily after each load reduction and then re-started. This is consistent with the DHC behaviour observed in Zr-2.5Nb pressure tube material in which a period of incubation time is required to re-start cracking after a load-reduction as discussed by Coleman et al. (1990). This is due to the presence of residual stress at the crack tip after a load-reduction. The incubation time is required to form a larger hydrided region at the crack tip for cracking to continue. Once cracking has advanced beyond the crack tip region with residual stress, the normal DHC behaviour resumes. Figure 10 indicates that cracking did not stop completely (i.e. did not reach K_{IH}) after a number of load-reductions. The DHC test was terminated at 600 hours and the load was reduced to about 15 N. A heat-tinting cycle was performed by heating to 200°C for about 6 hours to mark the DHC crack.

The endplate strip was peeled off from the weld to expose the crack surface. Figure 11 shows the fracture surface on the endcap viewed from above and from the side. There were two zones of oxidized fracture surfaces, one represents the weld discontinuity and the other one represents the DHC crack. The DHC fracture surface appears to be “rougher” than the typical DHC crack in Zr-2.5Nb pressure tube material. This could be due to the difference in texture and microstructure of the two materials. It is expected that the Zircaloy weld would have more random texture and fewer reoriented hydrides in the crack path. The side view of the crack indicated that it grew at about 30° from the plane of the weld discontinuity into the weld region of the endplate.

Table 3 summarizes the results of Test 06-134. It is concluded that DHC can occur in the unirradiated endplate welds. It should be possible to perform K_{IH} and DHCV tests using the sample design and test apparatus described in Section 3.3. However, it is noted that cracking can be detected by the potential drop technique but not by the acoustic emission technique.

3.4.2 K_{IH} Tests

Five K_{IH} tests were performed: one at 130°C on the sample with 10 ppm hydrogen and four at 150°C on the 40 ppm samples. All tests were performed on the endplate-to-endcap welds of the fuel elements in the outer ring of the fuel bundle. In addition to obtaining the K_{IH} values, DHCV values were also obtained from these tests. However, it should be noted that the DHCV obtained at low applied K_I (just about K_{IH}) may be lower than that obtained at higher applied K_I in the standard DHCV tests.

Test 07-09: This test was performed at 130°C on the weld of element # 6 of the single-endplate bundle containing about 10 ppm hydrogen. Figure 12 shows the records of load, temperature, acoustic emission and potential drop of Test 07-09. The sample was heated to 250°C to mark the weld discontinuity and then cooled to the test temperature at 130°C. A load of about 45 N was applied which was equivalent to roughly 8 MPa√m, assuming a crack depth of 0.5 mm. No cracking was detected by either PD or AE after about 70 hours. The load was increased in steps of 5% in 40-50 hours interval. It was observed that the PD started to increase at a load of 65 N. However, the increase in PD was sluggish at this load level. After increasing the load in steps to 78 N at 460 hours, the increase in PD became steady. To be conservative, the lower load of 65 N was used to calculate K_{IH} in the stress analysis of this test. Cracking continued until about 750 hours when the temperature was increased to 200°C to mark the DHC crack and to see whether cracking could be arrested. No cracking was detected during the 120 hours hold at 200°C.

This is consistent with the DHC behaviour in zirconium alloys in which tests have shown that cracking cannot occur above a certain temperature, T_{DAT} (DAT stands for Direction of Approach to Temperature), when approached by heating as reported by Ambler (1984). This is due to the TSS hysteresis in which the TSSP (for precipitation) concentration is significantly higher than the TSSD (hydride dissolution) concentration. When approached by heating to the test temperature above T_{DAT}, the hydrogen concentration at the crack tip cannot reach TSSP concentration and therefore DHC cannot occur. T_{DAT} depends on a number of parameters such as yield strength, applied K_I and previous cool-down temperature. T_{DAT} is in the range of 200°C for unirradiated Zr-2.5Nb pressure tube material. It is likely that T_{DAT} of the Zircaloy welds is lower than that of the pressure tube material because of the lower strength and more random texture.

DHC resumed (according to the PD response) when the temperature was lower to 130°C (see Figure 12). Interestingly, there were also AE activities for a short duration, as indicated in the discrete jumps in acoustic events (which were converted to voltage signals, as shown in Figure 12). However, it is not readily apparent what mechanism might have triggered them. One possible scenario is that some larger reoriented hydrides might have been formed at the crack tip region during cooling from 200°C to 130°C under stress. Subsequent cracking of these larger hydrides were detected by AE. Further work is required to verify this postulation. Once the DHC crack has advanced into steady growth at 130°C, the cracking was not detected by AE. Referring to Figure 12, the applied load was reduced by 20% at 1000 hours. The objective of the load reduction was to stop the cracking and form a larger uncracked hydrided region at the crack tip for metallographic examination. Cracking did stop as indicated by the PD which was unchanged after the load reduction. Testing was terminated after about 75 hours at the reduced load level.

After the DHC test, the sample was prepared for metallographic examination. The sample was sectioned in a slow speed diamond wheel cutter. Figure 13 shows the sectioned sample (and the locations of current and PD leads on the sample). The piece containing the weld was mounted and ground to the weld region. The section was then polished with 9 μm diamond paste. A mirror-like surface finish was obtained by attack polishing in slurry of abrasive burnt ammonium dichromate ashes with the addition of a small amount of dilute hydrofluoric acid. The sample was first examined in the as-polished condition. The hydrides were then revealed either by chemical etching in a solution containing nitric acid: lactic acid: hydrofluoric acid (45:45:4 volume ratio) or by anodizing in a solution of 60 ml ethanol, 35 ml distilled water, 20 ml glycerine, 10 ml lactic acid, 5 ml phosphoric acid and 2 ml nitric acid at a voltage of about 110 V.

Figure 14 shows the metallographic section in the anodized condition. In this plane, the DHC crack appeared to initiate at the weld discontinuity about 0.17 mm from the notch formed between the end plate and endcap. The crack grew at an angle of about 33° from the weld discontinuity into the weld region of the endplate. Figure 15 shows the tip of the DHC crack in the as-polished and chemically etched conditions at higher magnification. A small uncracked hydride about 20 µm long was present at the crack tip. This hydrided region was likely formed during the 75 hours hold at 130°C under reduced load at the end of the DHC test (refer to Figure 12).

After metallographic examination, the sample was removed from the mount. The endplate was peeled and ground off from the weld. Figure 16 shows the fracture surface on the weld cap and endplate (Note: the micrograph of the endcap also indicates the location of the metallographic section in the weld region). The two segments of DHC before and after the heat-tinting at 200°C can be distinguished from the difference in oxide color. The maximum length of each crack segment was measured from the fracture surface of the endplate (Figure 17). The photograph was taken roughly normal to the DHC fracture surface, based on visual examination. These were used to calculate the DHCV along with the cracking time determined from the potential drop record. For the second crack segment obtained after the heat-tinting, it is assumed that there is no incubation time for cracking to resume after the heat-tinting.

The K_{IH} value was determined to be 8.3 MPa√m following the procedure described in detail in Section 3.5. The DHCV for the two crack segments were 4.7×10^{-10} m/sec and 5.4×10^{-10} m/sec. Results of the K_{IH} and DHCV are summarized in Table 3.

<u>Test 07-67</u>: This test was performed on the weld of element # 2 of the full bundle hydrided to nominally 40 ppm hydrogen. The K_{IH} test was performed at 150°C.

Figure 18 shows the records of load, temperature, acoustic emission and potential drop of Test 07-67. The sample was subjected to a preconditioning cycle by heating to about 218°C for an hour, prior to cooling to the test temperature at 150°C (It should be noted that the weld discontinuity has already been oxidized during the hydriding procedure). The sample was then loaded to 50 N. No cracking was detected by the PD after about 40 hours. The load was increased by about 5% every 40 hours. The PD started to increase slowly at an applied load of 62 N, which was used to calculate K_{IH} in the stress analysis. There were no AE signals detected. The load was increased a few times by 2.5% as there was uncertainty whether the PD was increasing steady. Crack growth was continued to about 840 hours and the DHC crack was marked by subjecting the sample to a heat-tinting cycle at 220°C. Crack growth resumed after the temperature was lowered to 150°C and the test was terminated at about 1200 hours.

Similar to Test 07-09, the sample was prepared for metallographic examination of the crack path and hydrides. Figure 19 shows the weld discontinuity and the DHC crack in the etched condition at two magnifications. The crack grew into the weld region of the endplate at about 30° from the weld discontinuity. This is similar to that observed in Test 07-09. The high magnification micrograph shows the presence of hydrides along the crack path and at the tip, as well as the microstructure of the weld in the background.

After metallographic examination, the sample was removed from the mount and the endplate strip was peel off and ground to reveal the fracture surface. For this particular sample, the endplate and weld region was severely deformed during the peeling process. This resulted in more material being ground off from the weld. Figure 20 shows the fracture surface which appeared to have only one crack segment. It is likely that the second crack segment formed after the heat-tinting might have been removed by the grinding process.

Results for the K_{IH} (7.7 MPa√m) and DHCV (2.5 x 10^{-10} m/sec) values at 150°C are summarized in Table 3. The DHCV value was obtained from the crack length measured from the metallographic section shown in Figure 19 which included the crack segments before and after heat-tinting, divided by the total cracking time before and after the heat-tinting as determined from the potential drop record.

Test 07-104: This test was performed on the weld of element # 13 of the full bundle hydrided to nominally 40 ppm hydrogen. The K_{IH} test was performed at 150°C.

Figure 21 shows the records of load, temperature, acoustic emission and potential drop of Test 07-104. The sample had similar test history and behaviour as that of Test 07-67, with the crack initiating at an applied load of 62 N. The heat-tinting cycle to 230°C was applied at about 480 hours. Figure 22 shows the fracture surface appearance of the two DHC crack segments, before and after the heat-tinting.

The K_{IH} of this sample was determined to be 7.9 MPa√m and the DHCV was 6.8 x 10^{-10} m/sec and 2.3 x 10^{-9} m/sec before and after the heat-tinting. The results are summarized in Table 3.

Test 07-140: This test was performed on the weld of element # 15 of the full bundle hydrided to nominally 40 ppm hydrogen. The K_{IH} test was performed at 150°C.

Figure 23 shows the records of load, temperature, acoustic emission and potential drop of Test 07-140. The sample had similar test history and behaviour as that of the other K_{IH} tests. Cracking was initiated at an applied load of 62 N. Figure 24 shows the fracture surface appearance, viewed from the top and from the side. A higher magnification of the crack surface is shown in Figure 25, which shows the two DHC segments.

The K_{IH} of this sample was determined to be 7.6 MPa√m and the DHCV was 2.1 x 10^{-10} m/sec and 4.0 x 10^{-10} m/sec before and after the heat-tinting. The results are summarized in Table 3.

Test 07-164: This test was performed on the weld of element # 8 of the full bundle hydrided to nominally 40 ppm hydrogen. The K_{IH} test was performed at 150°C.

Figure 26 shows the records of load, temperature, acoustic emission and potential drop of Test 07-164. Cracking appeared to initiate at an applied load of 62 N, which showed an increase in

potential drop as well as acoustic signals. However, the potential drop increase was sluggish and the load was increased to 65 N. Steady increase in potential drop occurred at this higher load level, as well as presence of some acoustic events. The heat-tinting was performed at about 380 hours. The rate of potential drop increase was higher after the heat-tinting, similar to that observed in the other tests.

Figure 27 shows the fracture surface appearance, viewed from the top and from the side. Two features are different from the samples of other K_{IH} tests. The first one is that the combined depth of the notch and weld discontinuity of about 0.85 mm was much larger than the values of 0.51-0.54 mm of the other K_{IH} test samples. The other difference was that the crack shape of Test 07-164 was more ovalized and deviated more from the idealized circular shape, compared to the crack shape of the other K_{IH} tests.

The K_{IH} of this sample was determined to be 13.6 MPa√m and the DHCV was determined to be 6.6×10^{-10} m/sec and 2.1×10^{-9} m/sec before and after the heat-tinting. The results are summarized in Table 3. The higher K_{IH} value was due to the larger crack depth and possibly treating the ovalized weld as an idealized circular weld. It should be pointed out that the microstructure of the weld region is homogeneous. The tip of a deeper crack may be in a location with a microstructure different than that of a shorter crack, which may affect the K_{IH} properties. An interesting point about the test is that acoustic emission was able to detect cracking, which may be due to the formation of larger hydrides as a result of the higher applied K_I.

<u>Summary of K_{IH} Tests</u>: Results of the K_{IH} tests are summarized in Table 3. Four of the five samples had K_{IH} values ranging from 7.6 to 8.3 MPa√m. This scatter in K_{IH} properties is considered to be small, compared to that obtained from Zr-2.5Nb pressure tube material. However, the fifth sample had a K_{IH} value of 13.6 MPa√m, which is significantly higher than those of the other test samples. This could be due to a longer initial combined depth of the notch and crack, which may result in the crack initiating at a region with a different microstructure. Ovality of the weld region may have also contributed to the higher K_{IH} value, as the K_I calculation is based on an idealized circular weld.

3.4.3 DHCV Tests

Four DHCV tests were performed at 150°C. Two were performed on the welds of the outer ring elements from the full bundle hydrided to 40 ppm hydrogen. The other two tests were performed on the welds of the intermediate elements in the intermediate ring next to the outer ring (hereafter identified as the intermediate ring) of the full bundle with 40 ppm hydrogen.

<u>Test 07-78</u>: This test was performed on the weld of element # 4 in the outer ring. The test was performed at 150°C, following the procedure described in Section 3.3.2.

Figure 28 shows the test record of Test 07-78. The sample was loaded to 80 N which should produce an applied K_I higher than the K_{IH} value. The sample was heated to 220°C and then cooled to 150°C for DHC to occur. Cracking appeared to initiate with only about 1-2 hours of incubation time, as indicated by the increase in PD. It was noted that there were some AE activities for a short duration. Cracking continued at a steady rate at the same applied load until the heat-tinting cycle at 115 hours. The potential drop record indicated that the velocity was greatly reduced (or cracking stopped completely) when the temperature was raised to

210°C. Cracking resumed when the temperature was restored to 150°C. The DHCV appeared to be higher after the thermal cycle, based on the rate of potential drop increase.

Figure 29 shows the fracture surface of the DHC crack viewed from the top and from the side. The side view of the DHC crack indicated that the crack grew at about 30° from the plane of weld discontinuity into the endplate, which is consistent with the other samples. The two segments of DHC crack are clearly shown by the difference in oxide color. The maximum length of the DHC cracks in the two segments was measured, as shown in Figure 30. The photograph was taken normal to the fracture surface.

Table 3 shows the velocity of the two crack segments determined from dividing the crack length by the cracking time obtained from the potential drop record. The results show that the crack velocity increased from 2.1×10^{-9} m/sec to 4.0×10^{-9} m/sec after the heat-tinting thermal cycle. One possible mechanism for the increase in DHCV was an increase in hydrogen in solution as a result of the thermal cycle. However, further work is required to determine the exact causes for the increase in DHCV after heat-tinting.

Test 07-79: The DHCV was performed at 150°C on the weld of element # 6 on the outer ring containing 40 ppm hydrogen.

Figure 31 shows the test record of Test 07-79. The sample was loaded to 80 N, heated to 220°C for an hour and then cooled to 150°C. After an incubation time of about 15 hours at 150°C, the PD started to increase. At the same time, there were some AE activities for a short duration. The incubation time in this test was much longer than those in Test 07-08. The large variability in initiation time for DHC initiation is not uncommon as it depends on the local condition at the flaw tip. The PD increased at a steady rate until the heat-tinting cycle at 168 hours. There was no PD increase during the period at 230°C for heat-tinting. It should be noted that the heat-tinting temperature was higher than that the 210°C used in Test 07-78, as cracking may not have completely stopped at 210°C. Cracking resumed when the temperature was restored to 150°C with a higher rate of PD increase.

Figure 32 shows the fracture surface viewed from above and from the side. The features were similar to that of Test 07-78. The two segments of DHC crack were clearly visible from the difference in oxide color. The maximum length of the two segments of DHC crack was measured, as shown in Figure 33.

Table 3 shows the velocity of the two crack segments obtained by dividing the crack lengths by the cracking time from the potential drop record. The results show that the crack velocity increased from 1.8×10^{-9} m/sec to 5.5×10^{-9} m/sec after the heat-tinting thermal cycle.

Test 07-107: The DHCV test was performed at 150°C on element # 21 of the second ring. It was noted that the endplate of the second ring was narrower than that of the outer ring.

Figure 34 shows the test record. The sample was loaded to about 73 N which produced noticeably more deflection of the sample when compared to the samples taken from the outer ring. This is likely due to the smaller weld resulting in higher bending stress. Cracking appeared to occur shortly after cooling to 150°C from the initial peak temperature at 220°C. After about 231 hours of cracking, the sample was given a heat-tinting thermal cycle before obtaining a second DHC crack segment at 150°C.

Figure 35 shows the fracture surfaces on both the endcap and endplate. A side view of the crack surface is shown in Figure 36. It is noted that the DHC crack did not initiate at region "A" (refer to Figure 35) which lied at the 6 o'clock position and should be subjected to the highest bending stress. However region "A" appeared to have been deformed during the welding process, which likely would have discouraged DHC initiation. Instead, the DHC cracks initiated from both sides adjacent to the deformed region. The maximum length of the DHC crack in the two stages of crack growth was measured for calculating the DHCV. The DHCV was determined to be 6.6×10^{-10} m/sec and 1.3×10^{-9} m/sec before and after the heat-tinting thermal cycle. The applied K_I was not determined because of the irregular crack initiation locations.

Test 07-113: The DHCV test was performed at 150°C on element # 26 of the second ring. Figure 37 shows the test record which is similar to that of Test 07-107. The same applied load of 73 N was used in this test and cracking initiated at 150°C with little incubation time. The sample was subjected to a heat-tinting thermal cycle at about 380 hours.

Figure 38 shows the fracture surface of the DHC cracks, which initiated on both sides adjacent to the deformed region of the weld. Figure 39 is a higher magnification of the DHC crack viewed normal to the fracture surface. The maximum crack lengths were measured from the micrograph and used for the DHCV calculation. The DHCV was determined to be 5.7×10^{-10} m/sec and 1.4×10^{-9} m/sec before and after the heat-tinting thermal cycle.

Summary of DHCV Tests: Results of the DHCV tests are summarized in Table 3. In general, DHCV increased after the heat-tinting cycle and the DHCVs measured from the welds in the second ring were lower than those from the outer ring. This could be due to the more extensive deformation and irregular crack growth of the welds in the second ring. Based on the results from the DHCV tests from the welds of the outer and second rings, DHCV at 150°C ranged from 5.7×10^{-10} m/sec to 2.1×10^{-9} m/sec prior to the heat-tinting. The DHCV range increased to 1.3×10^{-9} m/sec to 5.5×10^{-9} m/sec after the heat-tinting. As it is expected that the spent fuel bundles would not be subjected to a temperature cycle as that of the heat-tinting cycle during the long term storage, it is reasonable to use the DHCV data prior to the heat-tinting for DHC assessment.

3.4.4 SEM Examination of Fracture Surfaces

Two of the DHC test samples were selected for more detailed examination of the fracture surface by scanning electron microscopy (SEM). One of the objectives of the examination is to provide additional evidence that the cracking process was by delayed hydride cracking. The other objective is to confirm that DHC initiation occurred at the region where the crack deviated from the plane of the weld discontinuity. In other words, there was no DHC occurring in the weld discontinuity.

Samples from Test 07-79 (DHCV test) and Test 07-09 (K_{IH} test) were used for the SEM examination.

Test 07-79: This was a DHCV test performed at 150°C on the weld of element # 6 of the full bundle containing 40 ppm hydrogen. Figure 40 shows the fracture surface on the endplate side and the three regions of interested labelled as "1", "2" and "3". Region "1" was the DHC crack based on the examination in the stereo-microscope. Region "2" was the region tore apart at

room temperature to expose the DHC crack. Region “3” was the fracture surface of the weld discontinuity.

A higher magnification of the fracture surface of region “1” is shown in Figure 41a. The fracture surface consists mainly of cleavage fracture, indicative of a brittle fracture mechanism such as fracturing of the re-oriented hydrides. Figure 41b shows the fracture surface in region “2”. The fracture surface consists of both ductile region represented by the dimple features and region of cleavage brittle appearance. The ductile regions resulted from tearing of the metal matrix at room temperature. The brittle region could be from fracturing of the bulk hydrides distributed throughout the weld which contained 40 ppm hydrogen. Figure 41c shows region “3” at higher magnification. The fracture surface of the weld discontinuity has a granular appearance and has no brittle features, indicating there was no hydride cracking. Figure 42a is a fractograph showing the transition region between the weld discontinuity and the DHC crack. The transition was very distinct suggesting that DHC initiated at the boundary where the crack started to deviate from the plane of the weld discontinuity. Figure 42b shows the transition region between the weld discontinuity and the room temperature tearing, which indicates that ductile behaviour occurred adjacent to the weld discontinuity.

Test 07-09: This was a K_{IH} test performed at 130°C on the weld of element # 6 of the single-endplate bundle containing about 10 ppm hydrogen.

Figure 43 is a low magnification SEM micrograph of the fracture surface on the endcap. Region “1” was the DHC crack. Region “2” was resulted from room temperature tearing (most of this region has been removed by grounding). Region “3” was the weld discontinuity.

Higher magnification of the three regions is shown in Figure 44. Similar features to that of the sample from Test 07-79 were observed on this sample.

Summary of SEM Examination: It is concluded that the crack initiated and grew by a brittle fracture process, characteristic of that of hydride fracture via a DHC mechanism. The DHC initiated from the region of the weld discontinuity at the location where cracking started to deviate from the plane of the weld discontinuity into the endplate weld.

3.5 STRESS ANALYSIS METHODOLOGY AND RESULTS

This section provides a summary on the development of the stress analysis methodology to calculate the applied stress intensity factor K_I for crack initiation from the weld discontinuity in the DHC experiments. Details on the stress analysis are provided in Appendix A.

The stress analysis methodology uses both analytical and finite element analyses to determine the stress intensity factor K_I at the weld discontinuity as a function of an applied bending load. As described in Appendix A, in the analytical analysis, the sample was modeled as a cantilever rod with a fully circumferential crack. Two solutions for K_I available from the open literature were used.

For the finite element analysis, two approaches were taken to model the end of the fuel element. In a simplified approach (model “a”), boundary conditions which constrain displacement in the axial direction but allow fuel element and weld ovalization, were applied at the end of the element. In a more detailed approach (model “b”), the boundary conditions

included the endplate at the end of the fuel element. Since the analysis is linear-elastic, local deformation of the fuel element shell under the applied load would not affect the K_I value. In both approaches, four levels of complexity (Model I to IV) with increasing closeness to the actual sample geometry were analyzed. Model I analyzed a circumferential crack in a rod. Model II analyzed a circumferential crack in an endcap with uniform diameter. Model III analyzed a circumferential crack in an endcap with geometry closer to that of the actual sample (having a tapered portion). Model IV analyzed the circumferential crack at the root of a notch which is the closest to the actual sample geometry. However, the finite element modeling does not consider crack closure caused by the compressive bending stress at lower portion of the specimen. The crack closure, if present, would increase the load carrying capacity of the component and hence decrease the applied effective tensile stress.

For Test 07-09 described in detail in Appendix A, the applied K_I at crack initiation was determined using all these different approaches and the results are summarized in Table 4 The K_{IH} value obtained from finite element analysis Model IV-b was considered to be the closest corresponding to the test configuration. However, the results obtained from Model IV-b and Model III-b were close. For the other K_{IH} and DHCV tests, Model III-b was used to determine the applied K_I at crack initiation because of less time required for mesh generation.

Results of the loading conditions including bending stress and K_I for the commissioning tests described in Section 3.4 are summarized in Table 5. It should be noted that the dimensions of the crack depth and weld diameter may differ from that shown in the figures on the experimental results by a fraction of a decimal point, because some dimensions were re-measured and provided for stress analyses. These small differences in crack depth and weld diameter will not affect the calculated K_I values. The applied nominal and net-section bending stresses were computed using the analytical cantilever beam model. For the demonstration test (Test 06-134), the applied K_I was calculated using the analytical method only and the results are summarized in Table 6.

3.6 DISCUSSION

The following approaches were used to verify the tests: (1) compare test results to data from the open literature, and, (2) measure the K_{IH} from Zr-2.5Nb pressure tube samples with known K_{IH} value using similar test apparatus and load increasing test procedure.

3.6.1 Comparison with Literature Data

The K_{IH} values of irradiated Zircaloy electron beam welds were reported by Schofield et al. (2002) to be 8-12 MPa√m. Therefore, the results obtained from this test program appear to be reasonable.

The authors are not aware of DHCV data on zircaloy welds in the open literature. The DHCV of cold worked unirradiated Zr-2.5Nb pressure tube material has a lot of scatter, due to material variability and measurement uncertainties. In one set of tests by Simpson and Puls (1979), the DHCV of a pressure tube in the axial direction was reported to be in the range of 8-9 x 10^{-9} m/sec. It is likely that the Zircaloy weld may have lower DHCV than the cold worked Zr-2.5Nb pressure tube material because of the difference in yield strength and texture. Hence, the range of DHCV obtained in this test program also appears to be reasonable.

It should be pointed out, however, that the DHCV values reported in the open literature are based on measuring the average crack length over the entire sample width. In this test program, the DHCV values of the welds were obtained using the maximum crack length.

3.6.2 K_{IH} Tests on Unirradiated Zr-2.5Nb Pressure Tube Material

As discussed in Section 3.3.1, the K_{IH} data on the welds were obtained using an increasing load procedure. This is different than the more commonly used load-reduction K_{IH} test procedure for Zr-2.5Nb pressure tube material, in which a large K_{IH} database exists. The objective of this task is to show whether the K_{IH} values depend on the loading procedure.

Two C-shape samples (Figure 45), machined from an unirradiated pressure tube section hydrided to a nominal hydrogen concentration of 60 ppm, were used for this evaluation. The C-shape samples were tested under tensile loading through the machined pin holes in a loading frame similar to that used for the DHC tests on the fuel element welds. Cracking was monitored using the same potential drop system. When loaded under uniaxial loading through the pin holes, the K_I expression for the C-shape sample with a crack is given in ASTM E-399 (1994) as follows:

$$K_I = \frac{P}{B\sqrt{W}}\left[3\frac{X}{W} + 1.9 + 1.1\frac{a}{W}\right]\left[1 + 0.25\left(1 - \frac{a}{W}\right)^2\left(1 - \frac{r_1}{r_2}\right)\right] f\left(\frac{a}{W}\right) \qquad \text{(1a)}$$

where K_I = stress intensity factor

$$f\left(\frac{a}{W}\right) = \frac{\sqrt{\frac{a}{W}}}{\left(1 - \frac{a}{W}\right)^{3/2}}\left[3.74 - 6.30\left(\frac{a}{W}\right) + 6.32\left(\frac{a}{W}\right)^2 - 2.43\left(\frac{a}{W}\right)^3\right] \qquad \text{(1b)}$$

P = load
r_1/r_2 = ratio of inner to outer radii

a, W, B and X are defined in Figure 45.

For each C-shape sample, K_{IH} was first obtained at 200°C using the load-reduction procedure. As stated in the Section 3.3.1, cracking was first initiated from the machined notch at an applied K_I higher than the expected value of K_{IH}, the load was then reduced in small steps until no cracking was detected by the potential drop in at least 48 hours. After K_{IH} was reached, the load was increased to increase the K_I value by increments of 1 MPa√m until cracking was re-initiated. Thus, two K_{IH} values were obtained for each sample. The first value was obtained under load-reduction procedure while the second value was obtained under load-increase conditions.

Results of the K_{IH} tests on these two samples are summarized in Table 7. For Test 07_161, the K_{IH} obtained under load-reduction was 8.3 MPa√m. Cracking was re-initiated in the first load increment to 9.3 MPa√m. The K_{IH} value under increasing load conditions may have been lower

than 9.3 MPa√m if a small load increment was used. Similar results were obtained from Test 07_160 which has a K_{IH} value of 7.7 MPa√m under load-reduction conditions and cracking re-initiated in the first increment to 8.7 MPa√m. These results confirmed that the difference in K_{IH} values obtained under load-reduction and load-increasing procedures are nearly identical.

4. CONCLUSIONS

(1) A test apparatus was developed and fabricated which is capable of measuring DHC properties such as K_{IH} and DHCV of the endplate-to-endcap welds of the unirradiated fuel bundle.

(2) The test procedures for obtaining K_{IH} and DHCV properties of the endplate-to-endcap welds were established.

(3) The methodology to determine the applied stress intensity factor at the weld discontinuity under the loading conditions of the DHC tests was established.

(4) Four of the five samples tested in this program had K_{IH} values ranging from 7.6 to 8.3 MPa√m. The other sample had a K_{IH} value of 13.6 MPa√m, probably due to a difference in crack depth and the shape of the weld.

(5) DHCV at 150°C of the endplate-to-endcap welds was found to increase after a heat-tinting cycle. DHCV ranged from 5.7×10^{-10} m/sec to 2.1×10^{-9} m/sec prior to the heat-tinting. The DHCV range increased to 1.3×10^{-9} m/sec to 5.5×10^{-9} m/sec after the heat-tinting.

ACKNOWLEDGEMENT

The authors thank Mr. H. Seahra for providing technical support in the experimental program, Mr. T. Lampman of NSS and Dr. J. Freire-Canosa of NWMO for providing helpful discussion throughout the program.

REFERENCES

AECL CANDU, Sheridan Park Research Community. 1991. Fitness-for-Service Guidelines for zirconium alloy pressure tubes in operating CANDU reactors, COG Report No. COG-91-66. Toronto, Ontario.

Ambler, J.F.R. 1984. Effects of direction of approach to temperature on delayed hydride cracking behaviour of cold worked Zr-2.5 Nb, Zirconium in the Nuclear Industry: Sixth International Sym. STP 824, pp. 653-674.

ASTM E399-90. 1994. Standard test method for plane-strain fracture toughness of metallic materials. Annual Book of ASTM Standards, American Society for Testing and Materials.

Coleman, C.E., S. Sagat,, G.K Shek, D.B. Graham and M.A. Durand. 1990. Locating a leaking crack and safe stimulation, International Journal of Pressure Vessels and Piping, Vol. 43, pp. 187-204.

Schofield, J.S., E.C. Darby and C.F. Gee. 2002. Temperature and hydrogen concentration limits for delayed hydride cracking in irradiated zircaloy, Zirconium in the Nuclear Industry: Thirteen International Symposium, ASTM STP 1423, pp. 339-357.

Shek, G. K. February 2007. Commissioning plan for the development of test equipment and procedure for the measurement of DHC properties of the fuel bundle assembly welds, Memorandum prepared by Kinectrics Inc. for Ontario Power Generation, Kinectrics Document No. K-013119-010-TM-0001-R00. Toronto, Ontario.

Shek, G. K. October 2007. Status on the development of DHC test apparatus and commissioning tests of the fuel bundle assembly welds, Memorandum prepared by Kinectrics Inc. for Ontario Power Generation, Kinectrics Document No. K-013119-010-TM-0002-R0. Toronto, Ontario.

Simpson, L.A. and M.P. Puls. 1979. The effects of stress, temperature and hydrogen content on hydride-induced crack growth in Zr-2.5Nb, Metall. Trans. A, 10A, 1093-1105.

Table 1: "As-Received" Hydrogen Concentration in Endplate and Endplate Welds in the As-Received Conditions

Sample ID	Sample Location	TSSD Temp. (^oC)	Estimated Hydrogen Concentration from TSSD Equation* (wt. ppm)	Measured Hydrogen Concentration by Hot Vacuum Extraction Method (wt. ppm)
K-013119-GE-L2222C-PENCIL-16	Element 16 weld	182	9	10
K-013119-GE-L2222C-PENCIL-24	Element 24 weld	176	8	10
K-013119-GE-L2222C-ENDPLT-LOC-29	Endplate	176	8	9

*FFSG for Zr-2.5Nb pressure tube: TSSD = 81900 exp (-34500/RT)

Table 2: Results of TSSD Measurement of Hydrided Endplate Material

Sample ID	TSSD Temp. (^oC)	Estimated Hydrogen Concentration from TSSD Equation (ppm)
013119_DHC_TEST_07_67_ENDPLATE	270	39.3

Table 3: Summary of Commissioning Tests

Test ID	Type of Test	H Conc. (ppm)	Test Temp. (°C)	Maximum Nominal Bending Stress at Crack Initiation (MPa)	K_I for DHCV Test or K_{IH} (MPa√m)	DHCV (m/sec)		Comments
						Before Heat-Tinting	After Heat-Tinting	
06_134	Demo. test	10	130	264*	13.9*	NA	NA	DHC can occur in the unirradiated welds.
07_09	K_{IH} test	10	130	184*	8.3**	4.7E-10	5.4E-10	Two DHC crack segments before and after heat-tinting thermal cycle.
07_67	K_{IH} test	40	150	163*	7.7**	2.5E-10***	NA	
07_104	K_{IH} test	40	150	167*	7.9**	6.8E-10	2.3E-09	
07_140	K_{IH} test	40	150	170*	7.6**	2.1E-10	4.0E-10	
07_164	K_{IH} test	40	150	155*	13.6**	6.6E-10	2.1E-9	Deeper initial crack.
07_78	DHCV	40	150	214*	11.8**	2.1E-9	4.0E-9	
07_79	DHCV	40	150	209*	12.2**	1.8E-9	5.5E-9	
07_107	DHCV	40	150	193*	NA	6.6E-10	1.3E-9	Weld from second ring; irregular crack growth due to deformed region.
07_113	DHCV	40	150	198*	NA	5.7E-10	1.4E-9	Weld from second ring; irregular crack growth due to deformed region.

* Approximated from analytical method I.
** Obtained from finite element analysis using model III-b.
*** DHCV was determined by the dividing the total crack length (from metallography) and the total crack time of the two crack segments before and after heat-tinting.

Table 4: Applied K_I in Test 07_09 Determined from Different Stress Analysis Approaches

FE Model	J [N/mm]	K_I [MPa√m]
Model I-a	0.887	10.0
Model I-b	0.538	7.8
Model II-a	0.893	10.0
Model II-b	0.543	7.8
Model III-a	0.962	10.4
Model III-b	0.610	8.3
Model IV-a	0.962	10.4
Model IV-b	0.575	8.0

Table 5: Stress Intensity Factors at Crack Initiation Computed using Finite Element Method (Model Type III-b)

(Refer to Table 3 for Hydrogen Concentrations and Test Temperatures)

Test	Notch Crack Depth [mm]	End Cap Diameter [mm]	Loading Force [N]	Bending Moment [N mm]	Nominal Moment of Inertia [mm^4]	Maximum Nominal Bending Stress [MPa]	Maximum Net Section Bending Stress [MPa]	Stress Intensity Factor K_I [MPa√m]
07_09	0.51	4.70	65.5	1878.5	23.95	184	384	8.3
07_67	0.54	4.81	62.0	1778.2	26.28	163	349	7.7
07_78	0.61	4.78	80.0	2294.4	25.63	214	518	11.8
07_79	0.64	4.82	80.0	2294.4	26.50	209	527	12.2
07_104	0.54	4.77	62.0	1778.2	25.41	167	361	7.9
07_140	0.51	4.74	62.0	1778.2	24.78	170	352	7.6
07_164	0.85	4.89	62.0	1778.2	28.07	155	558	13.6
07_107	0.55	4.79	72.7	2085.0	25.84	193	423	N/A
07_113	0.74	4.75	72.7	2085.0	24.99	198	607	N/A

Table 6: Stress Intensity Factors Estimated using the Analytical Approach (Method I)

Test	Crack Depth [mm]	End Cap Diameter [mm]	Loading Force [N]	Bending Moment [N mm]	Nominal Moment of Inertia [mm^4]	Maximum Nominal Bending Stress [MPa]	Maximum Net Section Bending Stress [MPa]	Stress Intensity Factor K_I [MPa√m]
06_134	0.50*	4.80	100.0	2868.0	26.06	264	532	13.9

*Estimated value.

Table 7: Comparison of K_{IH} Obtained under Load-Reduction and Increasing Load Conditions

Test #	Sample #	Pressure Tube ID	Hydrogen Concentration (ppm)	Test Temperature (°C)	K_{IH} Obtained by Load-Reduction (MPa√m)	K_{IH} Obtained by Increasing Load (MPa√m)
07_161	180-1	Offcut 146B	60	200	8.3	9.3*
07_160	0-2	Offcut 146B	60	200	7.7	8.7*

*Cracking initiated in the first load-increment of 1 MPa√m after the load-reduction test.

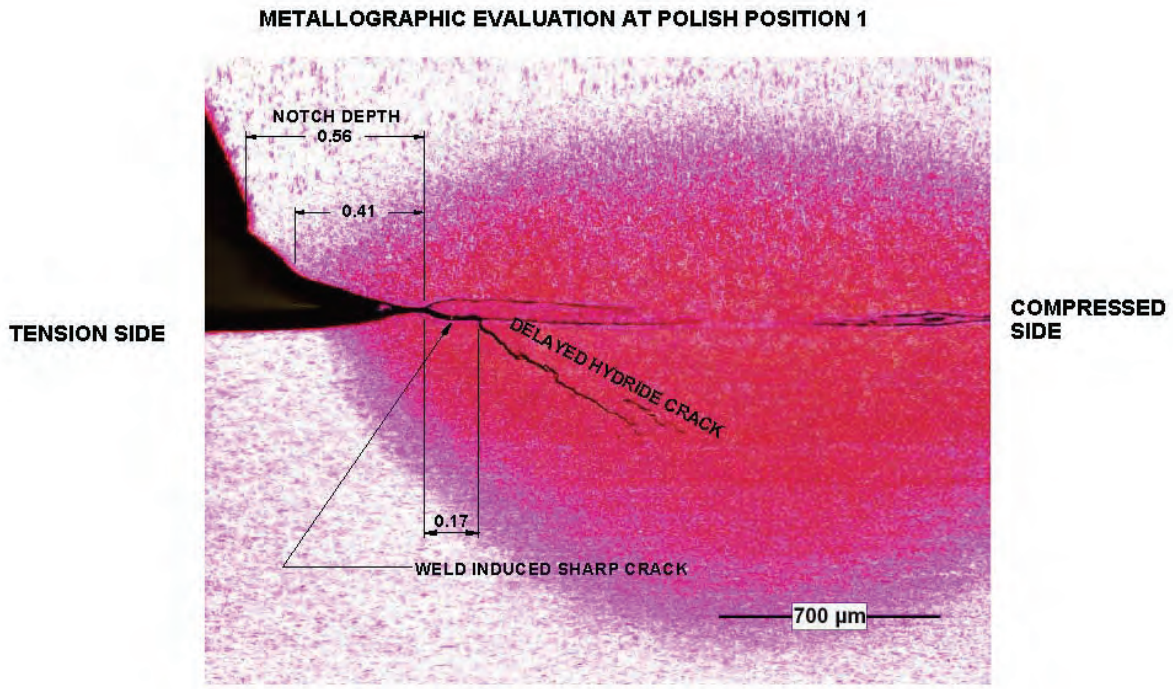

Figure 1: Metallographic Section of a Weld Sample after the DHC Test Showing the Notch and Weld Discontinuity (The DHC Crack Deviates about 33° from the Plane of the Weld Discontinuity) (Test 07-09)

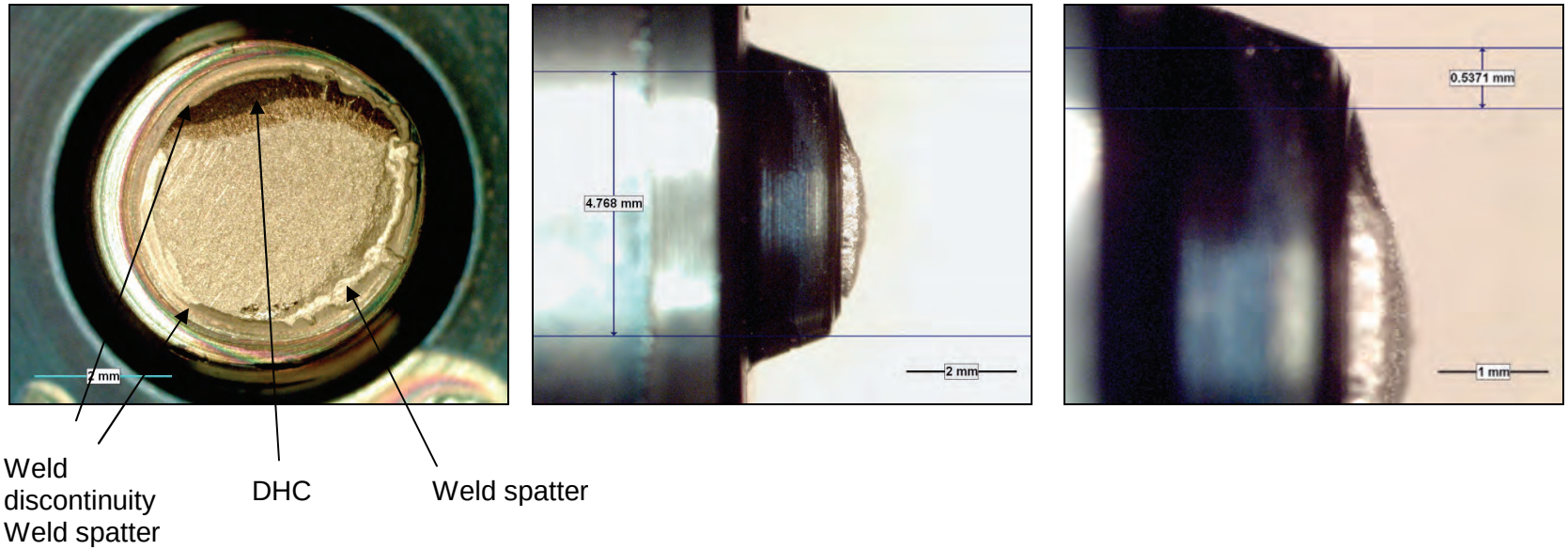

Top view of DHC crack on endcap

Side-view showing the weld diameter

Side-view showing the combined notch and crack depth

Figure 2: Fracture Surface on the Endcap after the DHC Test to Illustrate the Appearance of the Weld Discontinuity and Weld Spatter (Commissioning Test 07-104)

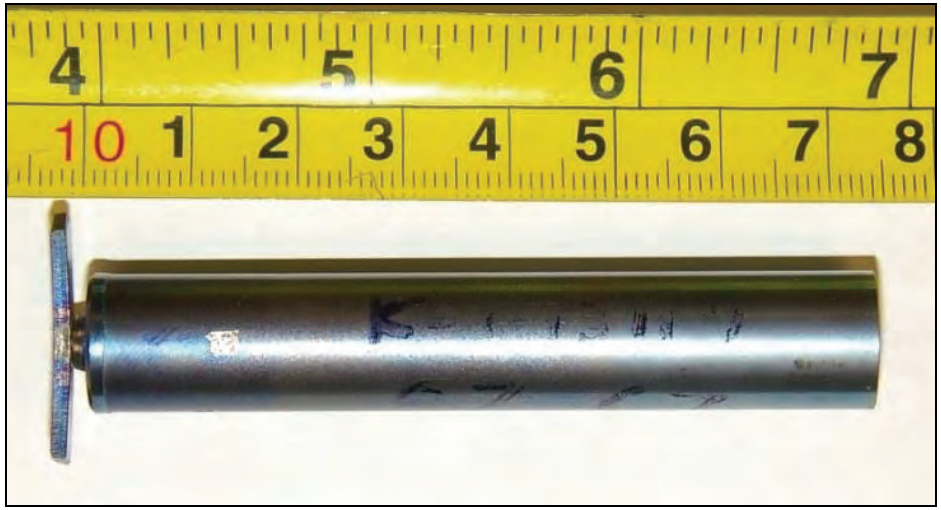

Side view

End view

Figure 3: Sample for DHC Test

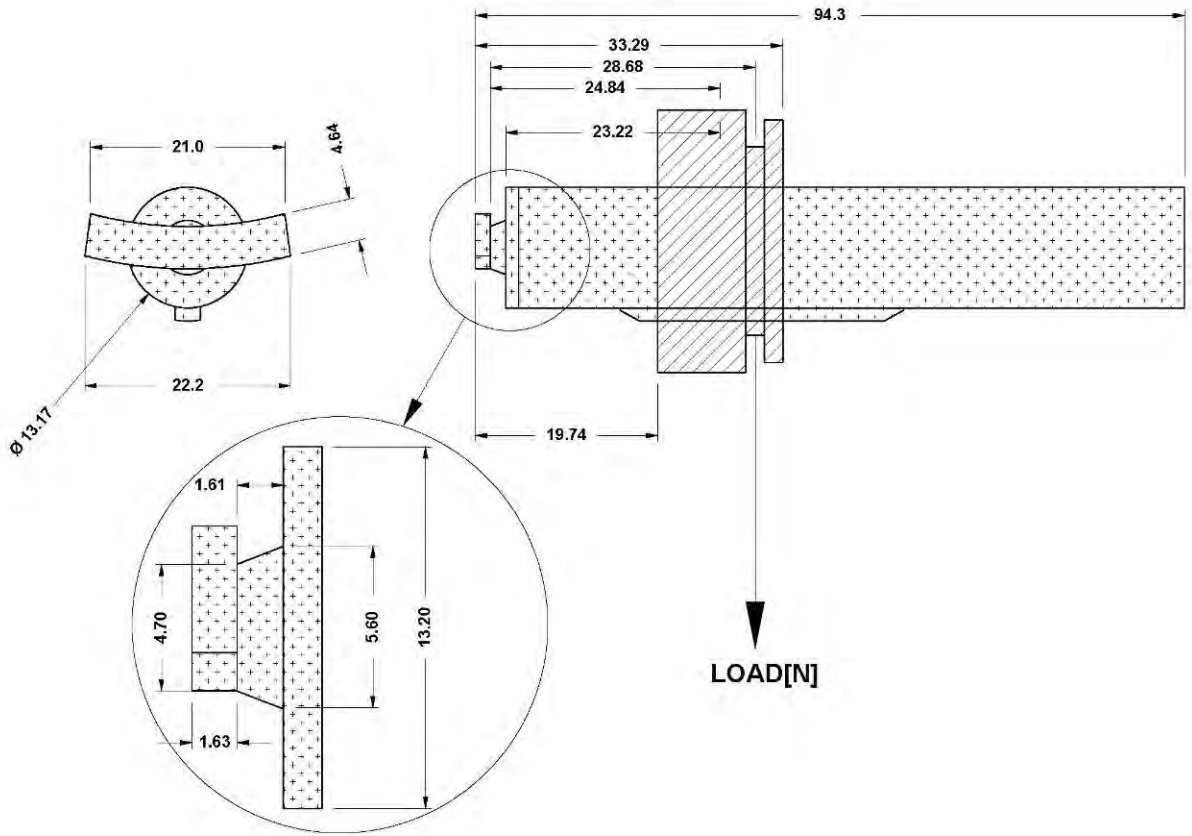

Note: In this illustration, the lever arm distance from the centre of the collar to the weld discontinuity is 24.94 mm. The endplate thickness is about 1.6 mm. The loading is applied by pulling down on the collar.

Figure 4: Drawing of DHC Test Sample which Includes the Collar for the Loading Cable and Showing the Nominal Dimensions

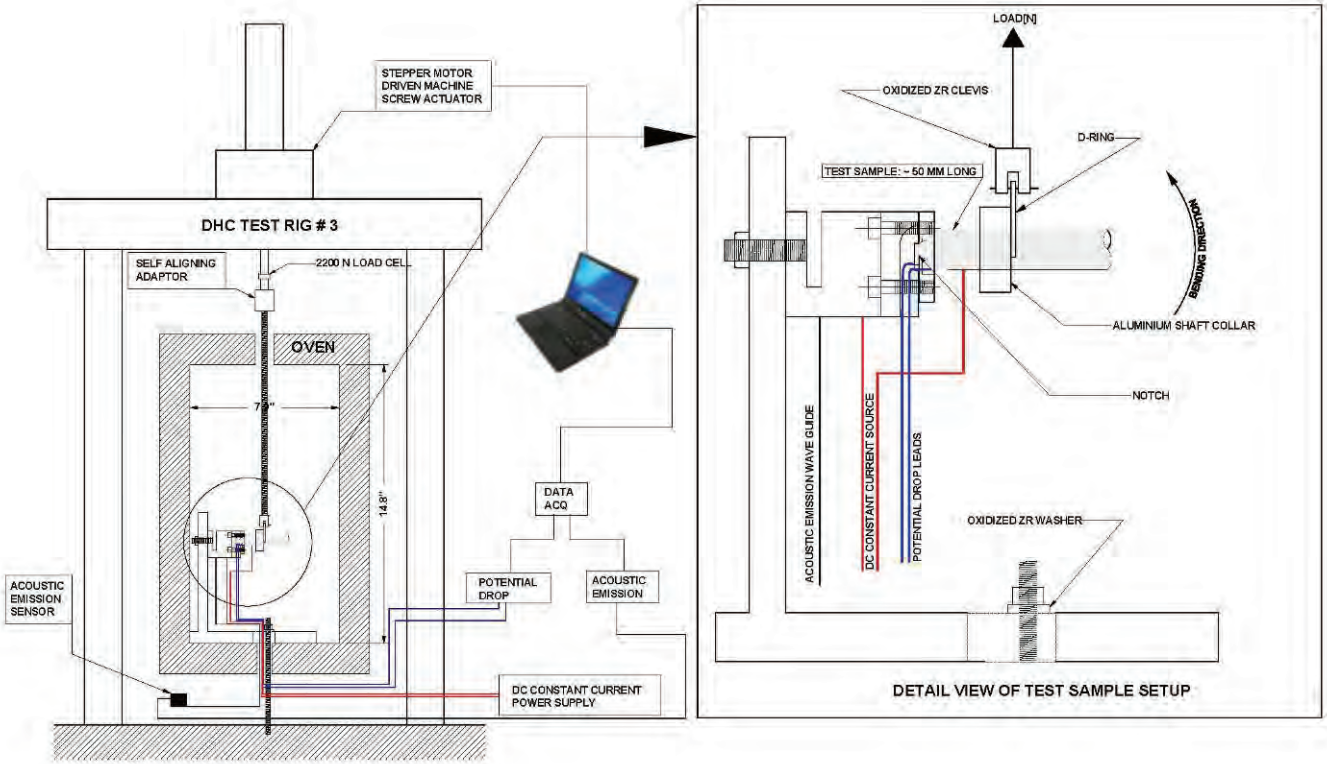

Figure 5: DHC Test Apparatus

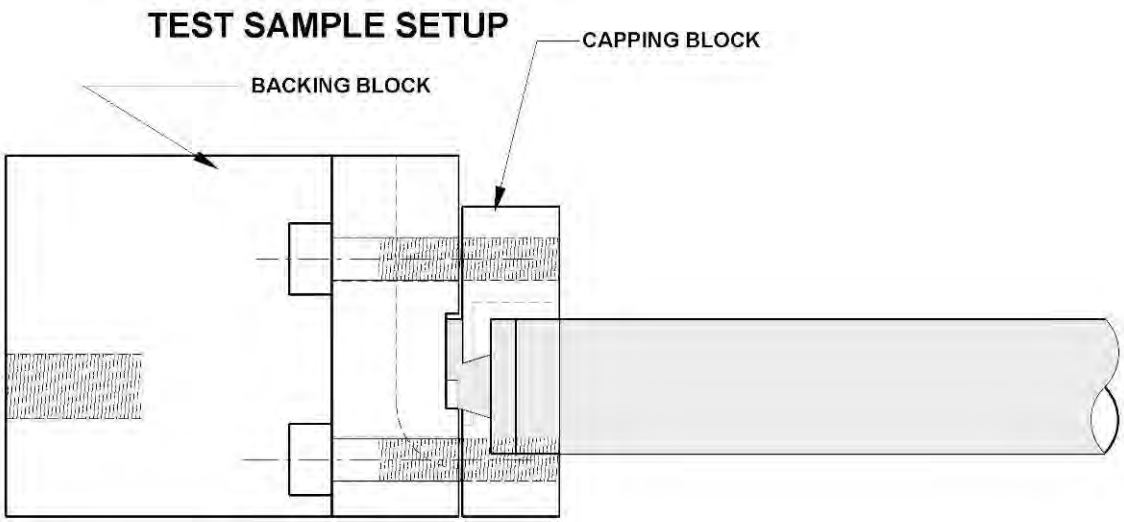

Figure 6: Holding Blocks for DHC Test Sample

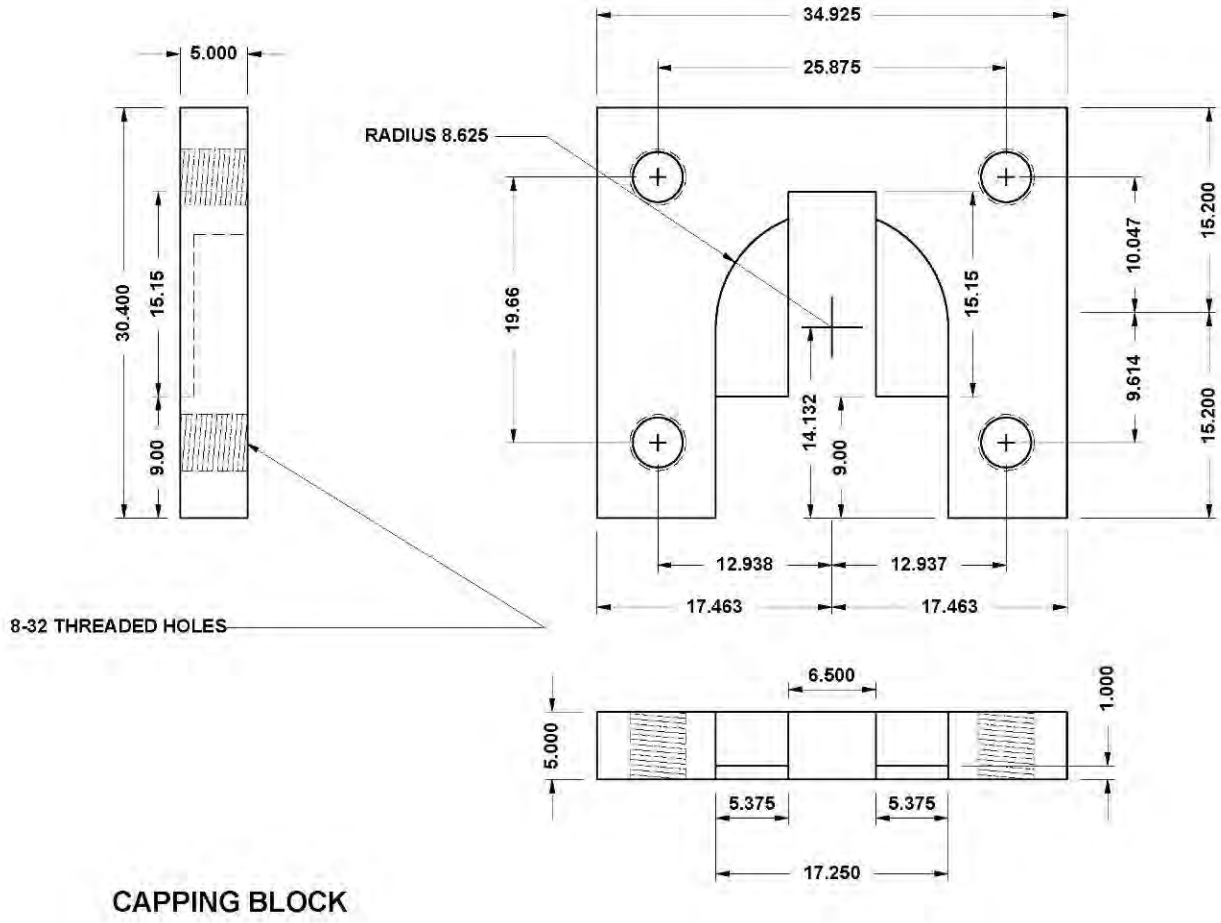

Figure 7: Design of Capping Block

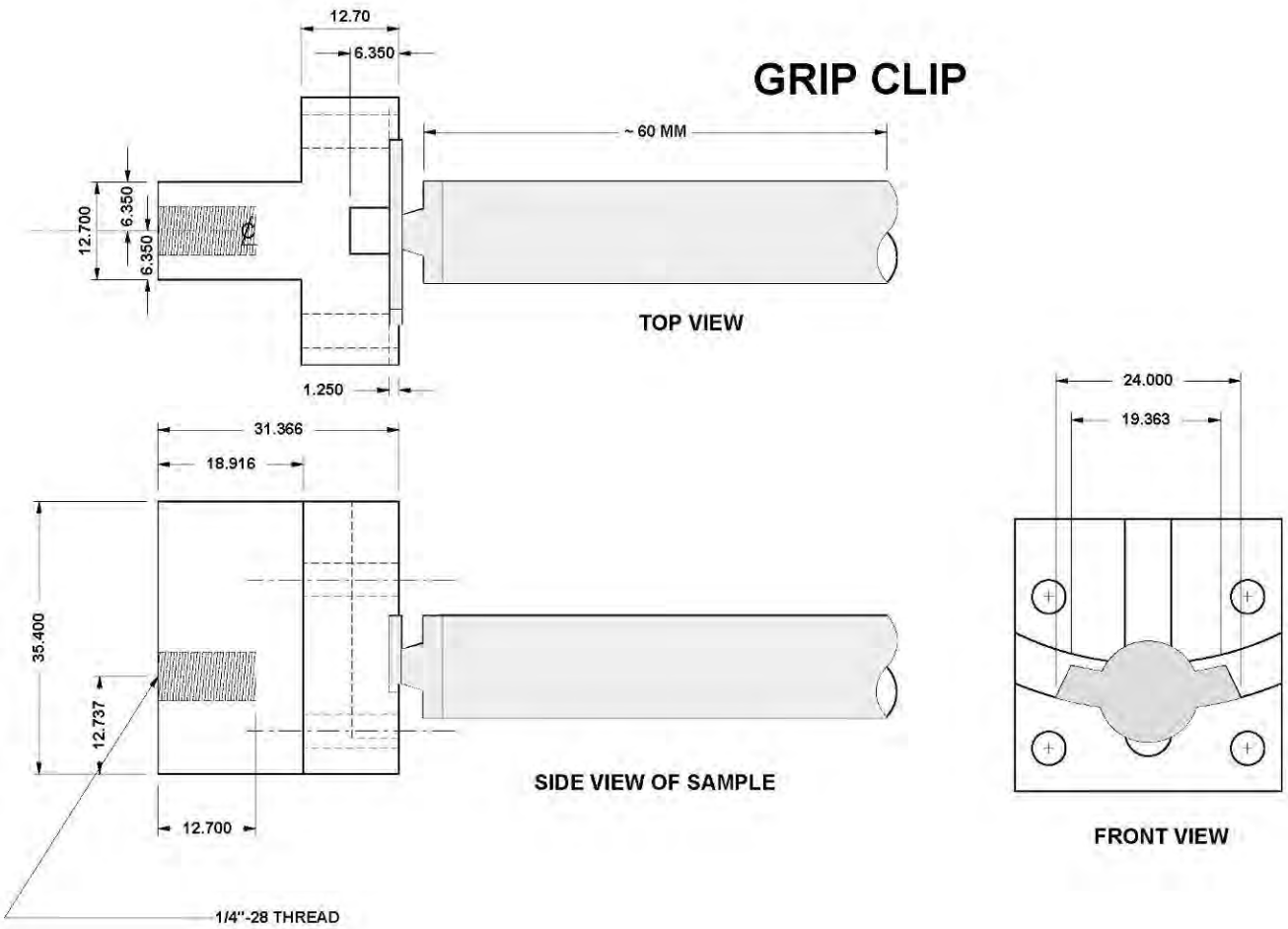

Figure 8: Design of Backing Block. The Endplate Thickness about 1.63 mm

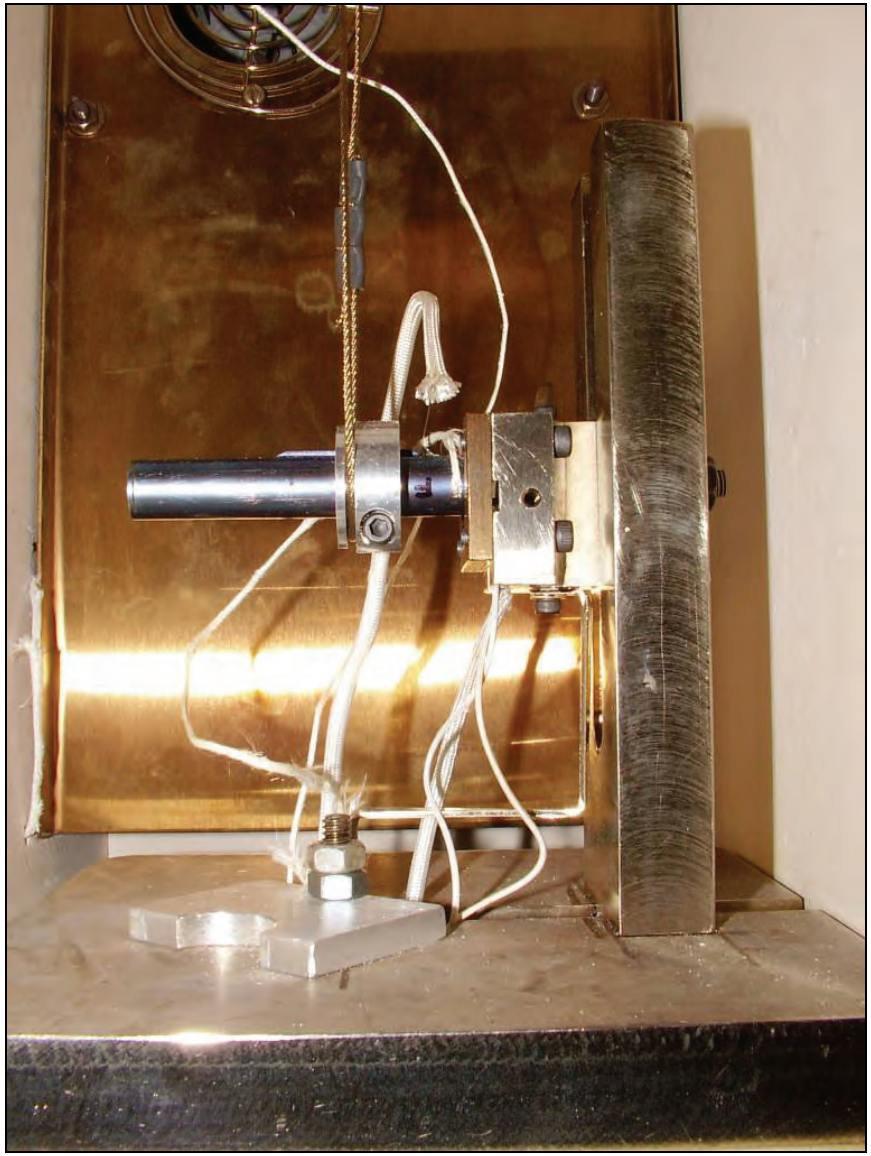

Figure 9: Photograph Showing the Sample in the Loading Rig under Load

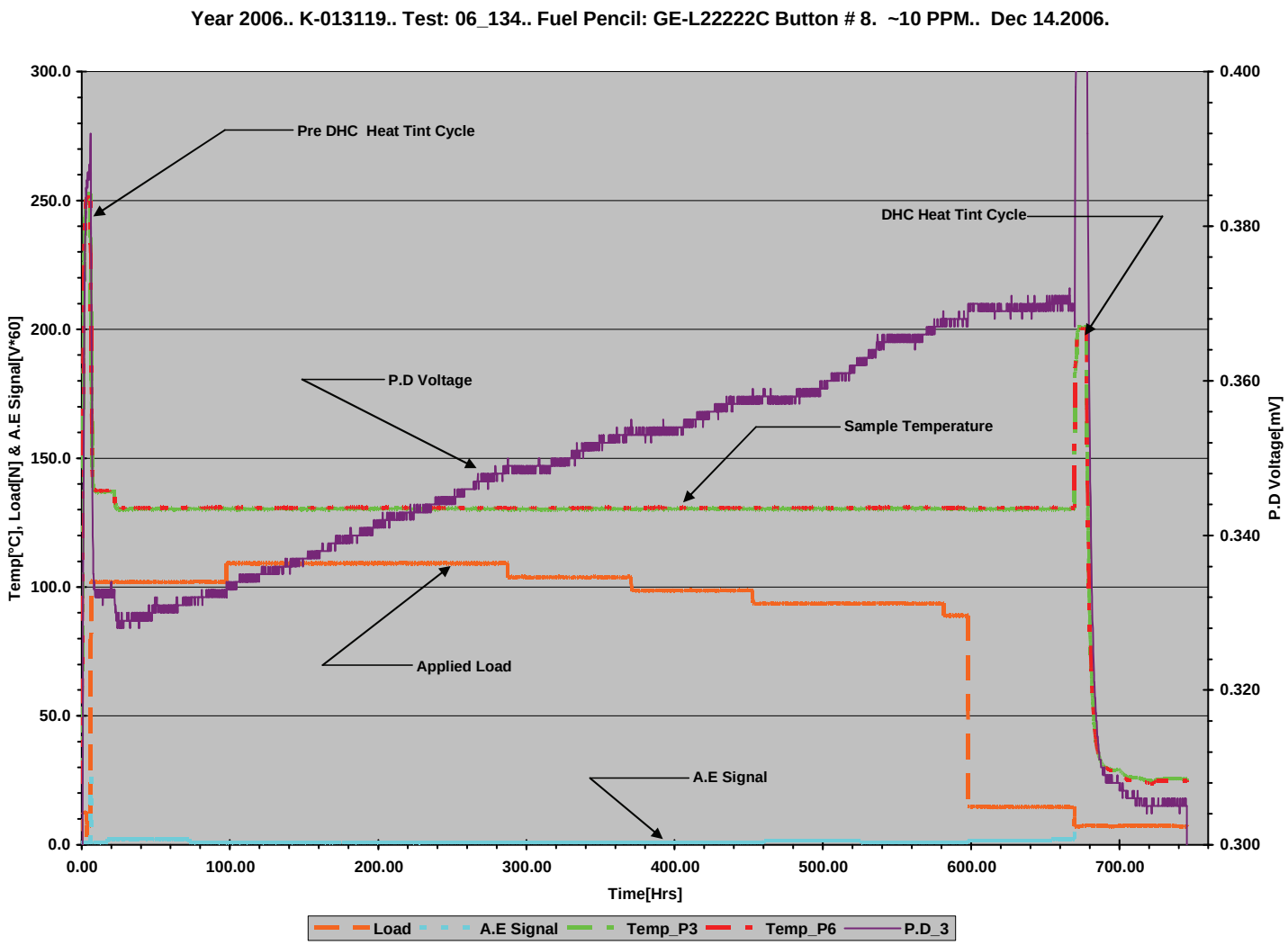

Figure 10: Test Record of Demonstration Test Showing the Temperature, Load, Potential Drop (PD), and, Acoustic Emission Signals (AE) (Test 06-134)

(a) Top view

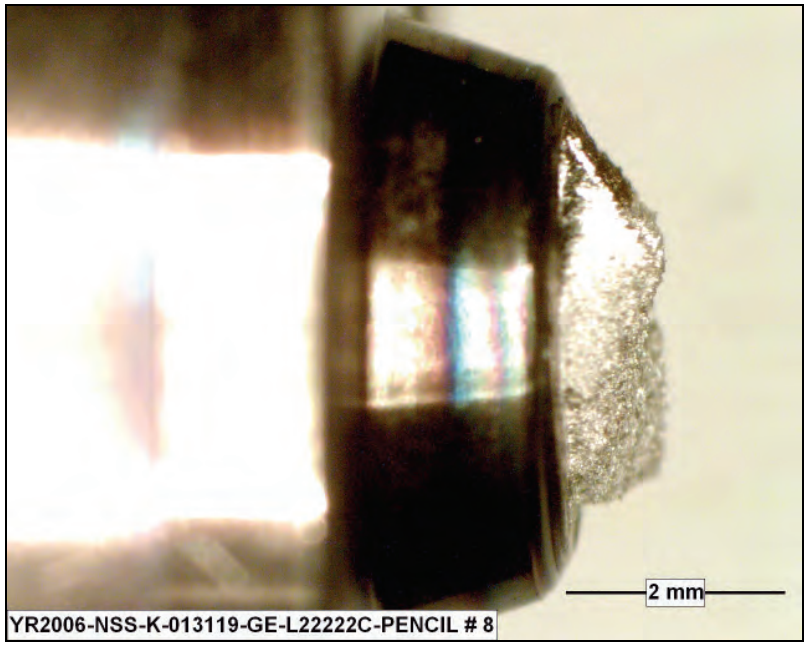

(b) Side view

Figure 11: Fracture Surface Appearance of Sample (Test 06-134)

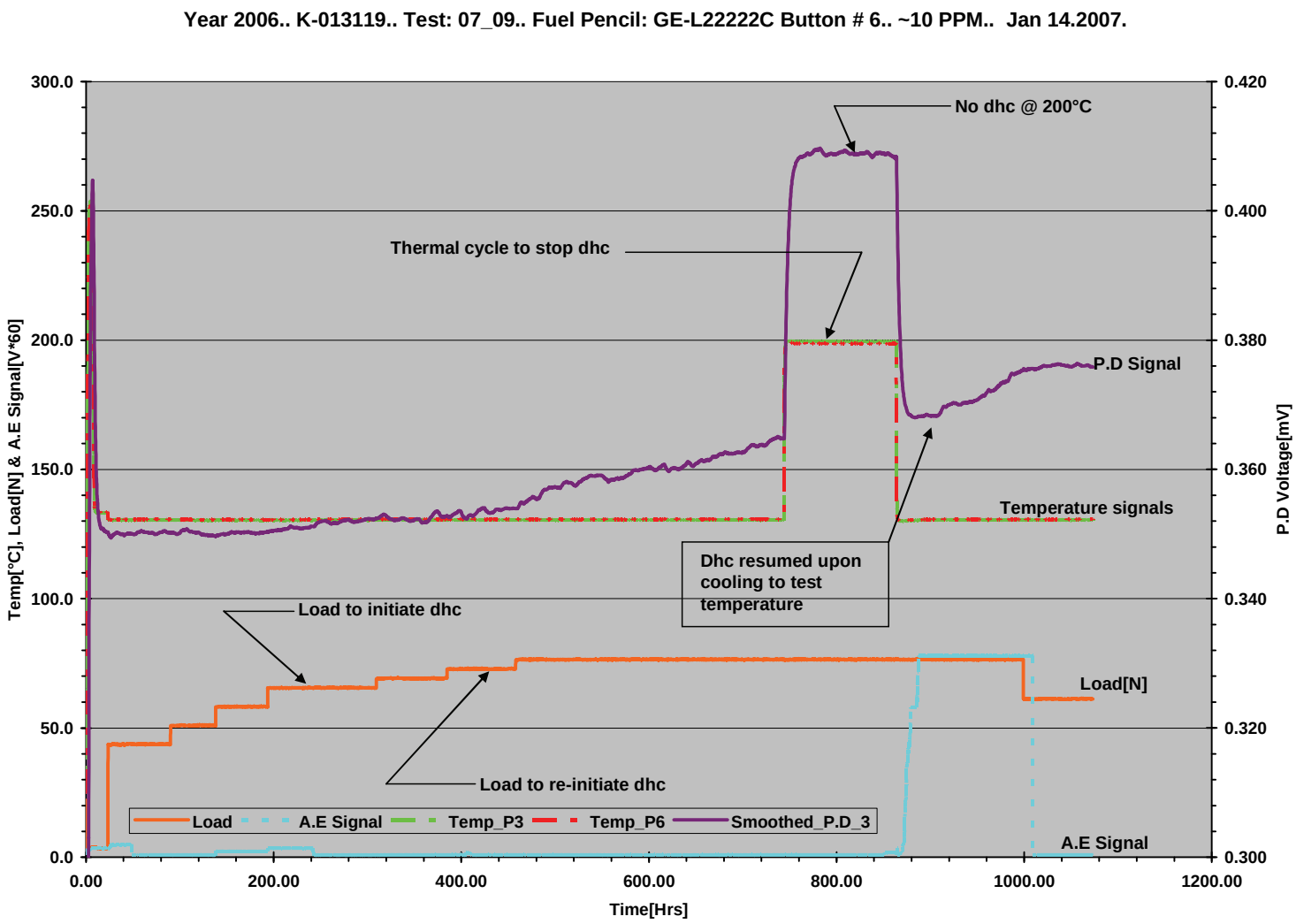

Figure 12: Test Record (Commissioning Test 07-09)

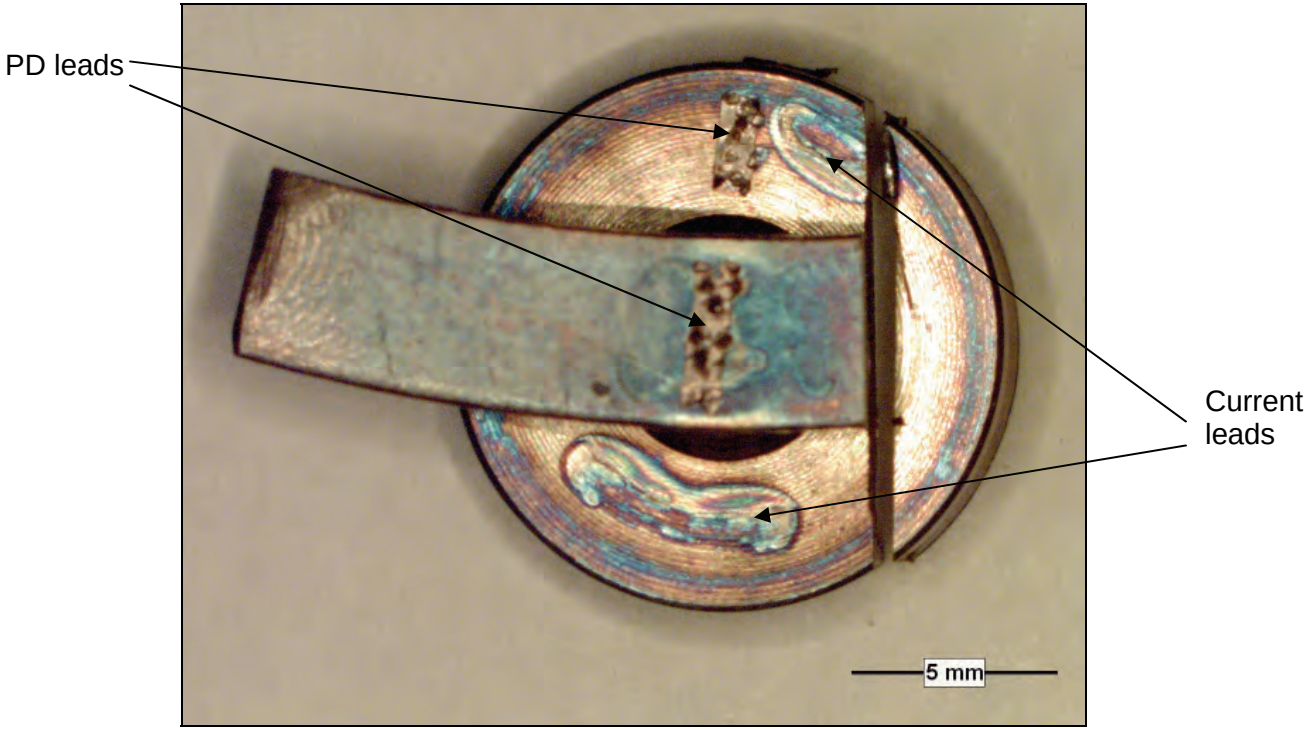

Figure 13: Photograph of Sample Showing the Cut Location for Metallographic Sample Locations of Current and PD Leads are also Shown (Test 07-09)

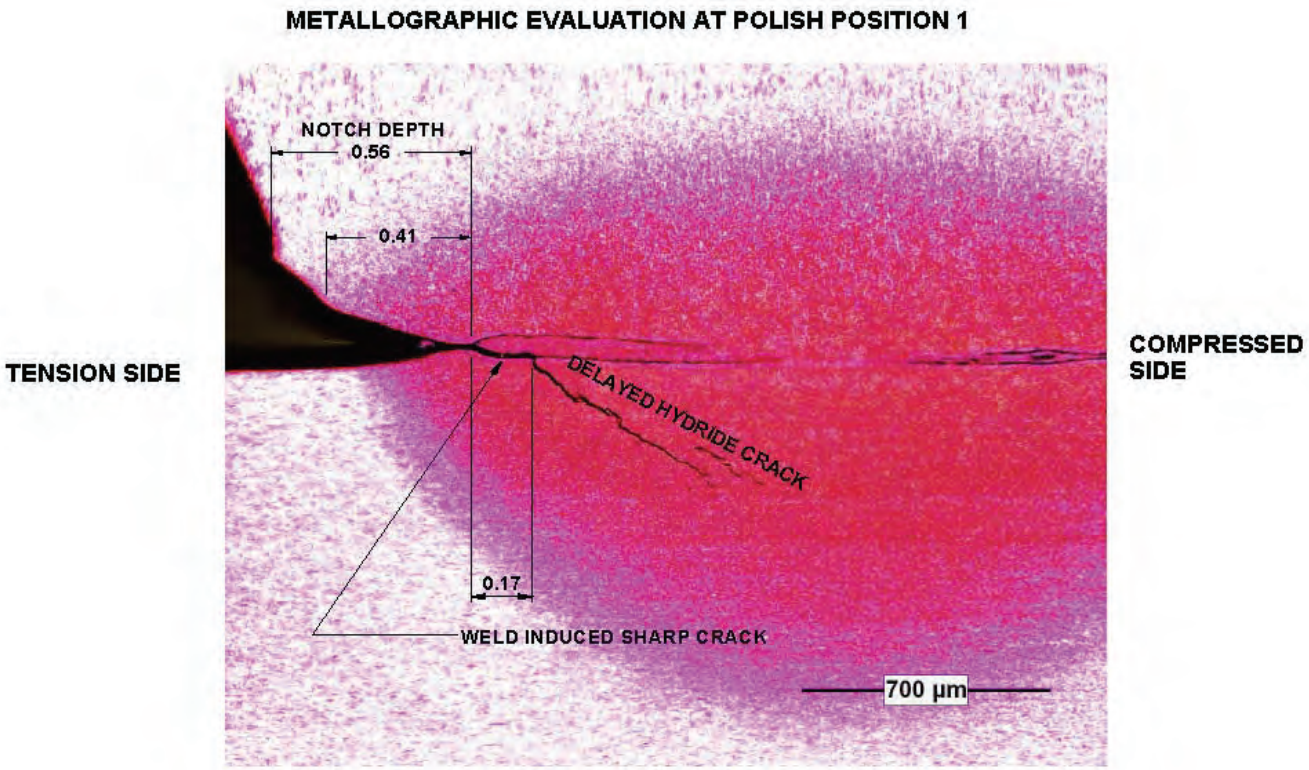

Figure 14: Metallographic Section of Sample Showing the Weld Notch. Weld Discontinuity and DHC Crack (Test 07-09)

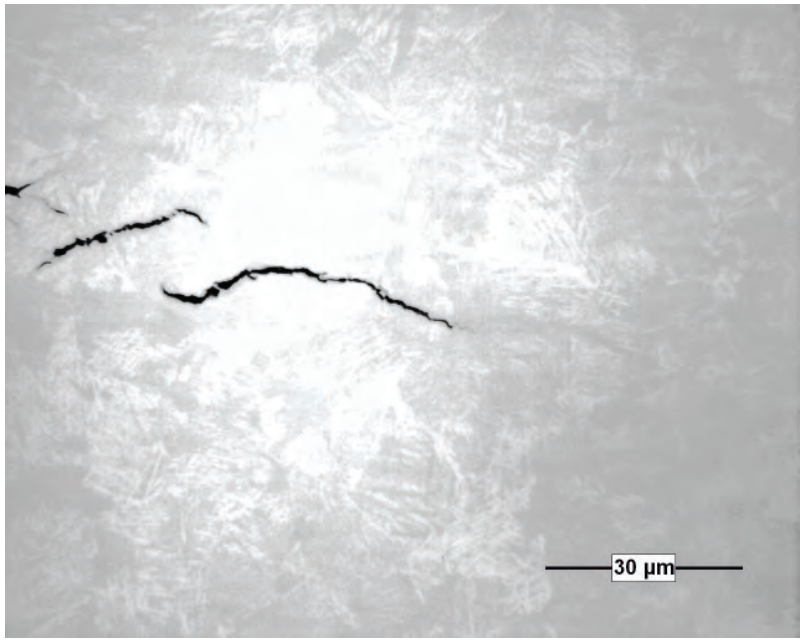

(a) as-polished

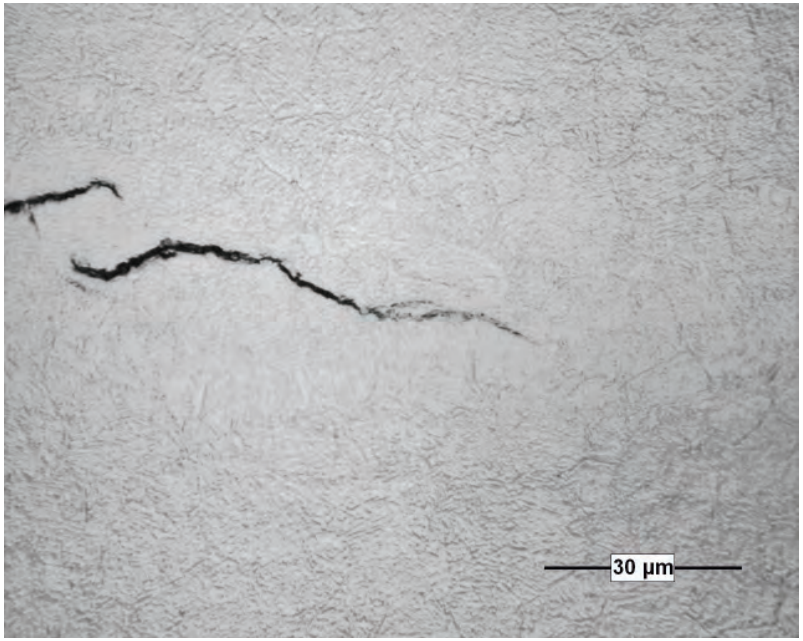

(b) chemically etched

Figure 15: The Tip of the DHC Crack in the “as Polished” and “Etched” Condition Showing the Uncracked Hydride

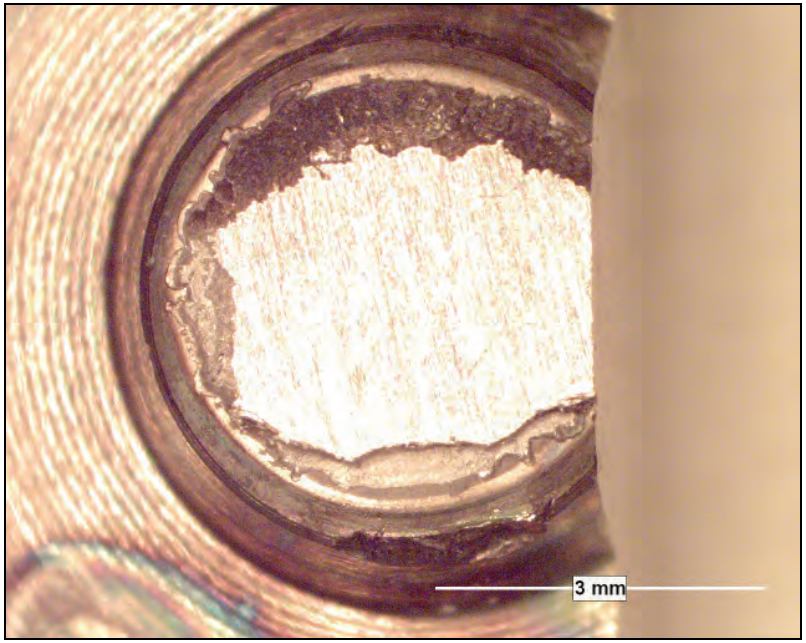

(a) DHC fracture surface on endcap

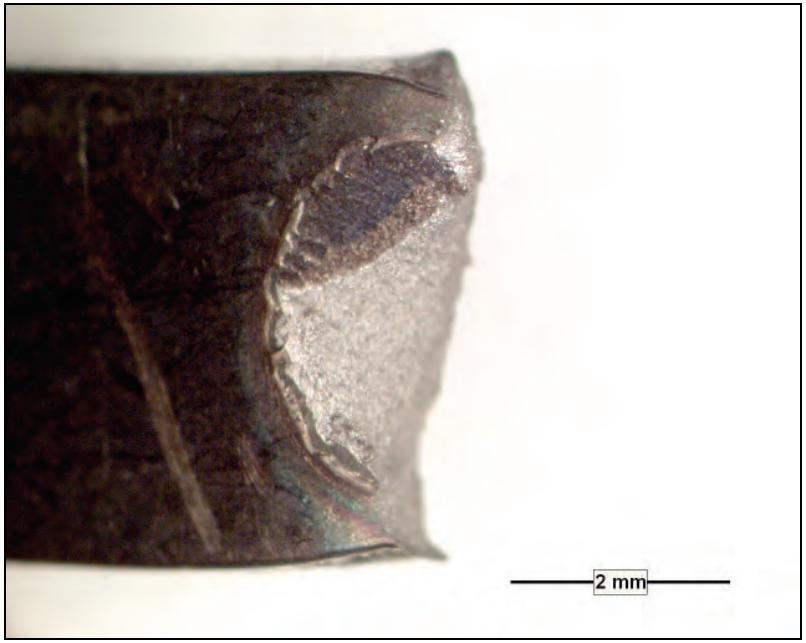

(b) DHC fracture surface on endplate

Figure 16: Fracture Surface of DHC Crack of Sample (Test 07-09)

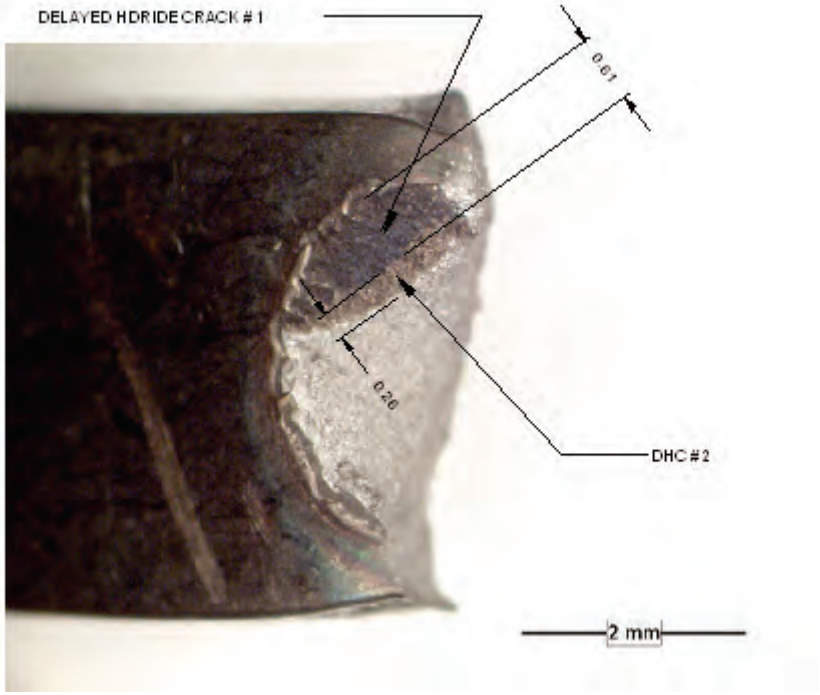

Figure 17: The Maximum Length of the Two DHC Crack Segments Measured from the Photograph (Test 07-09)

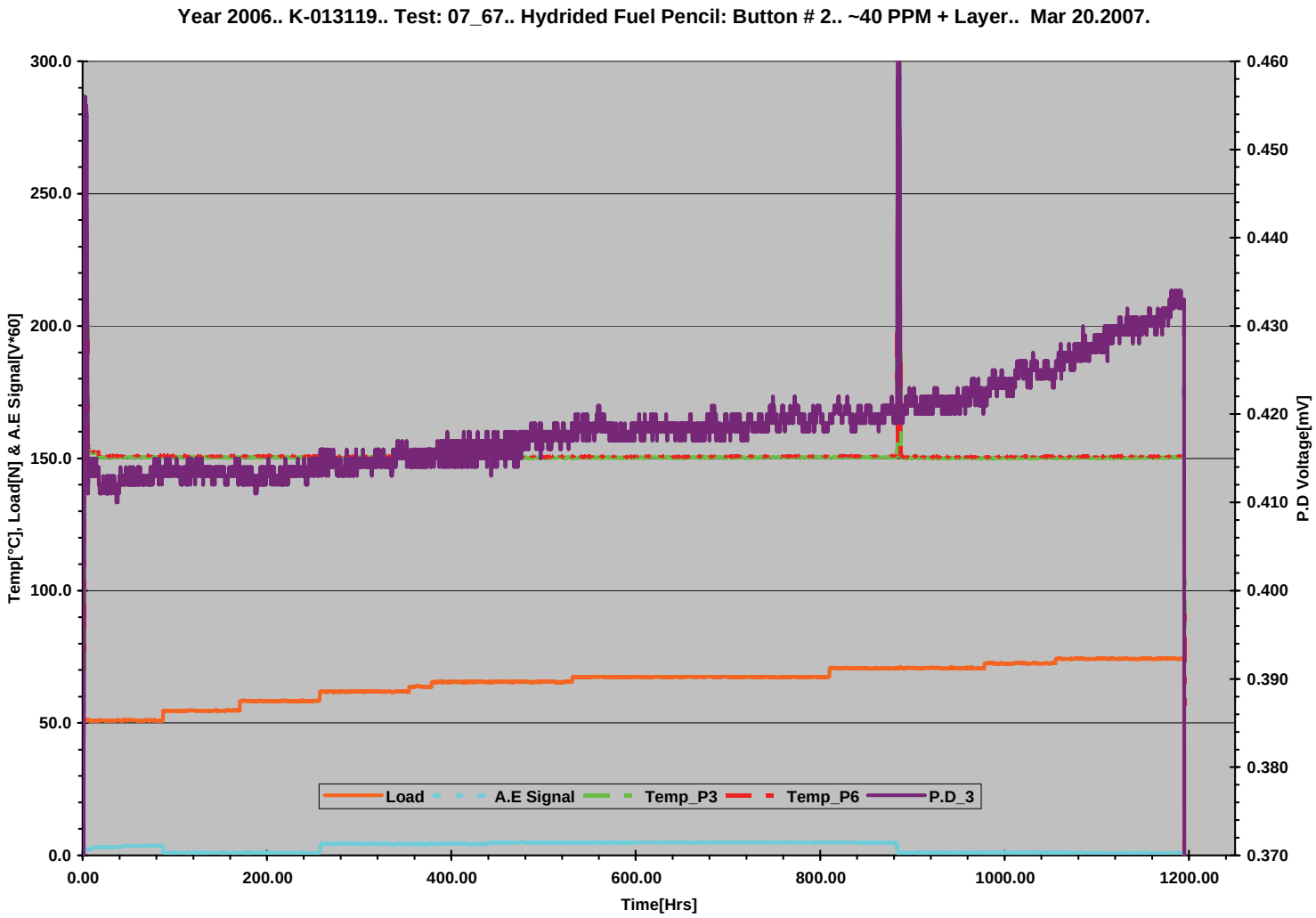

Figure 18: Test Record of DHC. The Heat-Tinting Cycle Performed at about 900 Hours (Commissioning Test 07-67)

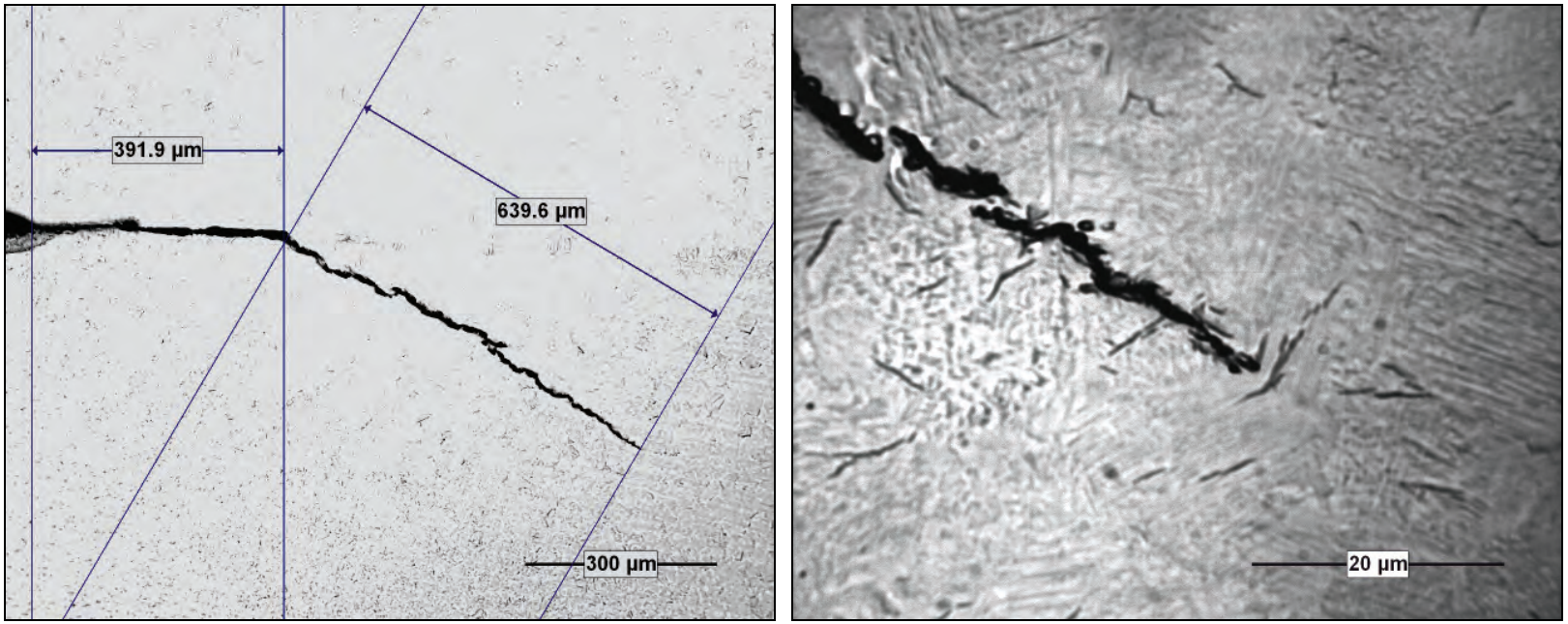

Figure 19: Metallographic Section Showing the Weld Discontinuity and Hydrides along the Crack (Test 07-67)

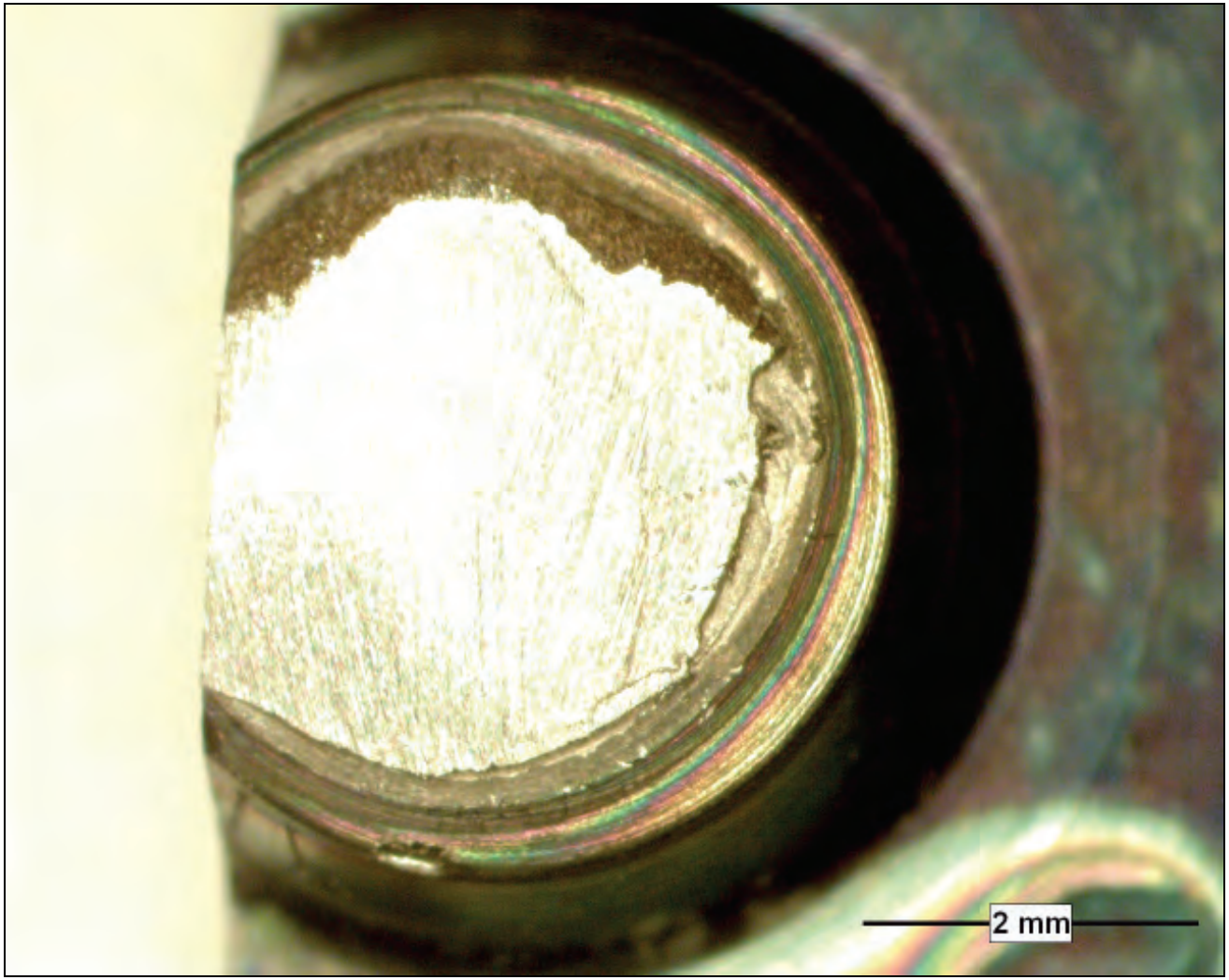

Figure 20: DHC Fracture Surface of Sample (Test 07-67)

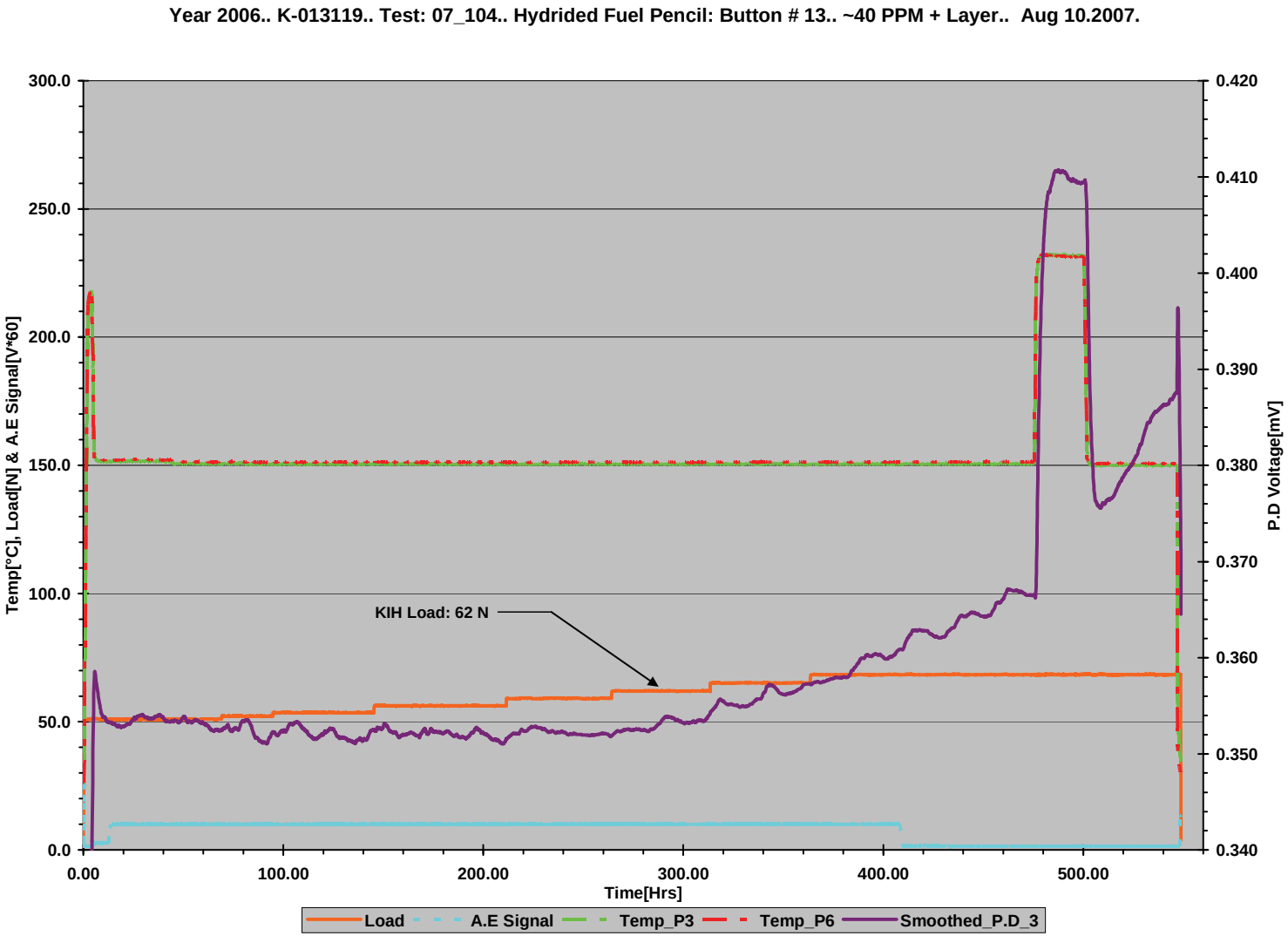

Figure 21: Test Record of K_{IH} Test (Test 07-104)

Top view

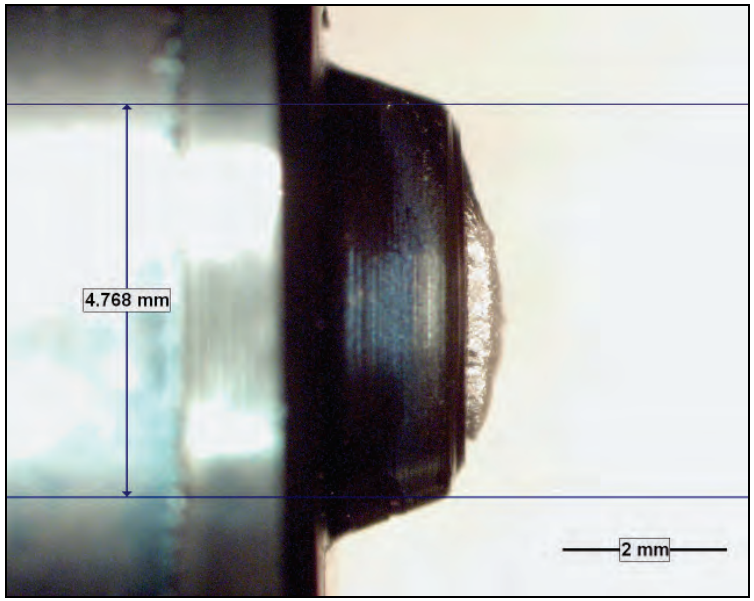

Side view

Figure 22: Fracture Surface Appearance of Sample (Test 07-104)

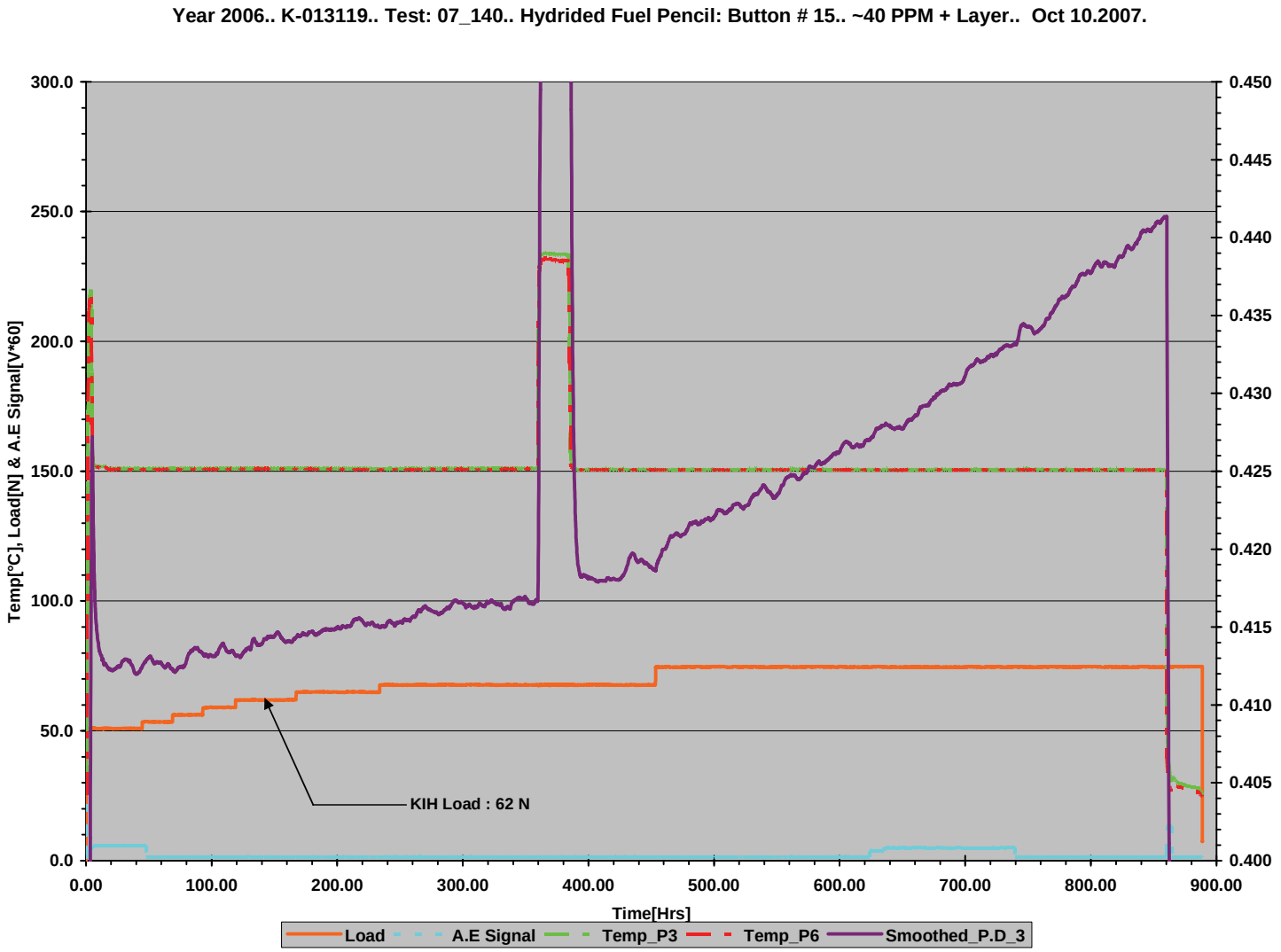

Figure 23: Test Record of K_{IH} Test (Test 07-140)

(a) Top view

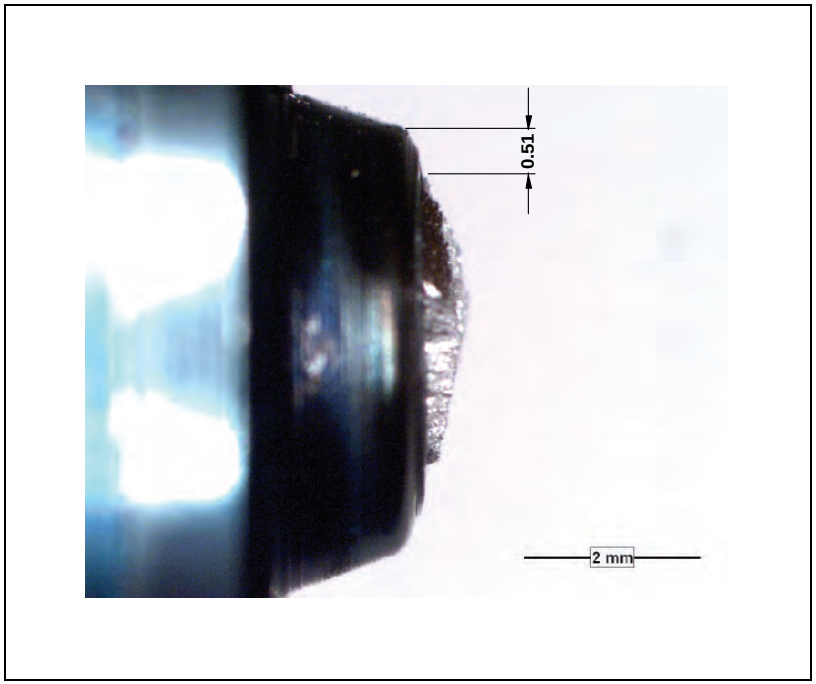

(b) Side view

Figure 24: Fracture Surface of Sample from K_{IH} Test (Test 07-140)

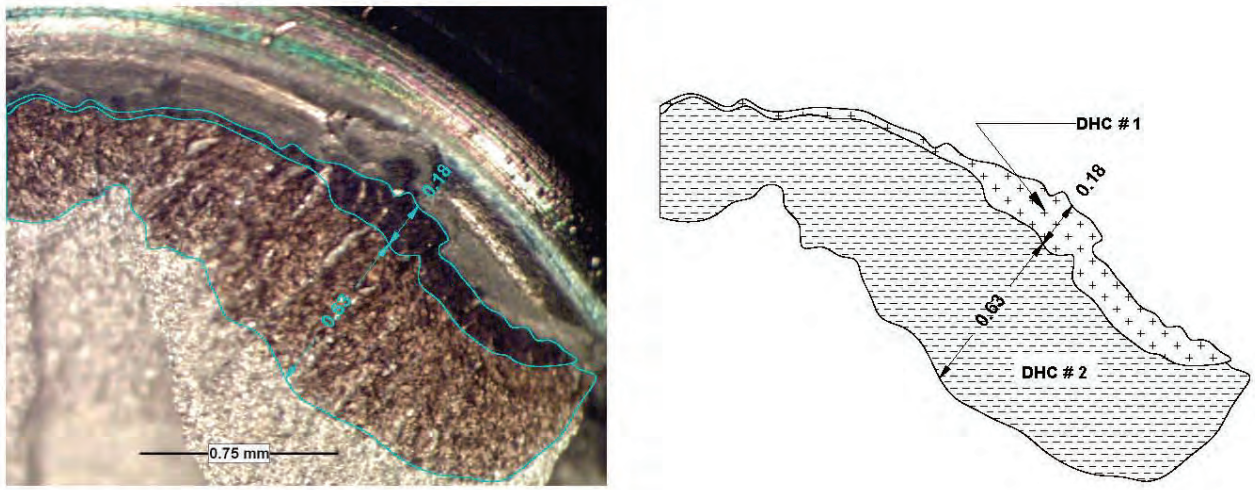

Figure 25: Higher Magnification of Fracture Surface of Sample Showing the Two DHC Segments (Test 07-140)

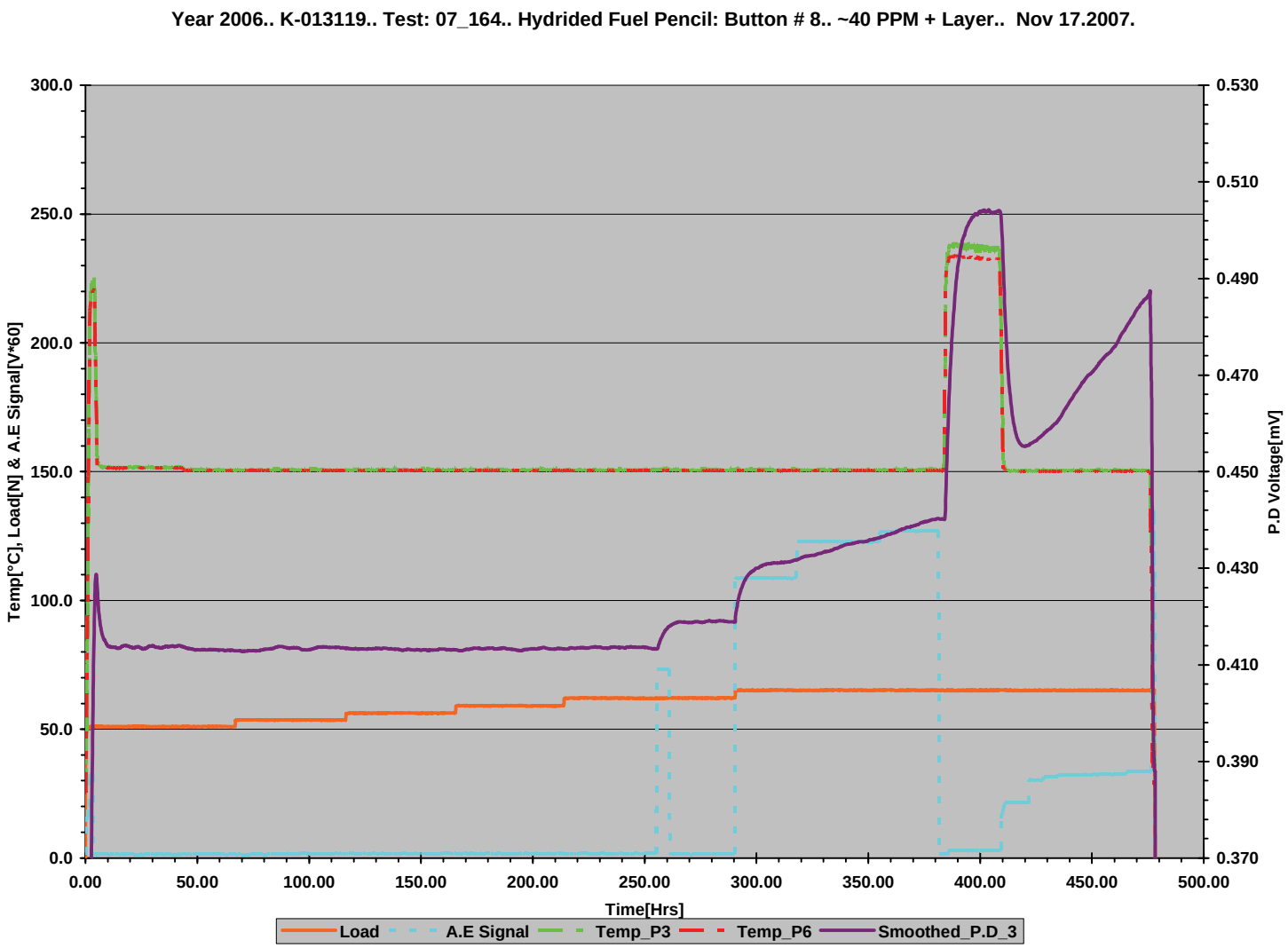

Figure 26: Test Record of K_{IH} Test (Test 07-164)

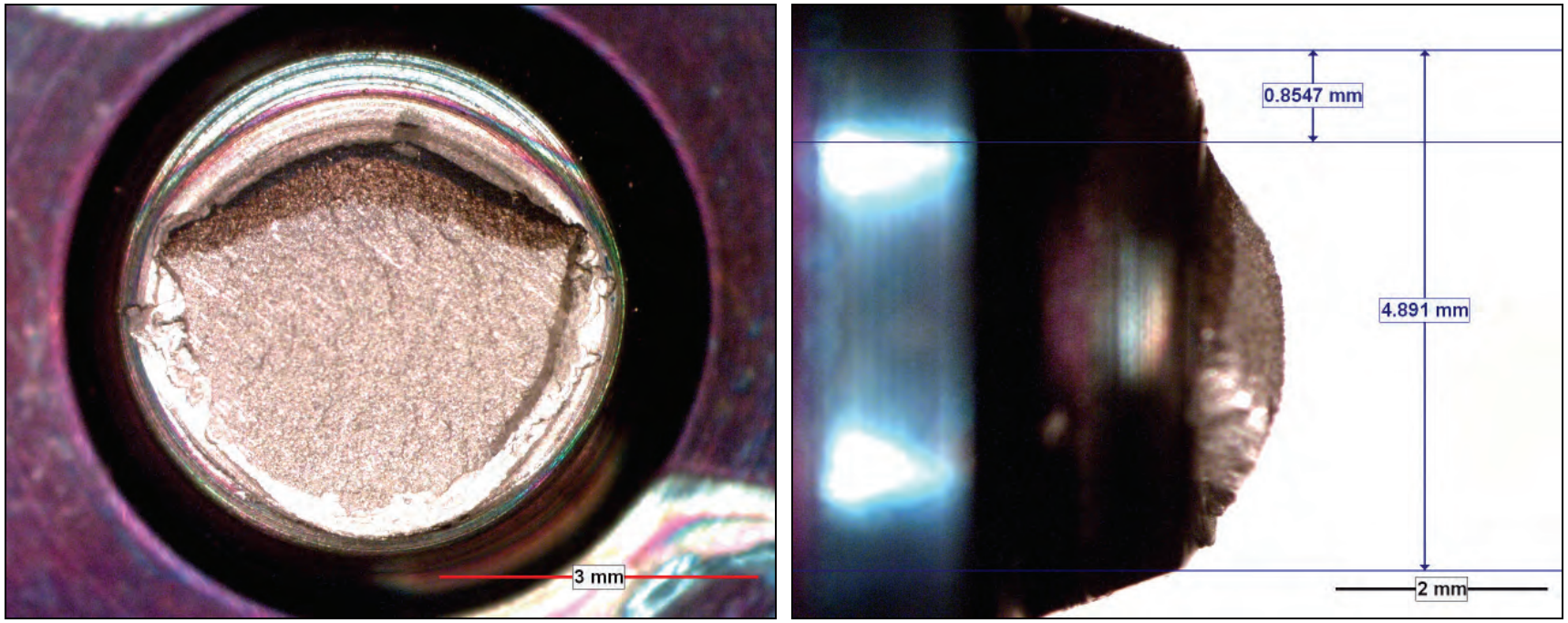

Top view

Side view

Figure 27: Fracture Surface of Sample (Test 07-164)

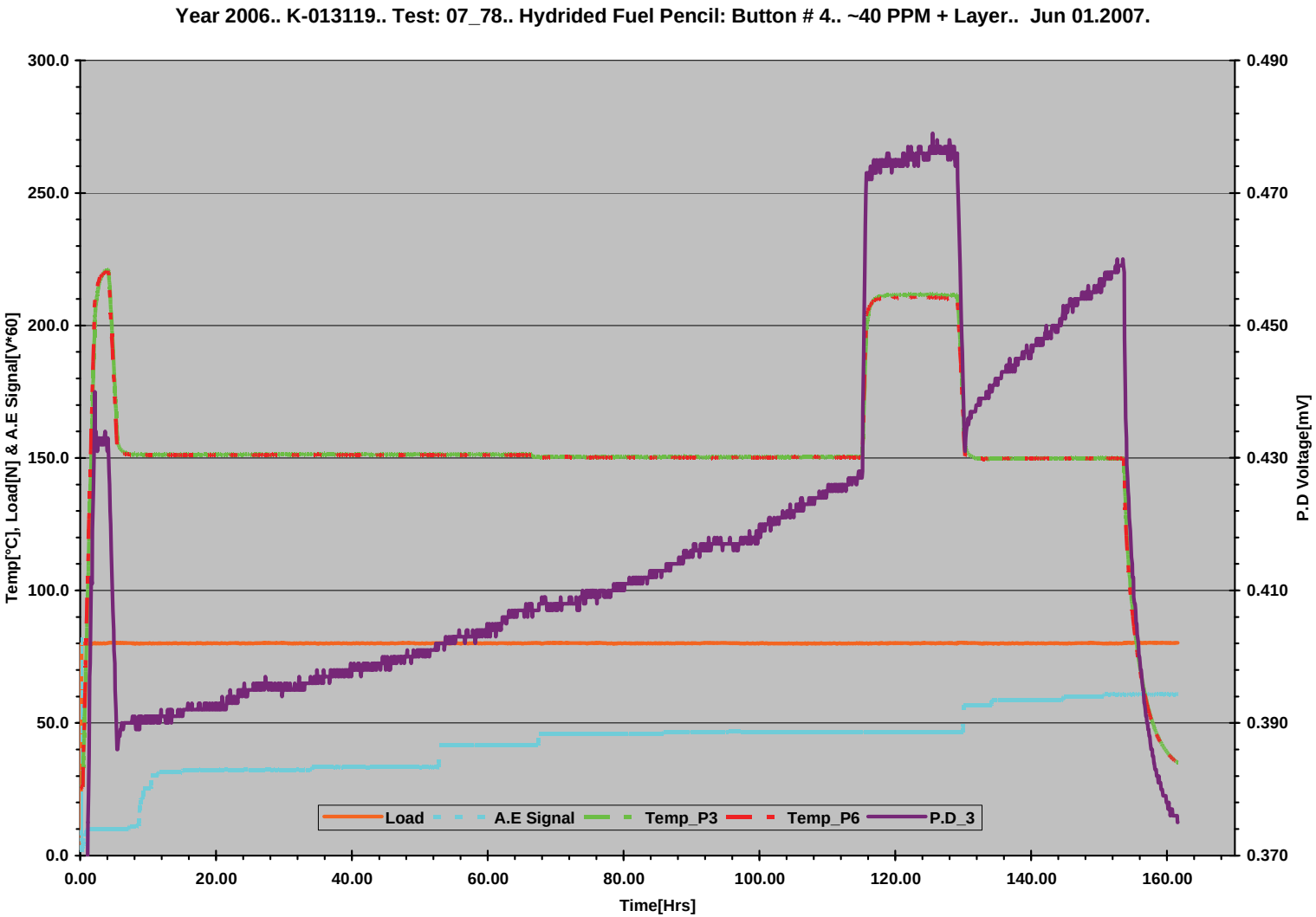

Figure 28: Test Record of DHCV Test (Commissioning Test 07-78)

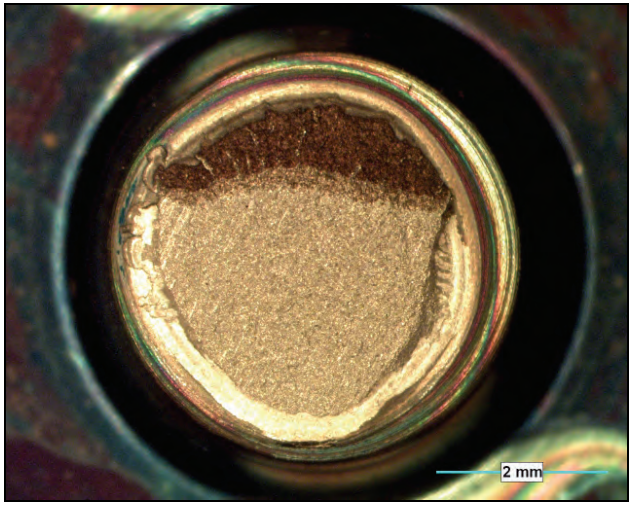

Top view

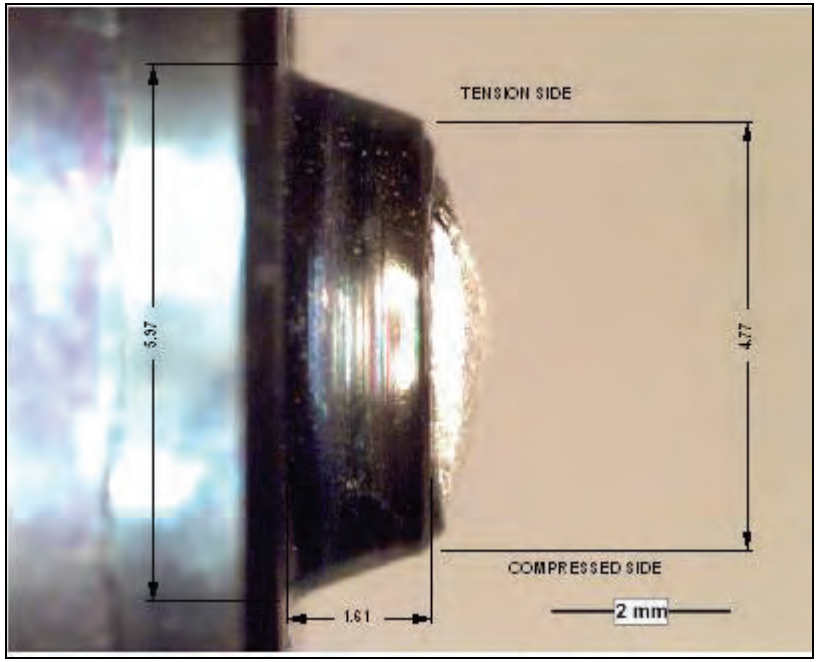

Side view

Figure 29: Fracture Surface Appearance of Sample (Test 07-78)

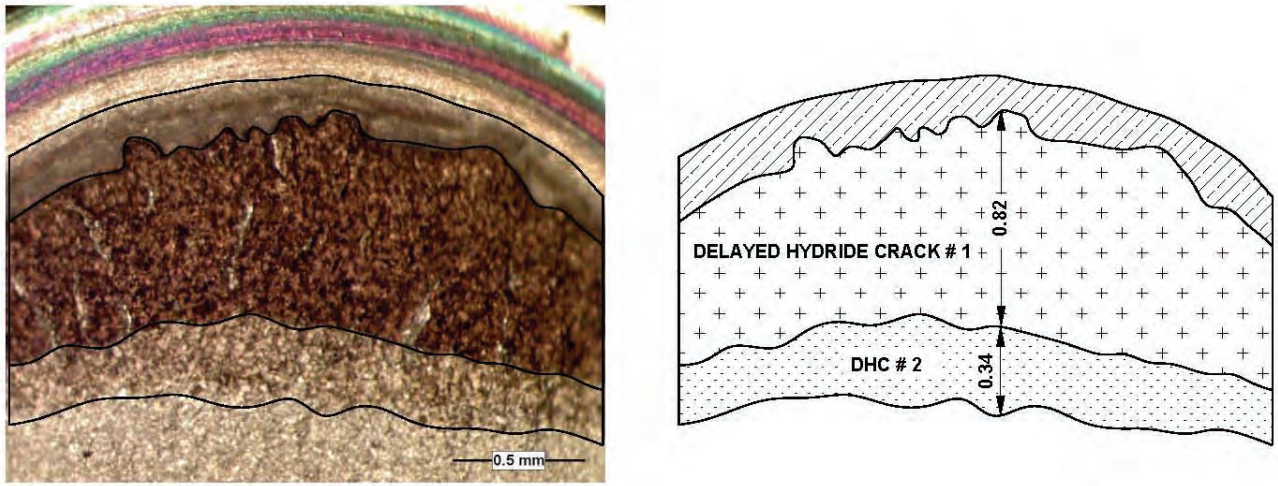

Figure 30: The Maximum Length of Each Crack Segment Was Measured from the Digitalized Picture (Test 07-78)

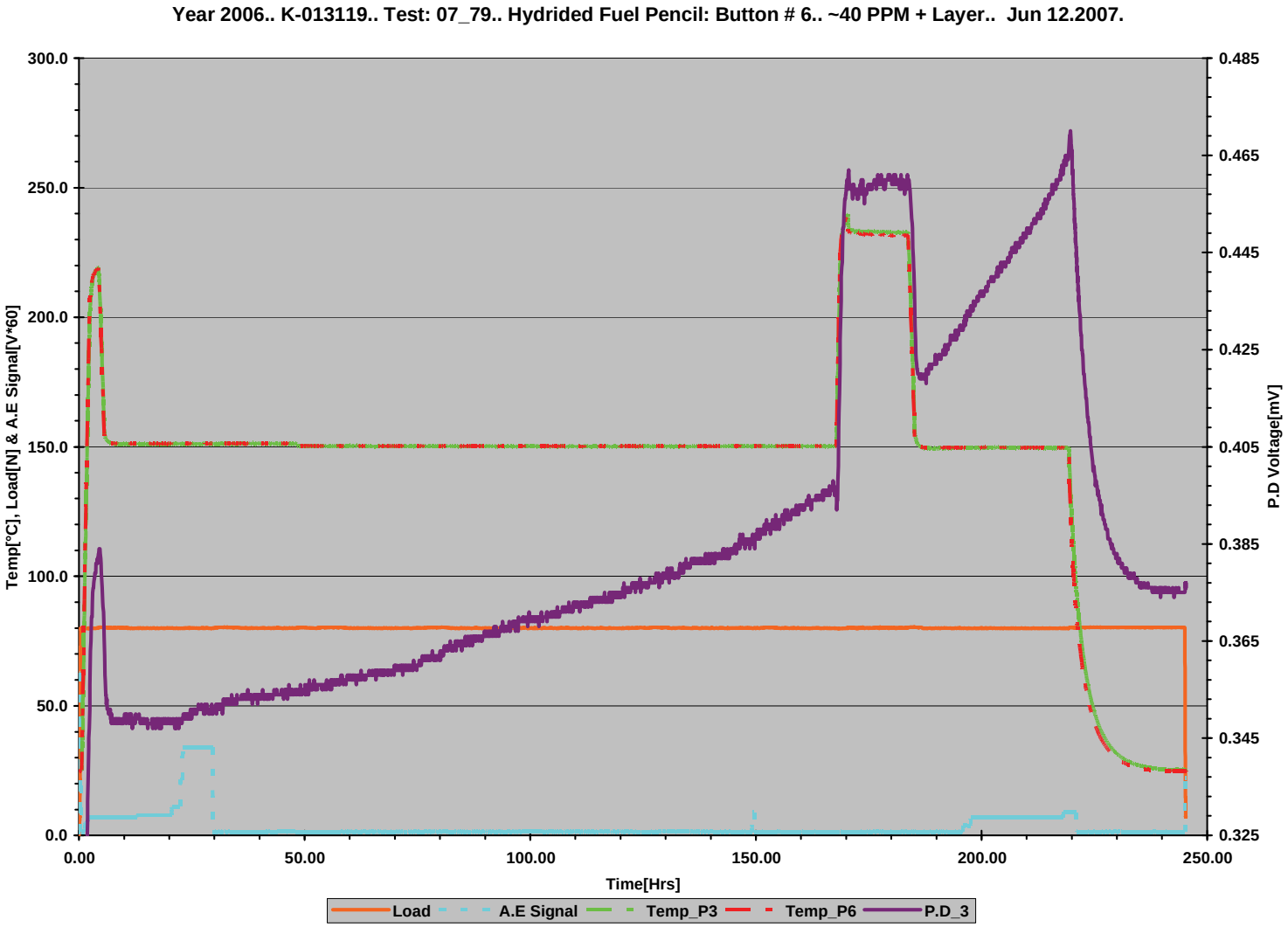

Figure 31: Test Record of DHCV Test (Commissioning Test 07-79)

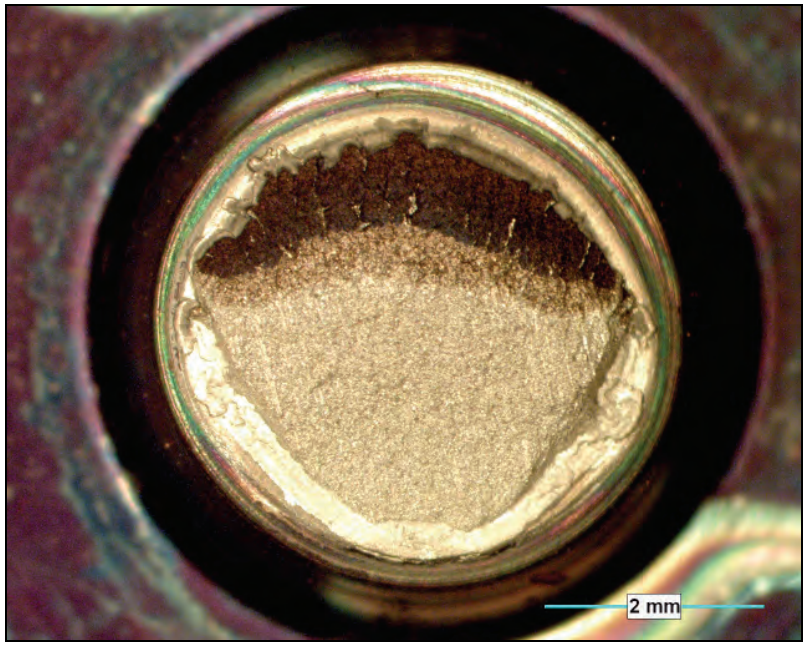

(a) Top view

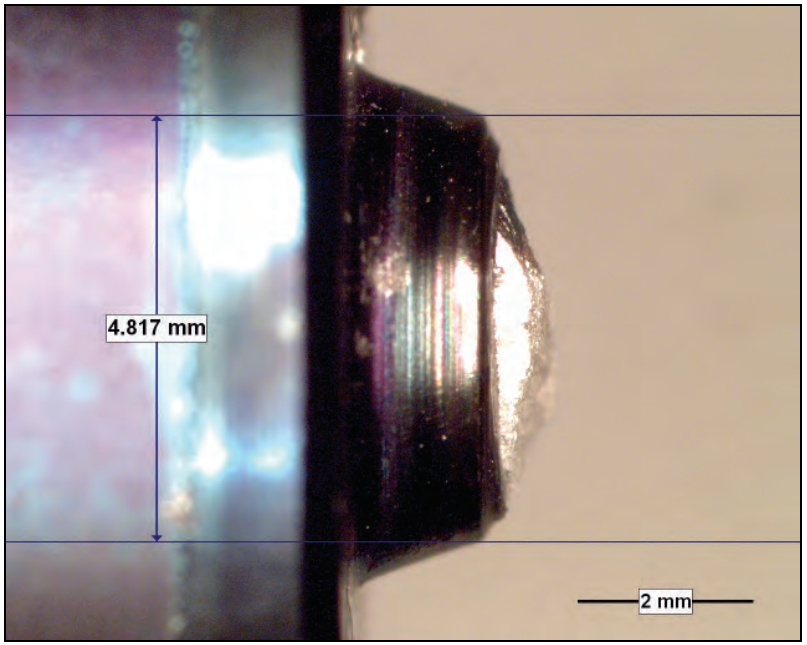

(b) Side view

Figure 32: Fracture Surface Appearance of Sample (Test 07-79)

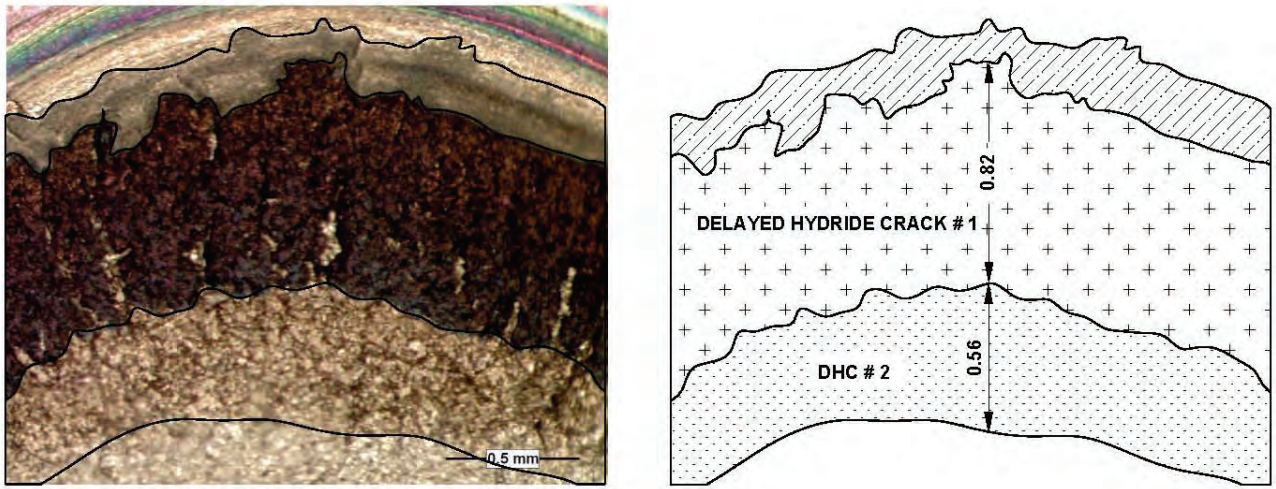

Figure 33: The Maximum Length of Each Crack Segment Measured from the Digitalized Picture (Test 07-79)

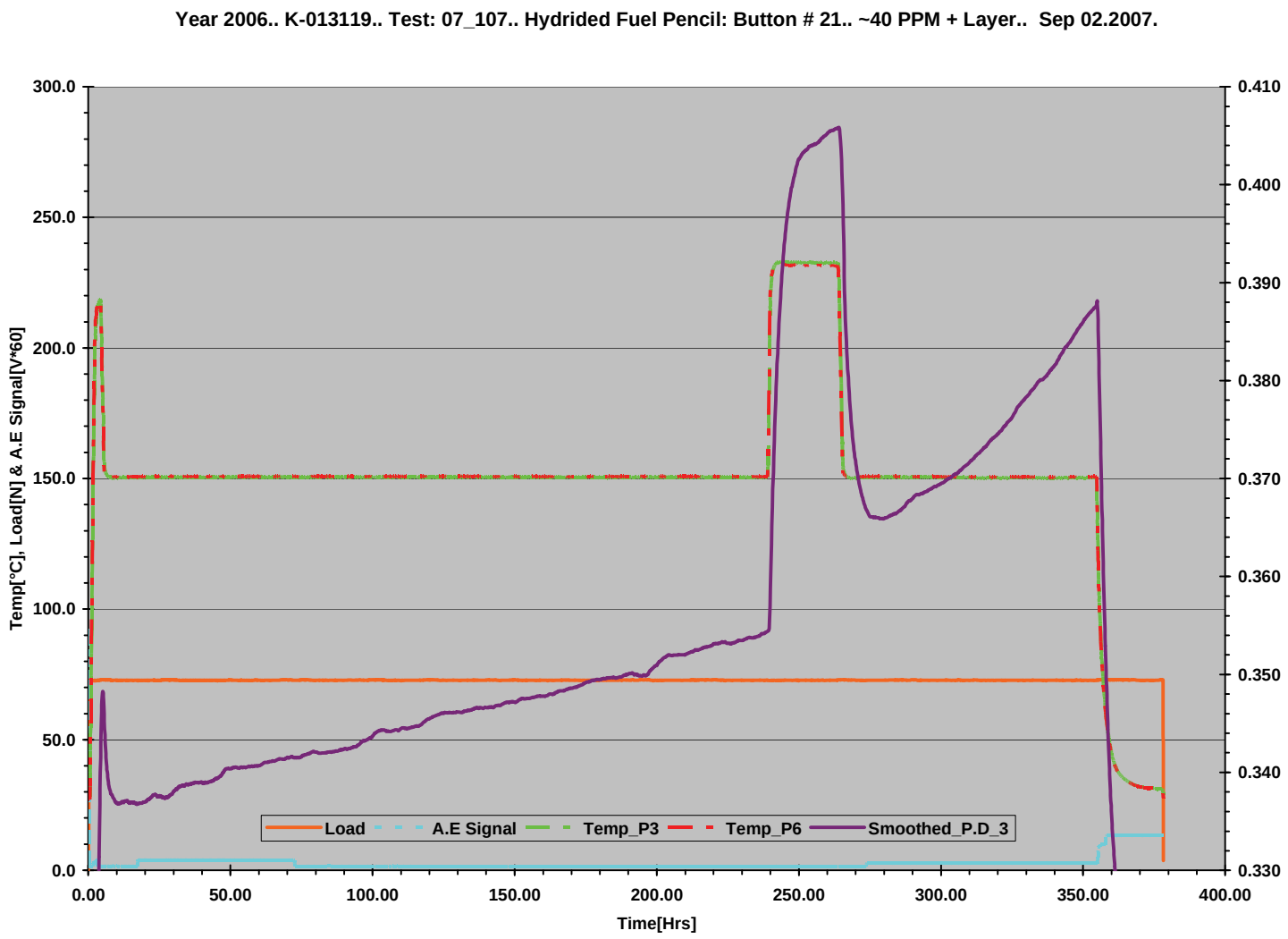

Figure 34: Test Record of DHCV Test (Test 07-107)

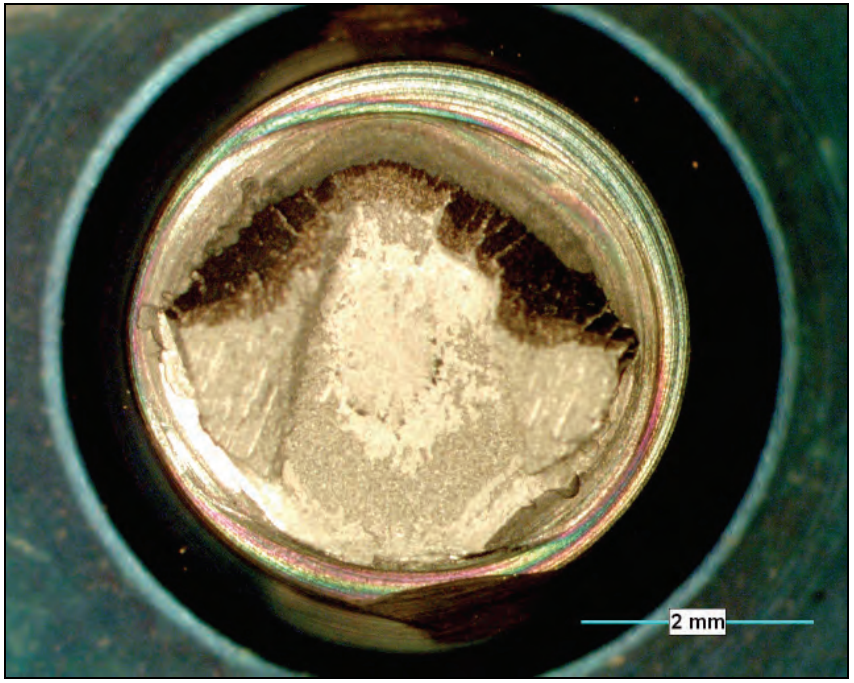

Fracture surface on endcap side

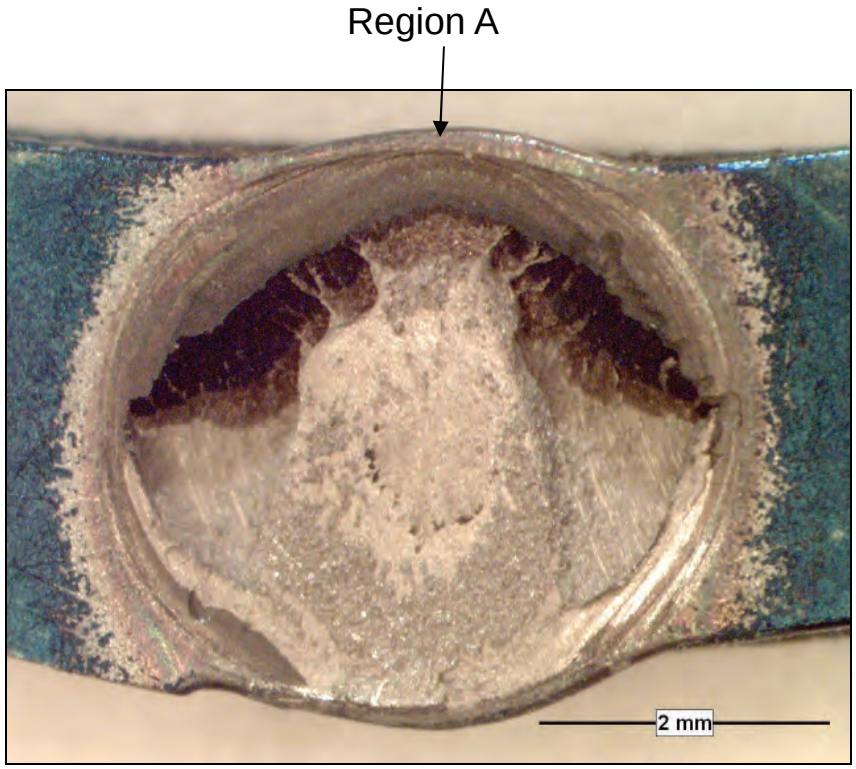

Fracture surface on endplate side

Figure 35: Top View of Fracture Surface of Sample of DHCV Test (Test 07-107)

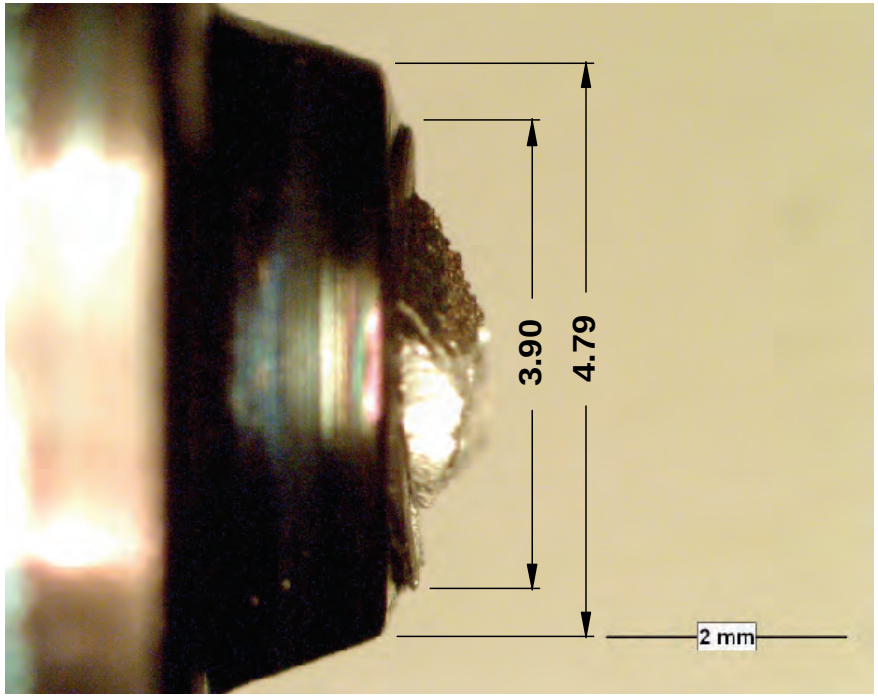

Figure 36: Side View of Fracture Surface (Test 07-107)

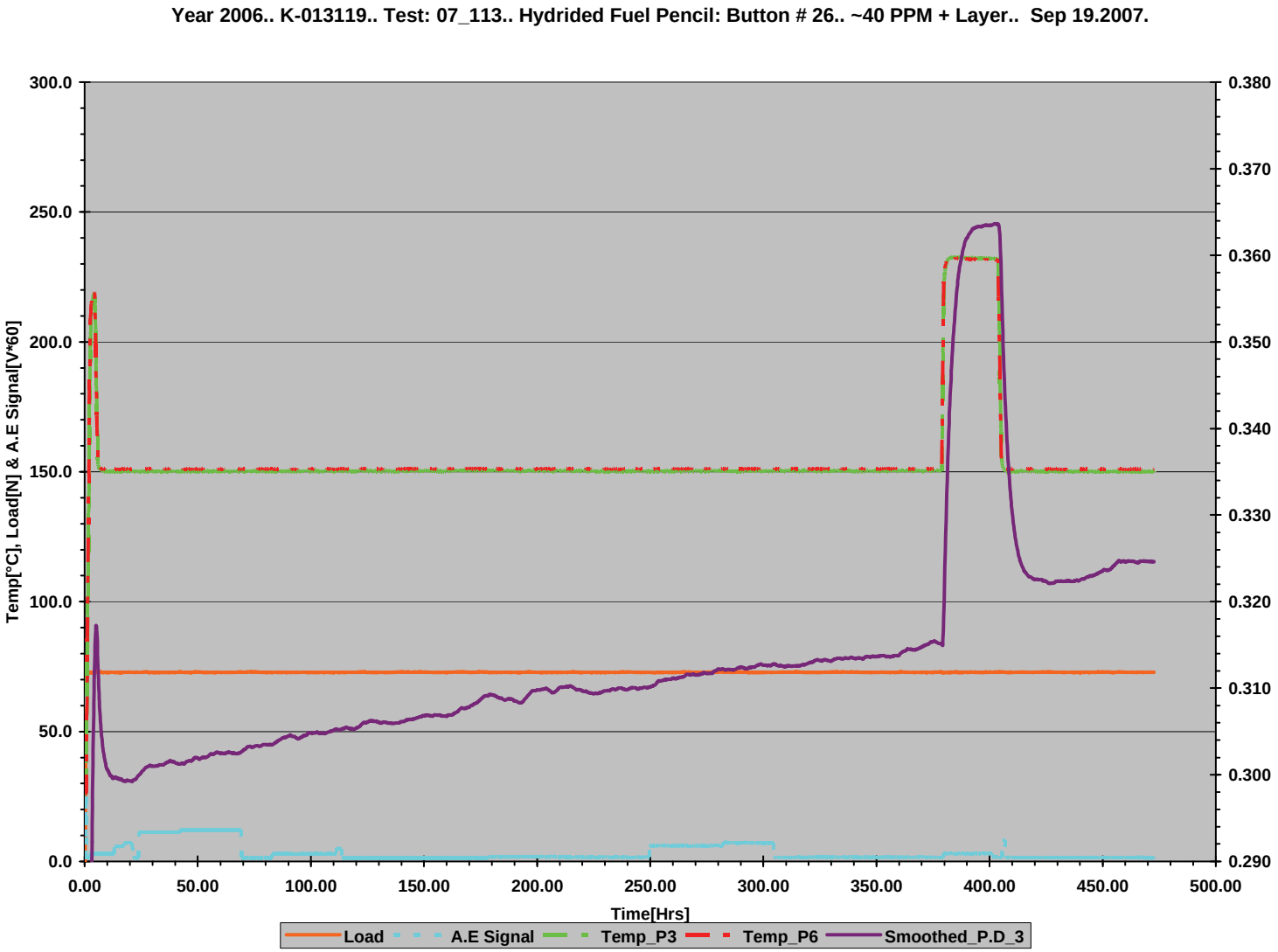

Figure 37: Test Record of DHCV Test (Test 07-113)

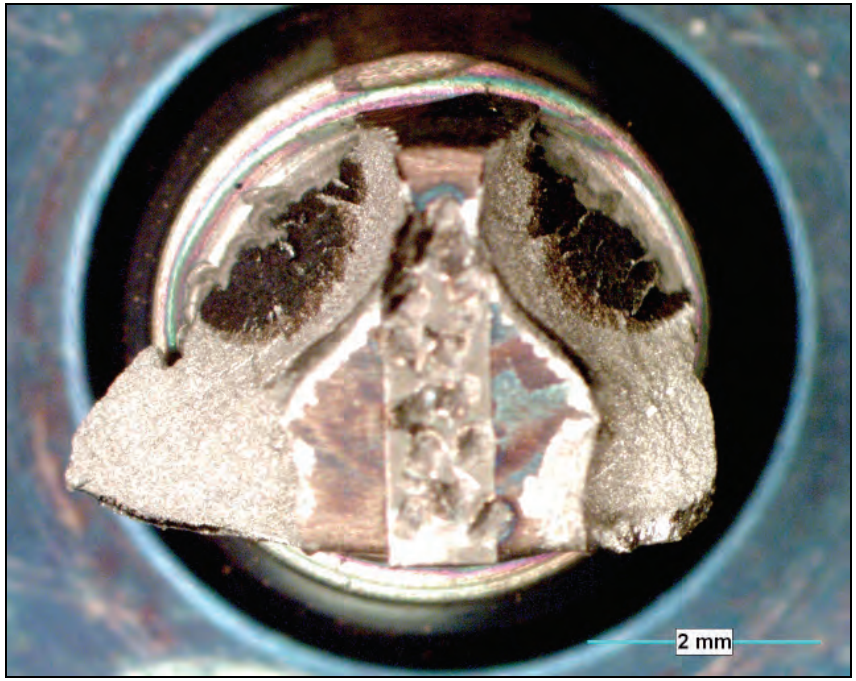

Top view

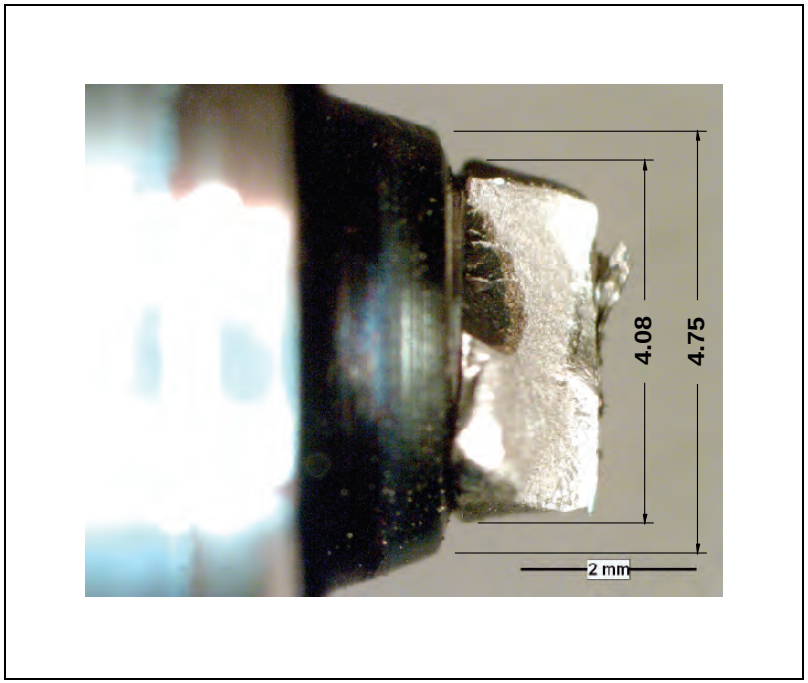

Side view

Figure 38: Fracture Surface of Sample from DHCV Test (Test 07-113)

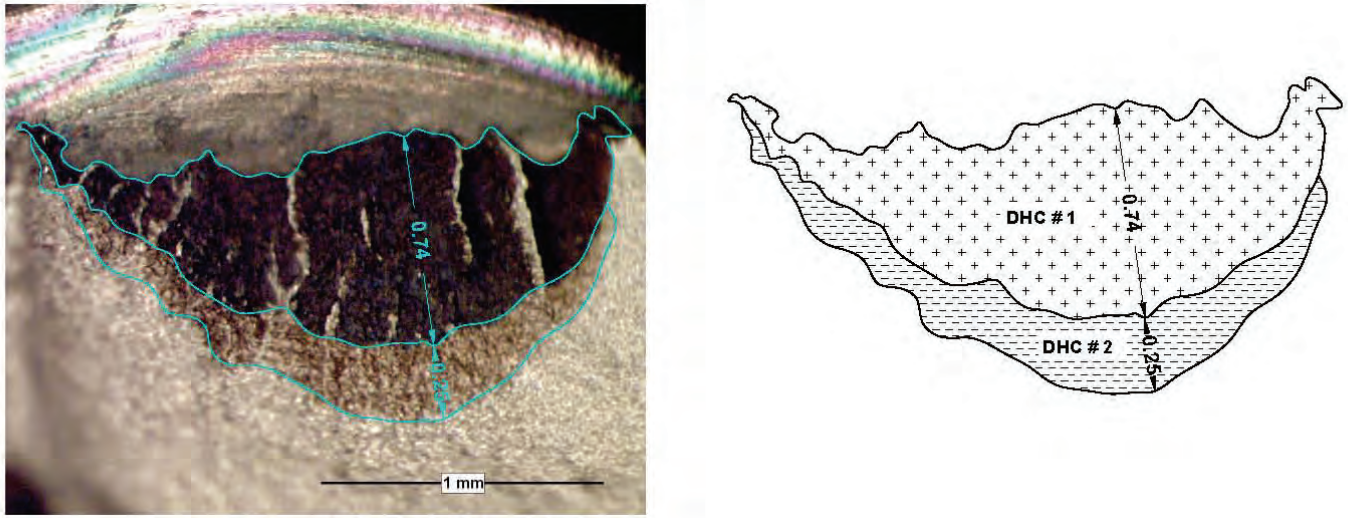

Figure 39: Fracture Surface of Sample Showing the Two DHC Segments (Test 07-113)

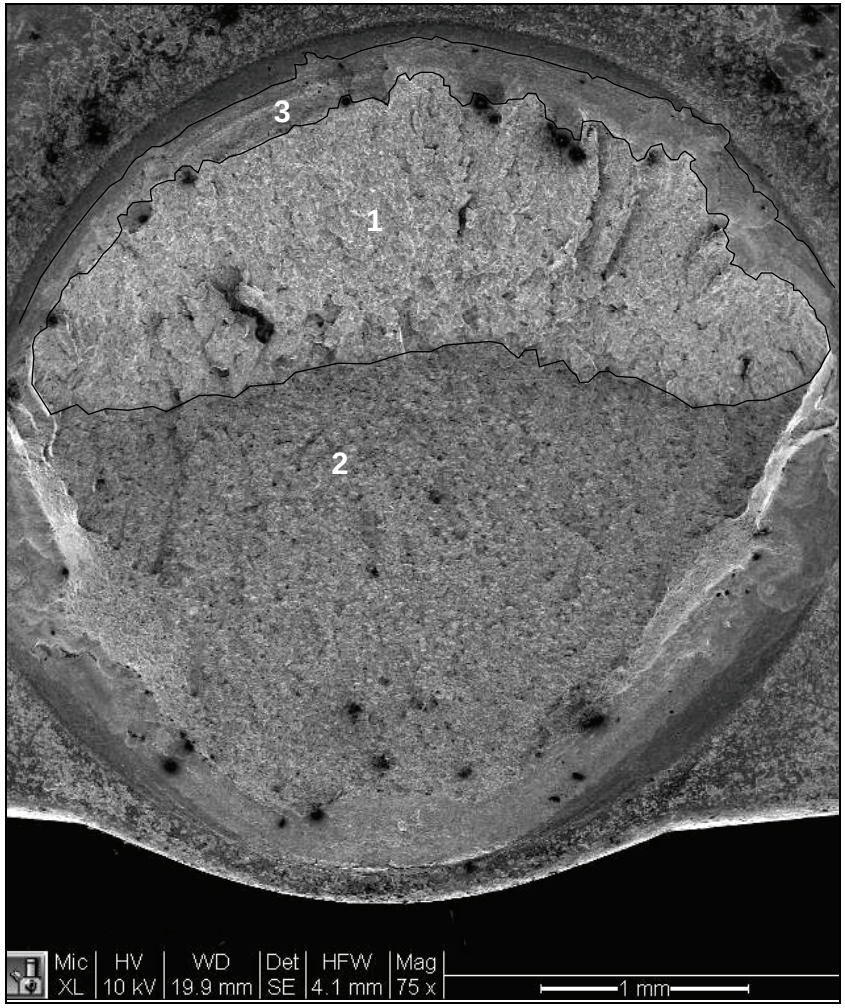

Figure 40: Low Magnification SEM Micrograph of Fracture Surface on the Endplate of Sample Showing the Three Regions of Interest. Region "1" : DHC; Region "2" : Room Temperature Tearing; And Region "3": Weld Discontinuity (Test 07-79)

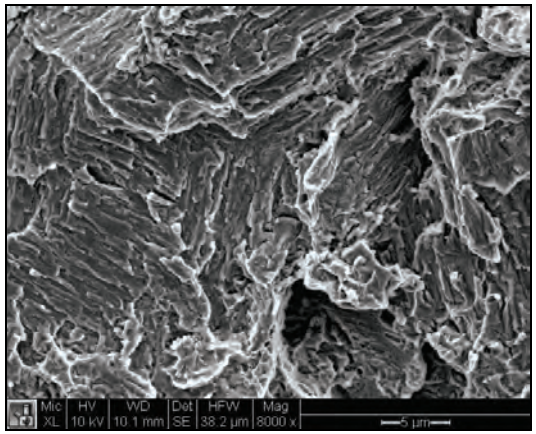

(a) Region “1”: cleavage brittle fracture

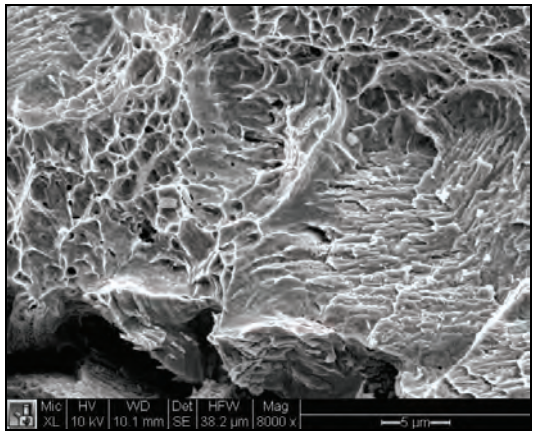

(b) Region “2”: ductile tearing features

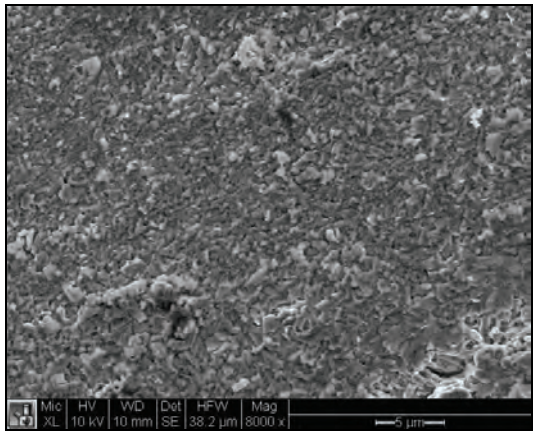

(c) Region “3”: weld discontinuity

Figure 41: Higher Magnification of the Three Regions (Test 07-79)

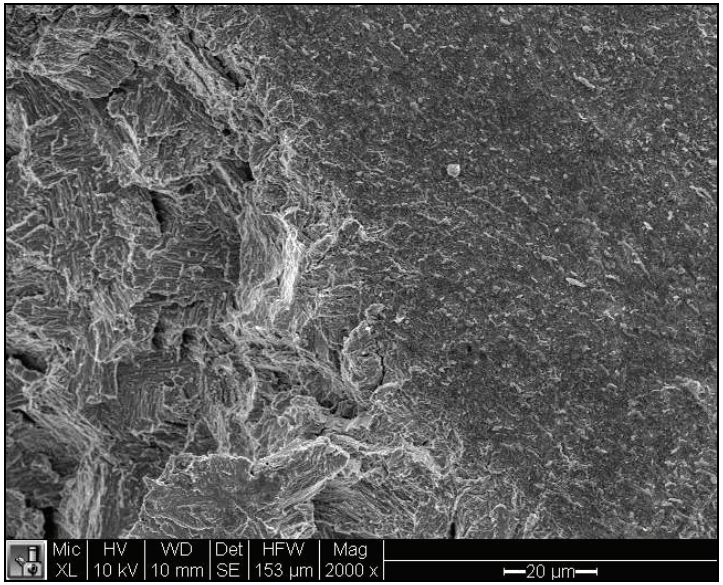

(a) Transition between weld discontinuity and DHC

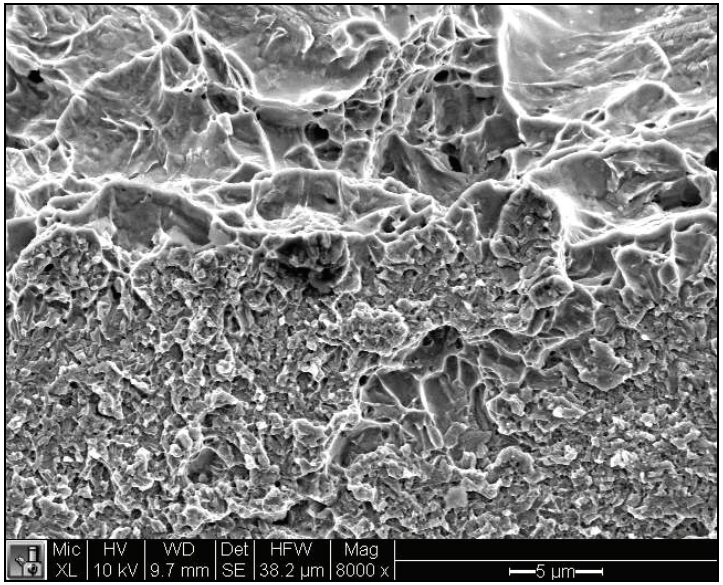

(b) between weld discontinuity and ductile tearing

Figure 42: Higher Magnification of the Transition Region (Test 07-79)

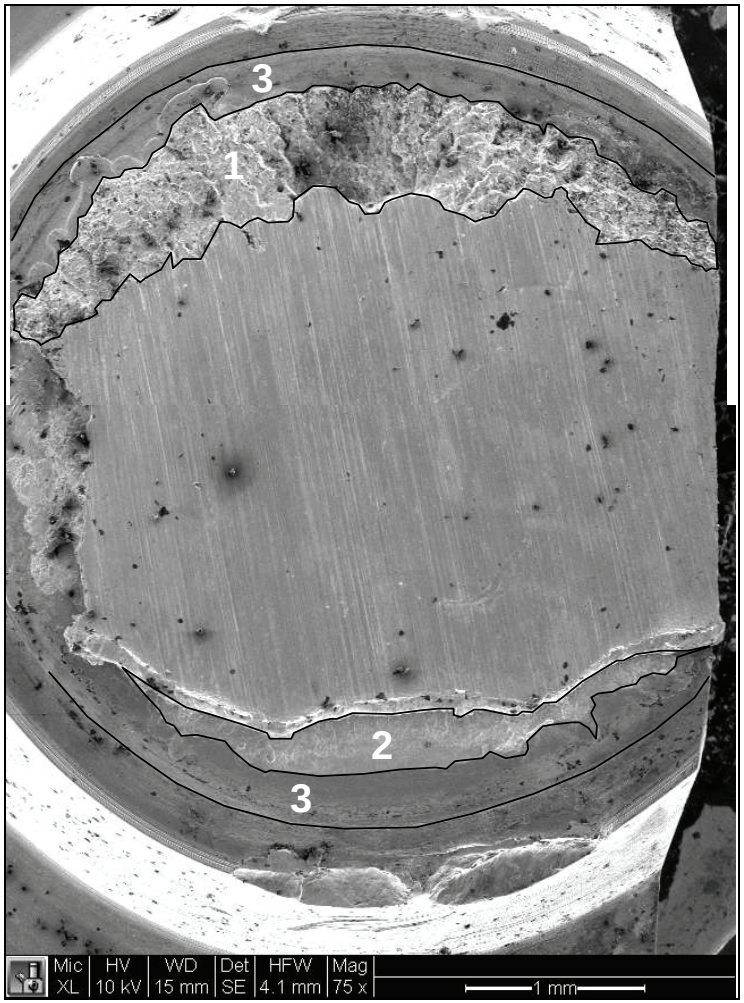

Figure 43: Low Magnification SEM Micrograph of the Fracture Surface of Sample (Test 07-09)

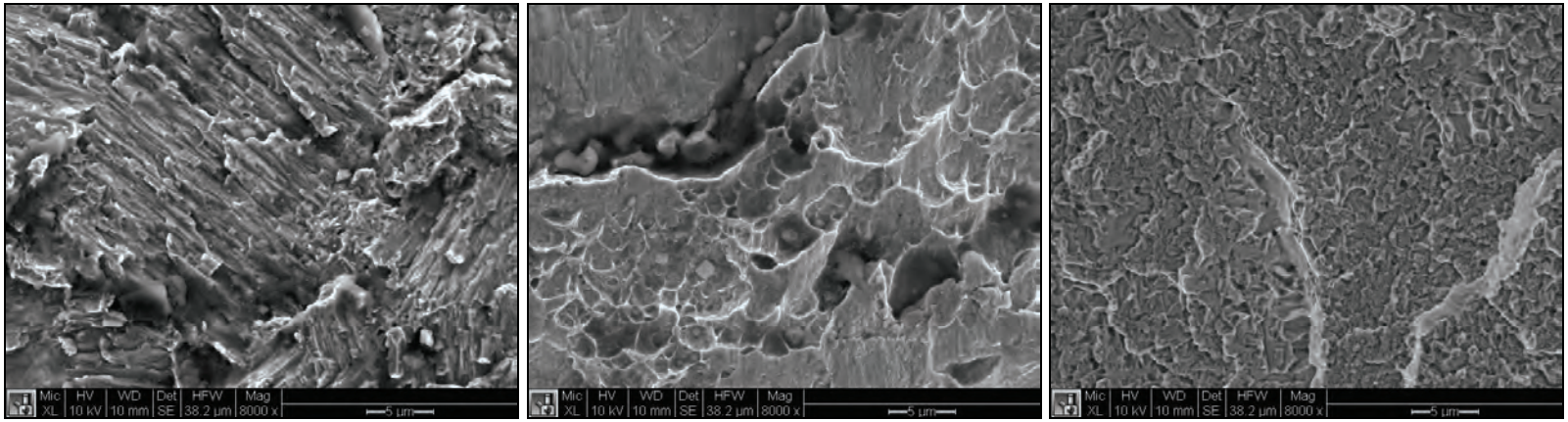

(a) Region “1”: cleavage brittle fracture (b) Region “2”: ductile tearing features (c) Region “3”: weld discontinuity

Figure 44: Higher Magnification SEM Micrographs of the Different Regions of Sample (Test 07-09)

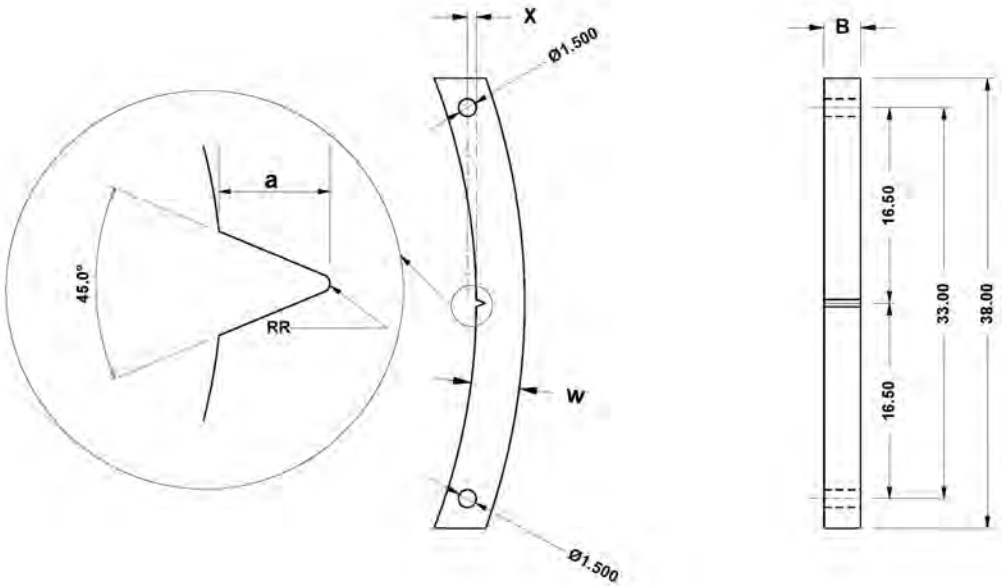

X = 0.75 mm
a = 0.75 mm
W = wall thickness = 4.1 mm nominal
B = 3.2 mm nominal
Notch root radius = 0.015 mm

Figure 45: C-Shape Sample Machined from Zr-2.5Nb Pressure Tube

APPENDIX A: NUMERICAL AND ANALYTICAL COMPUTATIONS OF STRESS INTENSITY FACTOR FOR DHC CRACK INITIATION

CONTENTS

Page

A1. INTRODUCTION 71
A2. GEOMETRY OF A FUEL BUNDLE ELEMENT 71
A3. APPLIED LOADING 72
A4. MATERIAL PROPERTIES 72
A5. RESULTS 73
A6. CONCLUSIONS 75
A7. RECOMMENDATIONS 75
A8. REFERENCES 75
A9. SECTION Aa-FUEL PENCIL FROM 07_09 TEST 77
A10. SECTION Ab - ANALYTICAL APPROACH TO COMPUTE THE STRESS INTENSITY FACTOR 81

A10.1 ERDOGAN AND TADA SOLUTION (METHOD I) 81
A10.2 COMPUTED STRESS INTENSITY FACTOR FOR 07_09 TEST 82
A10.3 BENTHEM SOLUTION (METHOD II) 82
A10.4 COMPUTED STRESS INTENSITY FACTOR FOR 07_09 TEST 83
A10.5 SUMMARY OF RESULTS FROM THE ANALYTICAL APPROACH 84

A11. SECTION Ac- NUMERICAL SIMULATIONS 84

A11.1 NUMERICAL APPROACH TO COMPUTE THE STRESS INTENSITY FACTOR 84
A11.2 FINITE ELEMENT MODELS AND RESULTS 84
A11.3 FINITE ELEMENT MODEL I-a 86
A11.4 FINITE ELEMENT MODEL I-b 87
A11.5 FINITE ELEMENT MODEL II-a 88
A11.6 FINITE ELEMENT MODEL II-b 89
A11.7 FINITE ELEMENT MODEL III-a 90
A11.8 FINITE ELEMENT MODEL III-b 91
A11.9 FINITE ELEMENT MODEL IV-a 92
A11.10 FINITE ELEMENT MODEL IV-b 93
A11.11 SUMMARY OF NUMERICAL RESULTS 94
A11.12 ADDITIONAL DISCUSSION ON TEST 07_104, TEST 07_140 AND TEST 07_164 94

LIST OF TABLES

Page

Table A-1: Mechanical Properties of Material....72
Table A-2: Computed Crack Driving Force for 07_09 Test....73
Table A-3: Computed Crack Driving Force from Detail FE Modeling....74

Table Ab-1: Stress Intensity Factors from Analytical Approach....84

Table Ac-1: Crack Driving Force from Numerical Approach....94

LIST OF FIGURES

Page

Figure A-1: Fuel Element Dimensions (mm) 71
Figure A-2: Loading Scheme from Experiment 72
Figure A-3: Stress Intensity Factors from Analytical and Numerical ('a' Type FE Models) Analyses 73
Figure A-4: Stress Intensity Factors from Analytical and Numerical ('b' Type FE Models) Analyses 74

Figure Aa-1: Fuel Element (Test 07_09) 77
Figure Aa-2: Detail View of the End of Fuel Element (Test 07_09) 78
Figure Aa-3: Out-of-Plane View of a Crack Test (07_09) 79
Figure Aa-4: Crack-Plane View of a Crack (Test 07_09)....80

Figure Ab-1: Notation for Erdogan and Tada Solution....81
Figure Ab-2: Notation for Benthem Solution....83

Figure Ac-1: Finite Element Model of a Fuel Bundle Element with a Circumferential Crack (Model I-a)....86
Figure Ac-2: Opening/Closing Stress Component (MPa) (Model I-a) 86
Figure Ac-3: Finite Element Model of a Portion of the Endplate Attached to the Endcap/Endplate Weld (Model I-b, See Figure Ac-7 for an Overall Picture of This Area Including the Fuel Element)....87
Figure Ac-4: Opening/Closing Stress Component (MPa) (Model I-b) 87
Figure Ac-5: Finite Element Model of a Fuel Bundle Element with a Circumferential Crack (Model II-a)....88
Figure Ac-6: Opening/Closing Stress Component (MPa) (Model II-a) 88
Figure Ac-7: Finite Element Model of a Fuel Bundle Element with a Circumferential Crack (Model II-b)....89
Figure Ac-8: Opening/Closing Stress Component (MPa) (Model II-b) 89
Figure Ac-9: Finite Element Model of a Fuel Bundle Element with a Circumferential Crack (Model III-a)....90
Figure Ac-10: Opening/Closing Stress Component (MPa) (Model III-a) 90
Figure Ac-11: Finite Element Model of a Fuel Bundle Element with a Circumferential Crack (Model III-b)....91
Figure Ac-12: Opening/Closing Stress Component (MPa) (Model III-b) 91

Figure Ac-13: Finite Element Model of a Fuel Bundle Element with a Circumferential Crack (Model IV-a) 92
Figure Ac-14: Opening/Closing Stress Component (MPa) (Model IV-a)....92
Figure Ac-15: Finite Element Model of a Fuel Bundle Element with a Circumferential Crack (Model IV-b) 93
Figure Ac-16: Opening/Closing Stress Component (MPa) (Model IV-b)....93

ABBREVIATIONS

DHC - Delayed Hydride Cracking
FEM - Finite Element Method
FE - Finite Element

NOMENCLATURE

D_o - diameter of fuel bundle element at the end-cap
D_B - maximum diameter of fuel bundle element
e - maximum distance from neutral axis to extreme elements
E - Young's modulus
I - moment of inertia
J - J-integral
K - stress intensity factor
K_I - mode I stress intensity factor
L - loading arm
M - bending moment
P - force
S - section moduli
T - shearing force
v - Poisson's ratio

UNITS

Force - N
Dimensions- mm
Stress - MPa

A1. INTRODUCTION

The susceptibility to delayed hydride cracking of unirradiated CANDU fuel bundle endplate/endcap welds has been investigated experimentally at Kinectrics Inc. An increasing loading test was performed to find the resistance of the Zircaloy endplate-to-endcap assembly to DHC crack initiation. This Appendix describes the stress analysis methodology to determine the applied stress intensity factor K_I at DHC initiation. Several numerical and analytical approaches were applied to achieve this goal.

A2. GEOMETRY OF A FUEL BUNDLE ELEMENT

The geometry of the fuel bundle element endcap/endplate region provided by Seahra (2007) is shown in Figure A-1. More detailed information on geometry, initial and final crack dimensions is provided in Section A9 (Appendix Aa).

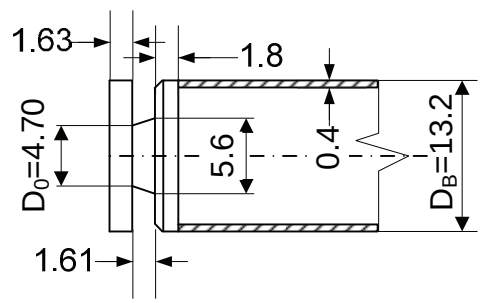

Figure A-1: Fuel Element Dimensions (mm)

The following parameters were derived using specific geometry of the fuel element:

$$I = \frac{\pi D_0^4}{64} = 23.95 \text{ [mm}^4\text{]}$$

$$e = \frac{D_0}{2} = 2.35 \text{ [mm]}$$

$$S = \frac{I}{e} = 10.19 \text{ [mm}^3\text{]}$$

A3. APPLIED LOADING

Force *P* was applied at a distance *L* from a circumferential crack (noted by point A). The loading scheme is illustrated in Figure A-2.

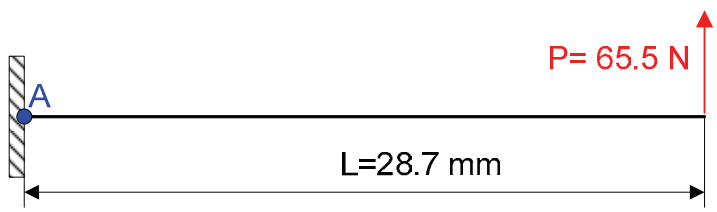

Figure A-2: Loading Scheme from Experiment

Seahra (2007) reported that the force at crack initiation was 65.5 N. The applied bending moment at point *A* was:

$$M^A = PL = 1879.9 \text{ [N mm]}$$

The maximum bending stress at the crack-free cross-section was:

$$\sigma_b = \frac{M^A}{S} = 184.3 \text{ [N/mm}^2\text{]} = 184.3 \text{ [MPa]}$$

A4. MATERIAL PROPERTIES

Numerical simulations were performed using material properties shown in Table A-1. Linear elastic material response was assumed.

Table A-1: Mechanical Properties of Material

Young's Modulus	Poisson's Ratio
94,500 MPa	0.4

A5. RESULTS

The crack driving forces in terms of K_I and J were computed using analytical (see Section A10: Appendix A) and numerical approaches (see Section A11: Appendix Ac). Table A-2 and A-3 show results obtained from type 'a' and 'b' finite element models respectively. Figures A-3 and A-4 compare results in bar-type plots.

Table A-2: Computed Crack Driving Force for 07_09 Test

Solution	J [N/mm]	K_I [MPa√m]
Analytical – Method I	-	10.0
Analytical – Method II	-	10.4
Numerical – Model I-a	0.887	10.0
Numerical – Model II-a	0.893	10.0
Numerical – Model III-a	0.962	10.4
Numerical – Model IV-a	0.962	10.4

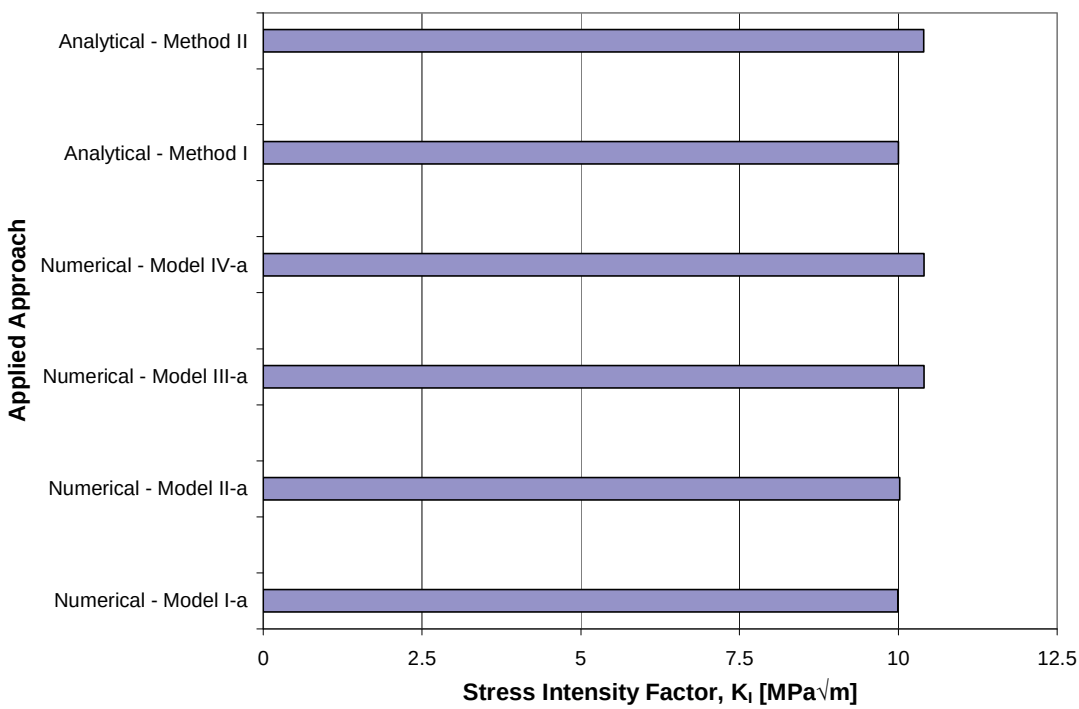

Figure A-3: Stress Intensity Factors from Analytical and Numerical ('a' Type FE Models) Analyses

Table A-3: Computed Crack Driving Force from Detail FE Modeling

FE Model	J [N/mm]	K_I [MPa√m]
Model I-a	0.887	10.0
Model I-b	0.538	7.8
Model II-a	0.893	10.0
Model II-b	0.543	7.8
Model III-a	0.962	10.4
Model III-b	0.610	8.3
Model IV-a	0.962	10.4
Model IV-b	0.575	8.0

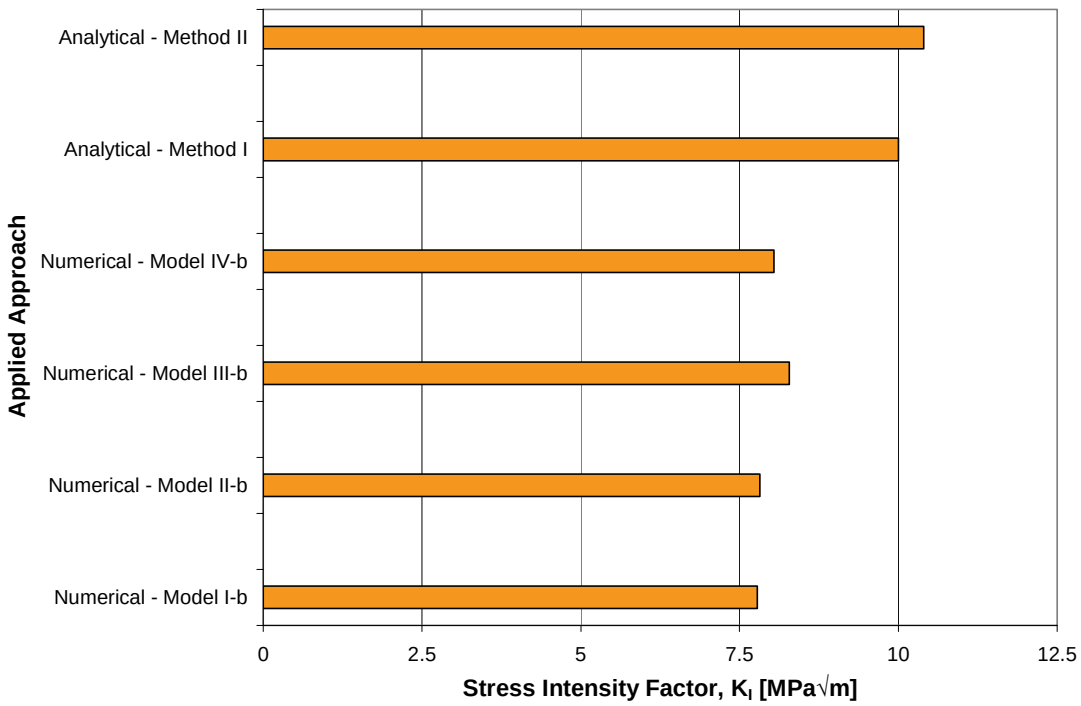

Figure A-4: Stress Intensity Factors from Analytical and Numerical ('b' Type FE Models) Analyses

A6. CONCLUSIONS

(a) Numerical and analytical analyses were performed in order to determine the stress intensity factor for crack initiation during 07_09 test.

(b) Computed stress intensity factors from type ‘a’ FE models were higher than those from type ‘b’ models.

(c) The stress intensity factors from analytical and from numerical type ‘a’ FE models were consistent.

(d) The stress intensity factors from type ‘b’ finite element models were lower than from the analytical approach.

(e) Based on performed computations, the stress intensity factor for crack initiation in 07_09 test was estimated to be 8.3 MPa√m as obtained with Model III-b.

A7. RECOMMENDATIONS

(a) Expand complexity by more detailed modeling of fuel element geometry and including crack contact/closure caused by the compressive bending stress.

(b) Compute crack driving force using elastic-plastic fracture mechanics approach.

A8. REFERENCES

Benthem, J.P. and W.T. Koiter. 1972. Asymptotic approximations to crack problems, Methods of Analysis of Crack Problems. Edited by Sih, G.C., Noordhoff International Publishing.

DeLorenzi, H.G. 1982. Energy release rate calculations by the finite element method, General Electric Technical Information Series. Report No. 82CRD205.

Erdogan, F. 1982. Theoretical and experimental study of fracture in pipelines containing circumferential flaws. U.S. Department of Transportation, DOT-RSPA-DMA, 50/83/3.

Gellerud, A., K. Koppenhoefer, A. Roy, S. Roychowdhury, M. Walters, B. Bichon, K. Cochran, A. Carlyle, and R.H. Dodds Jr. April 2007. WARP3D-release 15.8: 3-D dynamic nonlinear fracture analysis of solids using parallel computers and workstations. User’s Manual.

Hutchinson, J.W. 1968. Singular behavior at the end of a tensile crack in a hardening material. J. Mech. Phys. Solids, 16, 13-31.

Parks, D.M. 1977. The virtual crack extension method for nonlinear material behavior. Computer Methods in Applied Mechanics and Engineering, 12, 353-364.

Parks, D.M. 1978. Virtual crack extension – a general finite element technique for J-integral evaluation, Proc. 1st Int. Conf Numerical Methods in Fracture Mechanics. Swansea, UK, pp. 464-478.

Rice, J.R. and G.F. Rosengren. 1968. Plane strain deformation near a crack tip in a power-law hardening material. J. Mech. Phys. Solids, 16, 1-12.

Seahra, H. May 2007. Private communication.

Tada, H., P.C. Paris and G.R. Irwin. 1985. The stress analysis of cracks handbook, 2nd ed., Paris Productions Incorporated (and Del Research Corporation). St. Louis, MO.

A9. SECTION Aa-FUEL PENCIL FROM 07_09 TEST

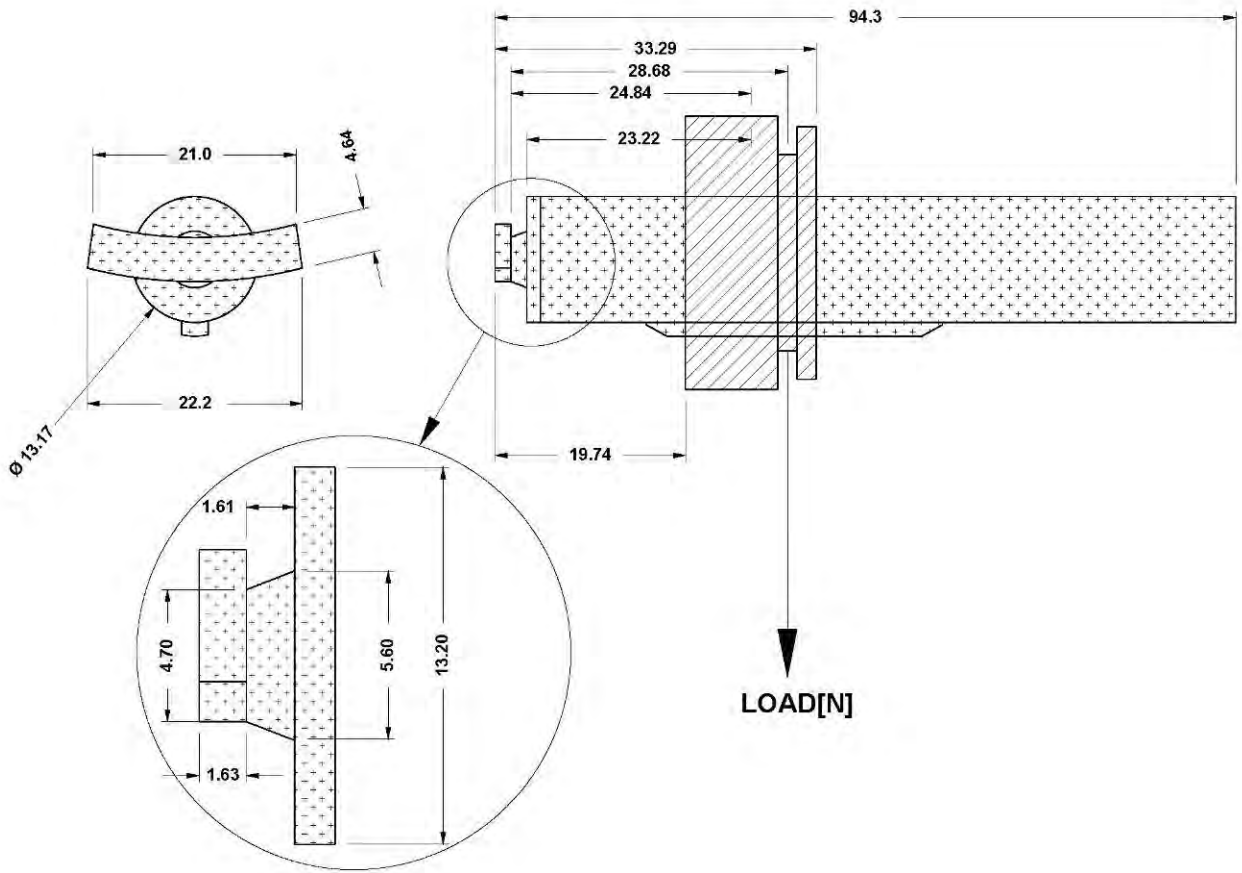

Figure Aa-1: Fuel Element (Test 07_09)

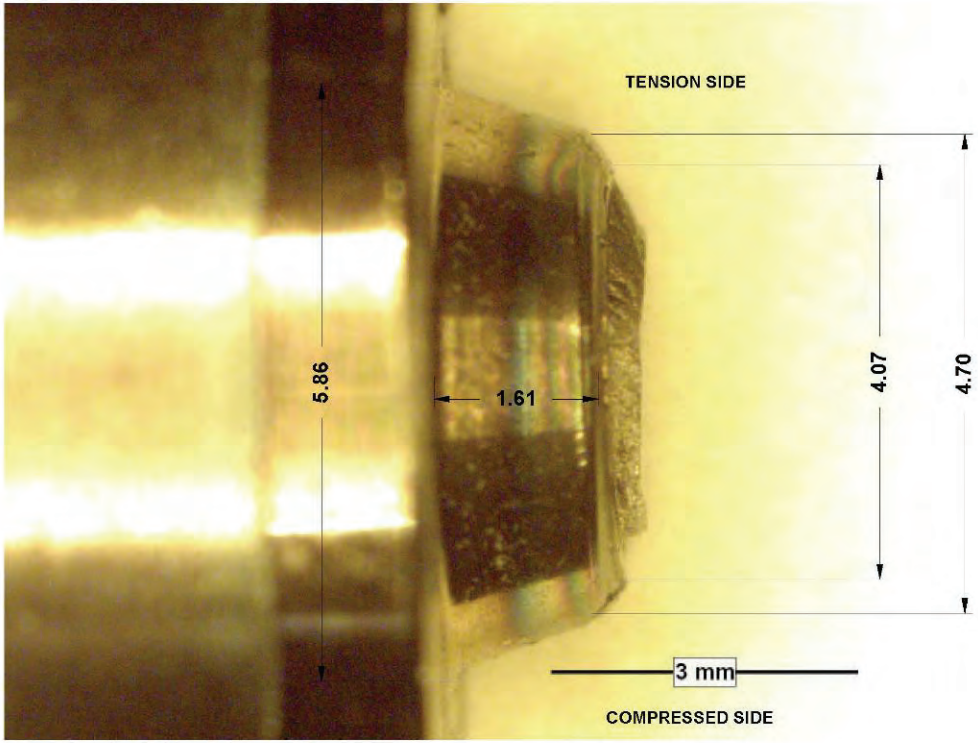

Figure Aa-2: Detail View of the End of Fuel Element (Test 07_09)

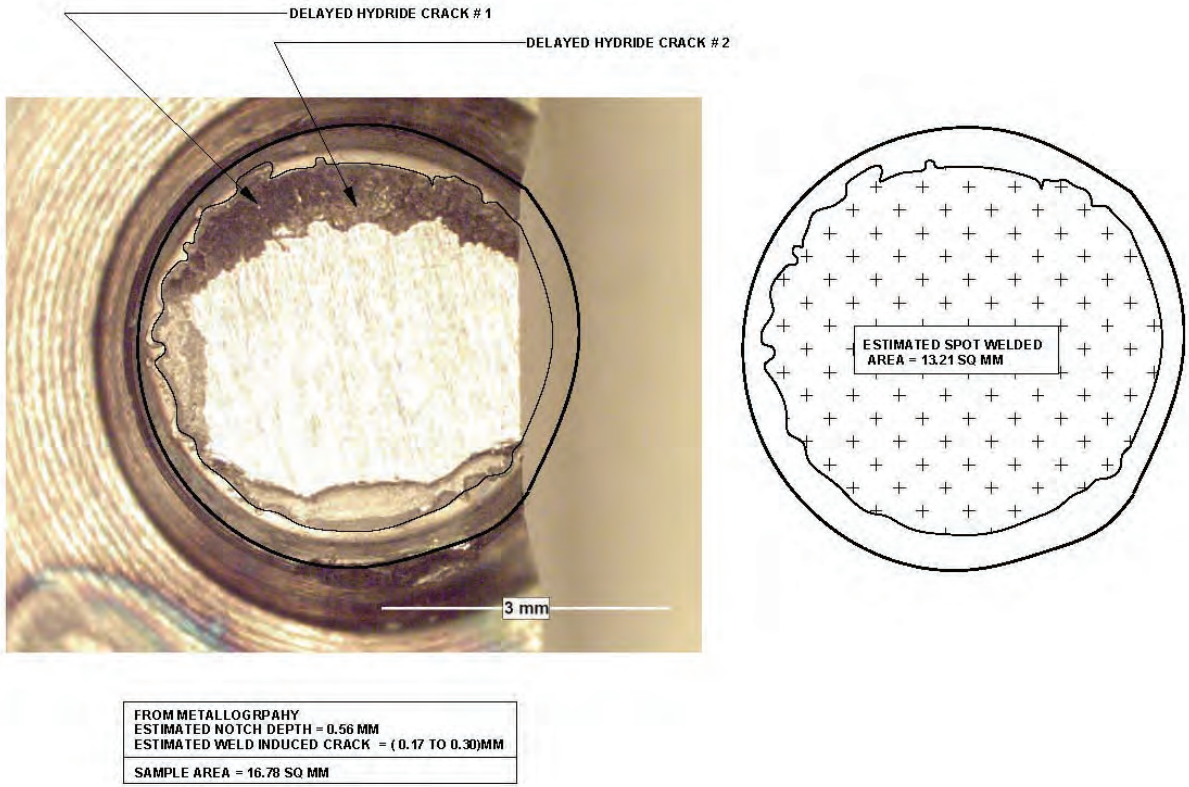

Figure Aa-3: Out-of-Plane View of a Crack Test (07_09)

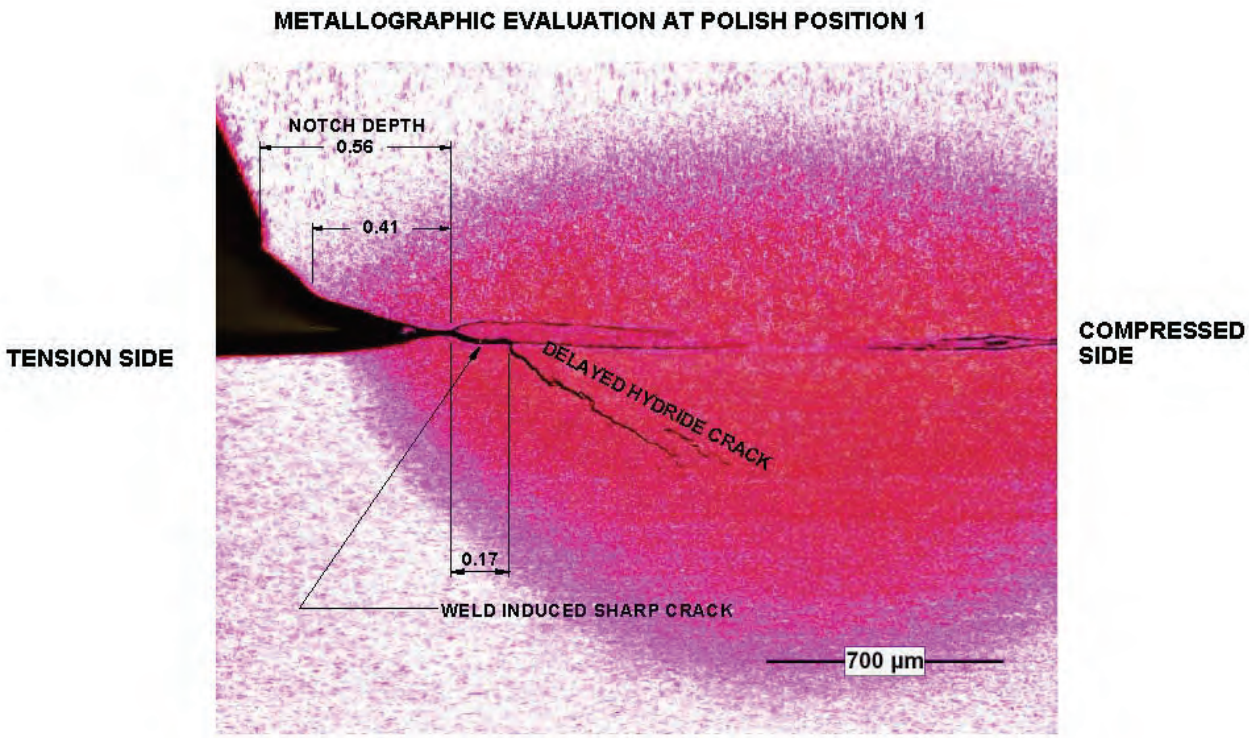

Figure Aa-4: Crack-Plane View of a Crack (Test 07_09)

A10. SECTION Ab - ANALYTICAL APPROACH TO COMPUTE THE STRESS INTENSITY FACTOR

A10.1 ERDOGAN AND TADA SOLUTION (METHOD I)

Erdogan (1982) and Tada et al. (1985) solution (noted further as Method I) for a rod with a fully circumferential crack (see Figure Ab-1) under bending was used to determine the stress intensity factor,

$$K_I = \sigma_b \sqrt{\pi c} F \qquad \text{(Ab-1)}$$

where *F* is a geometry correction factor expressed as

$$F = \frac{1}{\left(1-\frac{c}{b}\right)^{\frac{5}{2}}}\left(0.563 - 0.188\frac{c}{b} + \left(1-\frac{c}{b}\right)^2\left(0.559 - 1.47\frac{c}{b} + 2.72\left(\frac{c}{b}\right)^2 - 2.40\left(\frac{c}{b}\right)^3\right)\right) \qquad \text{(Ab-2)}$$

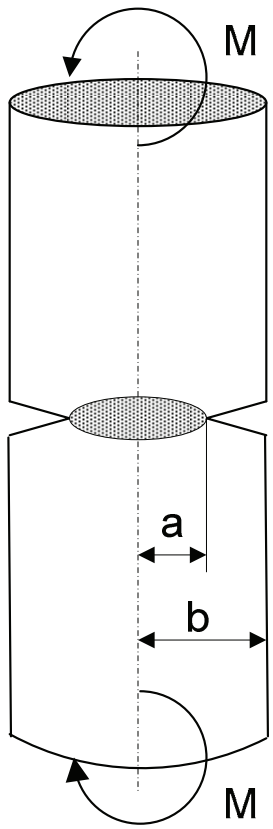

Figure Ab-1: Notation for Erdogan and Tada Solution

A10.2 COMPUTED STRESS INTENSITY FACTOR FOR 07_09 TEST

$c = 0.51$ [mm]

$\sigma_b = \frac{M^A}{S}$ =184.3 [N/mm^2] = 184.3 [MPa]

$F = 1.3509$

$K_I = \sigma_b \sqrt{\pi c 10^{-3}} F$

Computed

$K_I =$ 10.0 [MPa√m]

A10.3 BENTHEM SOLUTION (METHOD II)

Second analytical solution used to determine stress intensity factor was provided by Benthem et al. (1972) (see Figure Ab-2 for notation).

$$K_1 = \sigma_{bN} \sqrt{\pi (b-a)} F_2 \qquad \text{(Ab-3)}$$

where

$$\sigma_{bN} = \frac{4\mathrm{M}}{\pi a^3} \qquad \text{(Ab-4)}$$

F_2 is geometry correction factor expressed as

$$F_2 = G\sqrt{\frac{a}{b}} \qquad \text{(Ab-5)}$$

where

$$G = \frac{3}{8}\left(1.0 + \frac{1}{2}\frac{a}{b} + \frac{3}{8}\left(\frac{a}{b}\right)^2 + \frac{5}{16}\left(\frac{a}{b}\right)^3 + \frac{35}{128}\left(\frac{a}{b}\right)^4 + 0.537\left(\frac{a}{b}\right)^5\right) \qquad \text{(Ab-6)}$$

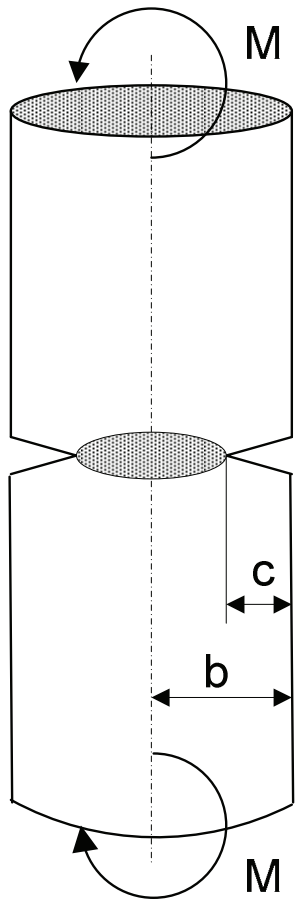

Figure Ab-2: Notation for Benthem Solution

A10.4 COMPUTED STRESS INTENSITY FACTOR FOR 07_09 TEST

$b = 2.35$ [mm]

$a = 1.84$ [mm]

$\sigma_{bN} = 383.9$ [MPa]

$F_2 = 0.6743$

$$K_1 = \sigma_{bN}\sqrt{\pi(b-a)10^{-3}}F_2$$

Computed:

$K_I = 10.4$ [MPa√m]

A10.5 SUMMARY OF RESULTS FROM THE ANALYTICAL APPROACH

The stress intensity factors for 07_09 test were computed using the analytical approach and they are documented in Table Ab-1. Bentham et al. (1972) solution produced higher stress intensity factors than Erdogan (1982) and Tada at al. (1985) solutions.

Table Ab-1: Stress Intensity Factors from Analytical Approach

Solution	K_I [MPa√m]
Method I (Erdogan and Tada)	10.0
Method II (Benthem)	10.4

A11. SECTION Ac- NUMERICAL SIMULATIONS

A11.1 NUMERICAL APPROACH TO COMPUTE THE STRESS INTENSITY FACTOR

Finite element computations were performed using WARP3D 15.8 (2007) with small displacement formulation for elements. Applied loading followed the experimental setup. J-integral was computed using domain integration procedure implemented in WARP3D (2007). Stress intensity factor, K_I, was obtained after applying plain strain conversion of J-integral:

$$K_I = \sqrt{\frac{E\,J}{1-\nu^2}} \qquad \text{(Ac-1)}$$

where *E* was Young's modulus and *v* was Poisson's ratio. For more information on J-integral and numerical methodologies used see the following references: Hutchinson (1968), Rice et al. (1968), Parks (1977), Parks (1978) and DeLorenzi (1982).

A11.2 FINITE ELEMENT MODELS AND RESULTS

Finite element modeling was performed for half length of the fuel bundle element due to existing symmetry. The three-dimensional FE models were developed using 20-node hexahedral solid model elements. The crack core region was modeled using twenty focused rings. Two approaches were applied to modeling the end of the fuel bundle element. In a simplified approach, rigid boundary conditions were applied at the end of the fuel element. These models were labelled 'a', e.g. model I-a. In a more detailed approach, modeling of the endplate was also included. The curvature of the end plate was not modeled at this stage. The applied boundary conditions followed the experimental setup by Seahra (2007). These models used label 'b', e.g. model I-b. More detailed information on the developed meshes, applied boundary conditions and obtained stresses is provided in Figures Ac-1 through Ac-16.

The elastic solution for the stress field at a planar crack shows a singularity at the crack tip and the stresses increase to infinity. However, in real materials, the area at the crack tip is plastically deformed and stresses are finite.

A11.3 FINITE ELEMENT MODEL I-a

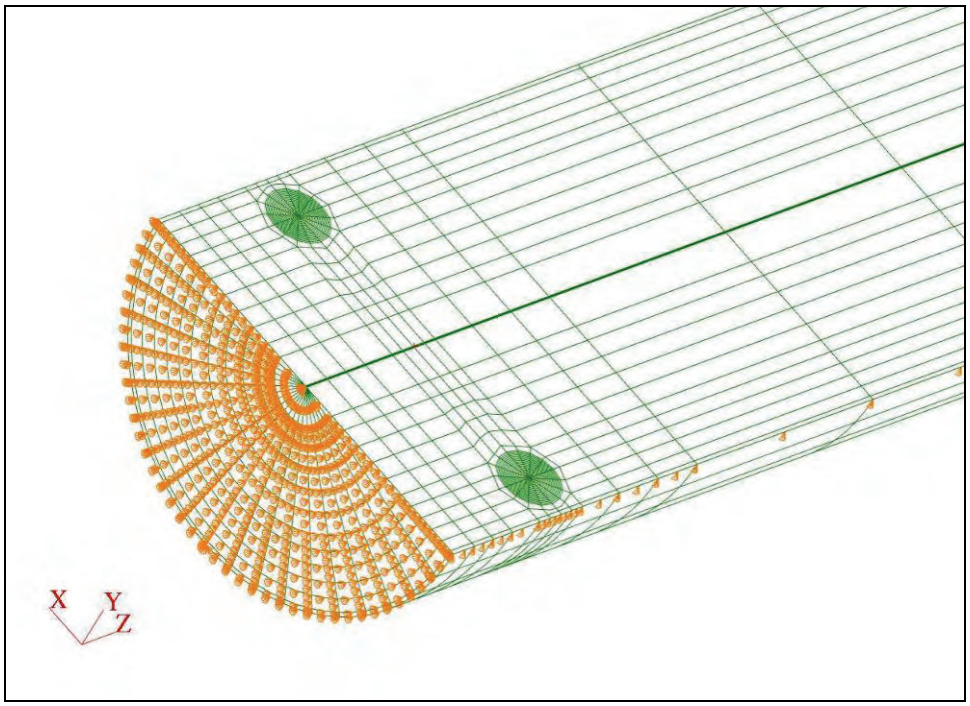

Figure Ac-1: Finite Element Model of a Fuel Bundle Element with a Circumferential Crack (Model I-a)

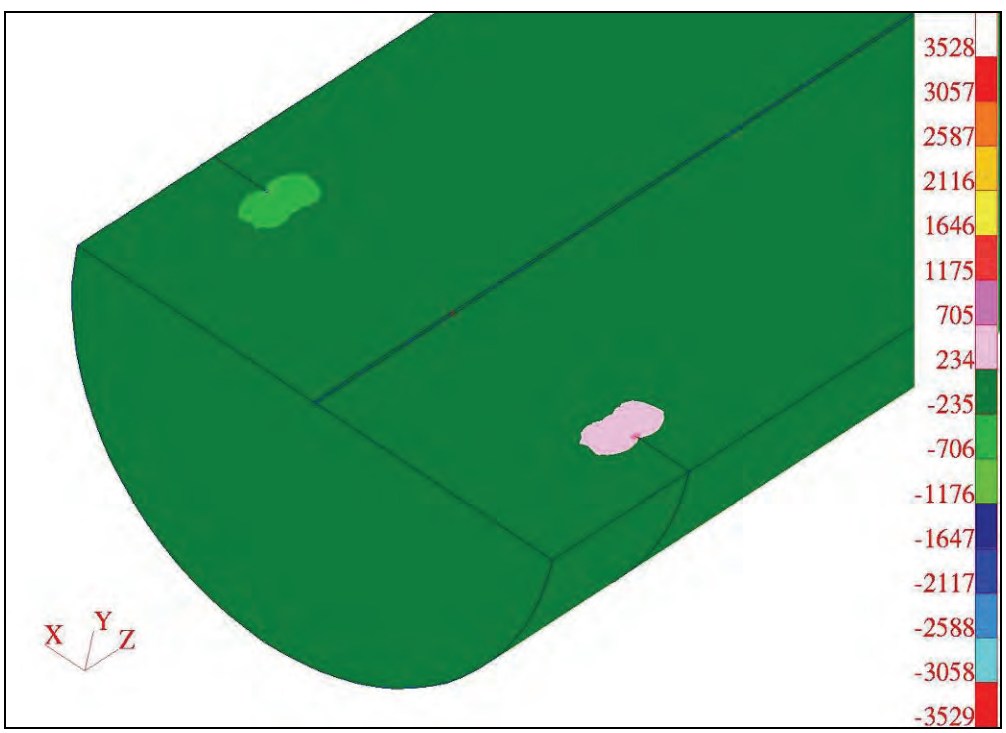

Figure Ac-2: Opening/Closing Stress Component (MPa) (Model I-a)

A11.4 FINITE ELEMENT MODEL I-b

The fixed displacements (shown in orange colour in Fig. Ac-3) were applied to two side edge surfaces of the end plate portion attached to the fuel element endcap. Symmetry boundary conditions were applied at the symmetry plane of the fuel bundle element (XZ-plane at Figure Ac-3)

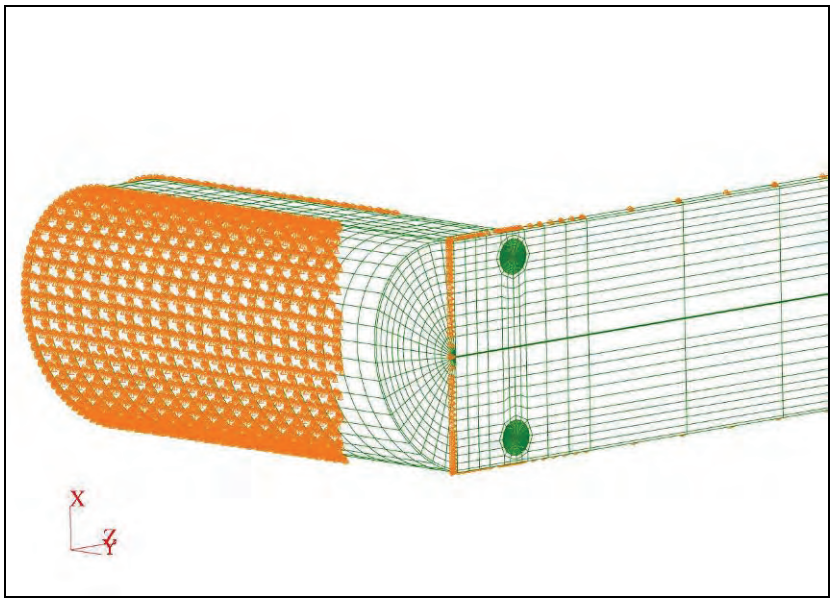

Figure Ac-3: Finite Element Model of a Portion of the Endplate Attached to the Endcap/Endplate Weld (Model I-b, See Figure Ac-7 for an Overall Picture of This Area Including the Fuel Element)

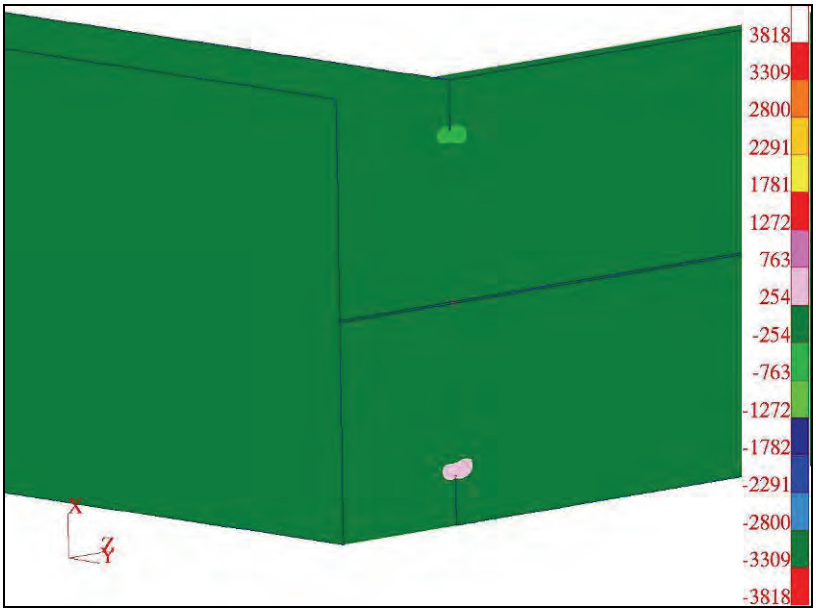

Figure Ac-4: Opening/Closing Stress Component (MPa) (Model I-b)

A11.5 FINITE ELEMENT MODEL II-a

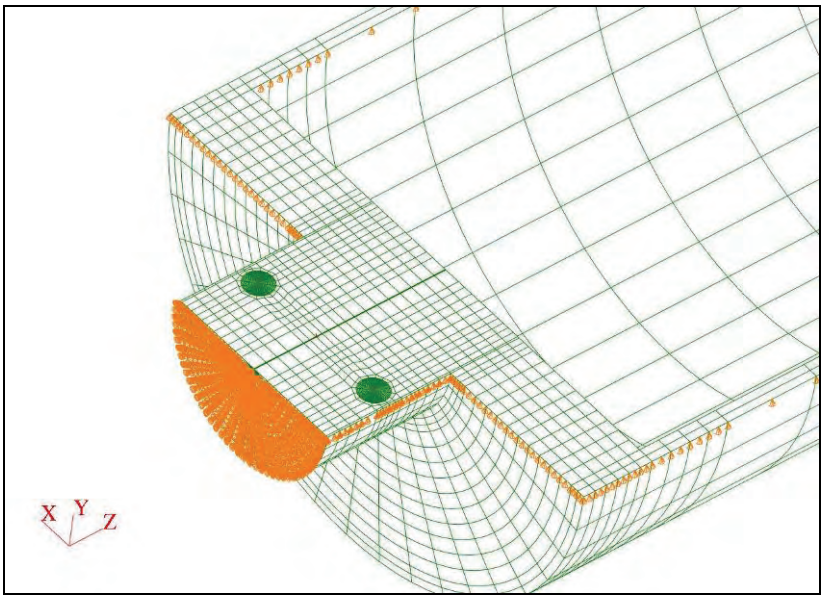

Figure Ac-5: Finite Element Model of a Fuel Bundle Element with a Circumferential Crack (Model II-a)

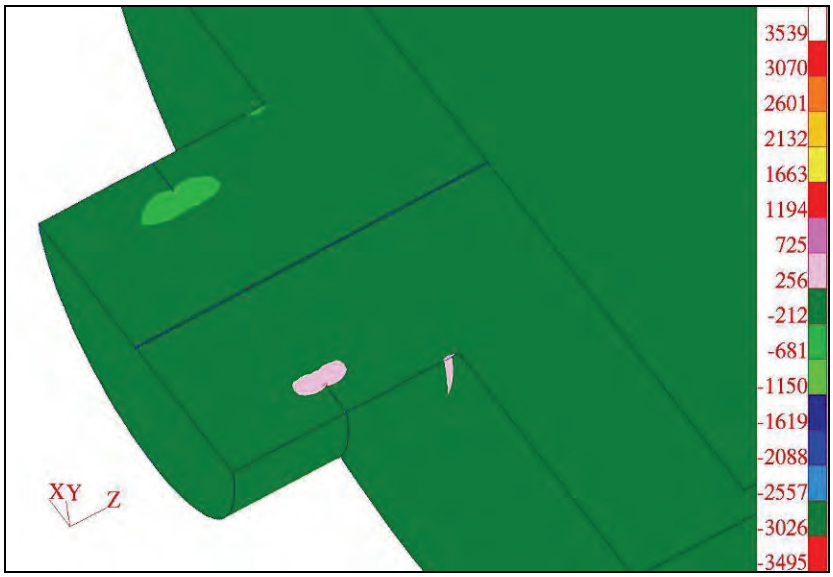

Figure Ac-6: Opening/Closing Stress Component (MPa) (Model II-a)

A11.6 FINITE ELEMENT MODEL II-b

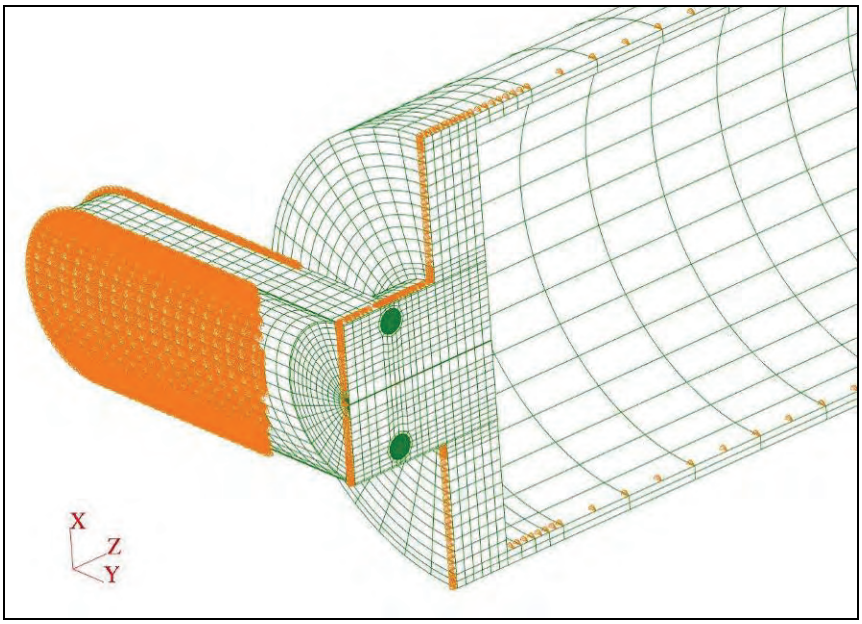

Figure Ac-7: Finite Element Model of a Fuel Bundle Element with a Circumferential Crack (Model II-b)

Figure Ac-8: Opening/Closing Stress Component (MPa) (Model II-b)

A11.7 FINITE ELEMENT MODEL III-a

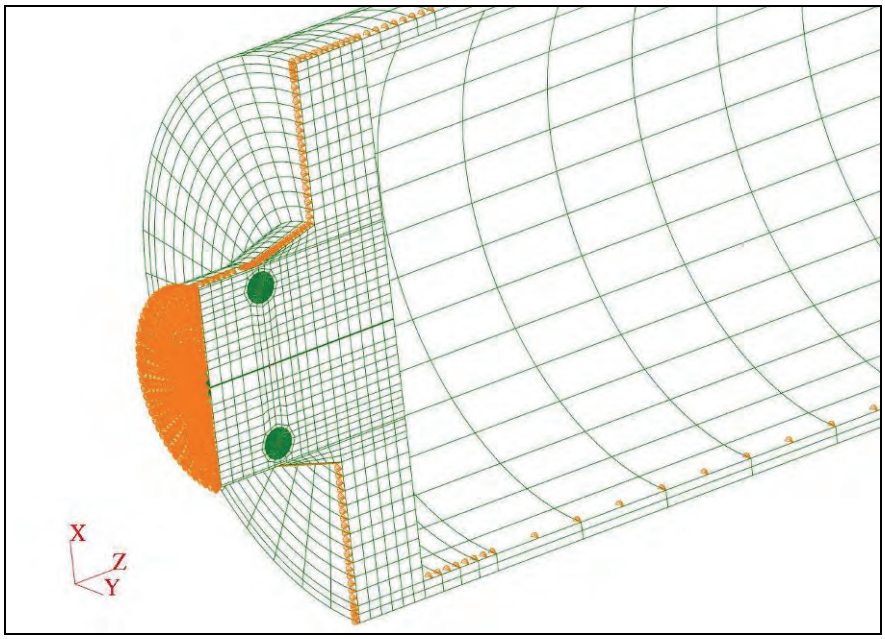

Figure Ac-9: Finite Element Model of a Fuel Bundle Element with a Circumferential Crack (Model III-a)

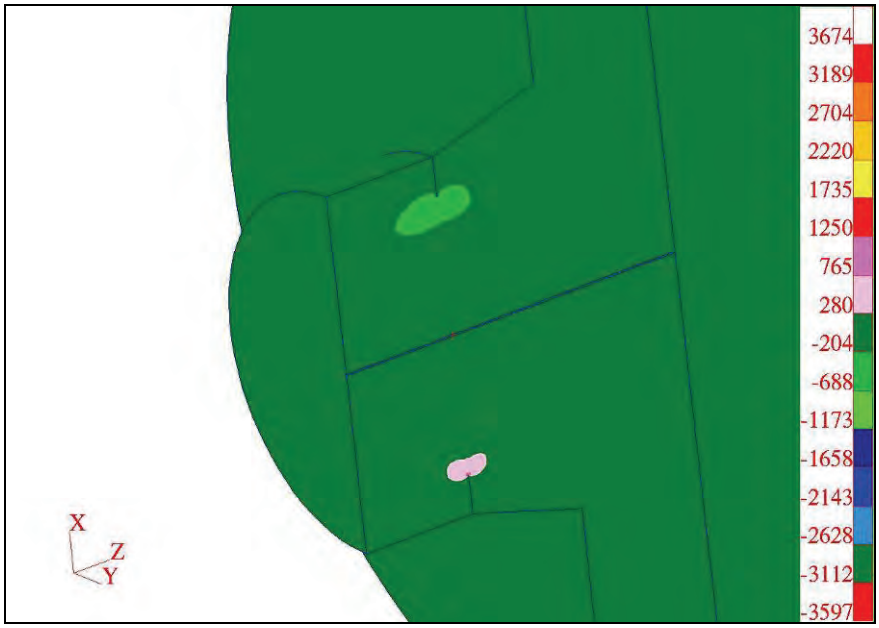

Figure Ac-10: Opening/Closing Stress Component (MPa) (Model III-a)

A11.8 FINITE ELEMENT MODEL III-b

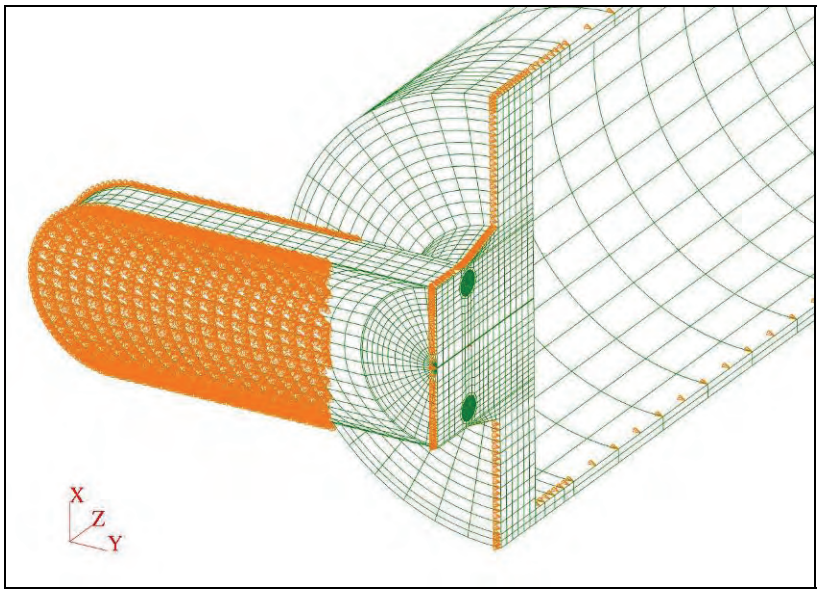

Figure Ac-11: Finite Element Model of a Fuel Bundle Element with a Circumferential Crack (Model III-b)

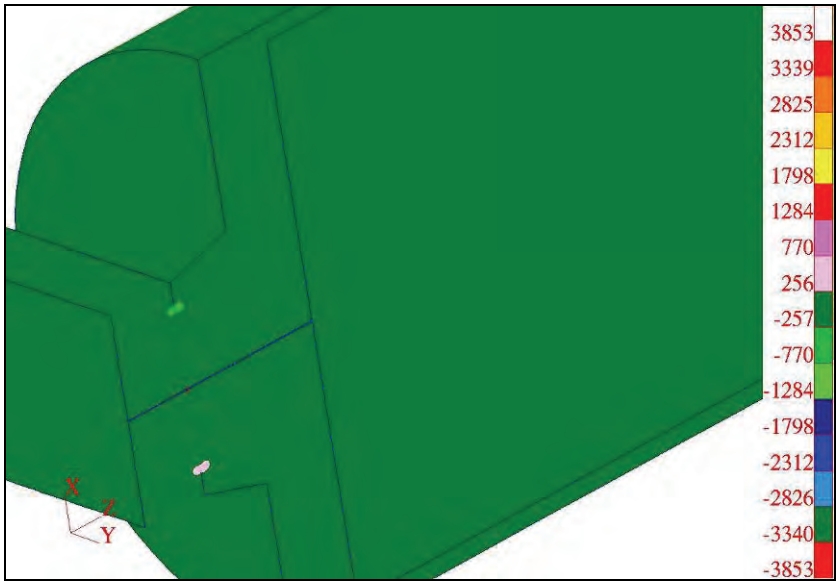

Figure Ac-12: Opening/Closing Stress Component (MPa) (Model III-b)

A11.9 FINITE ELEMENT MODEL IV-a

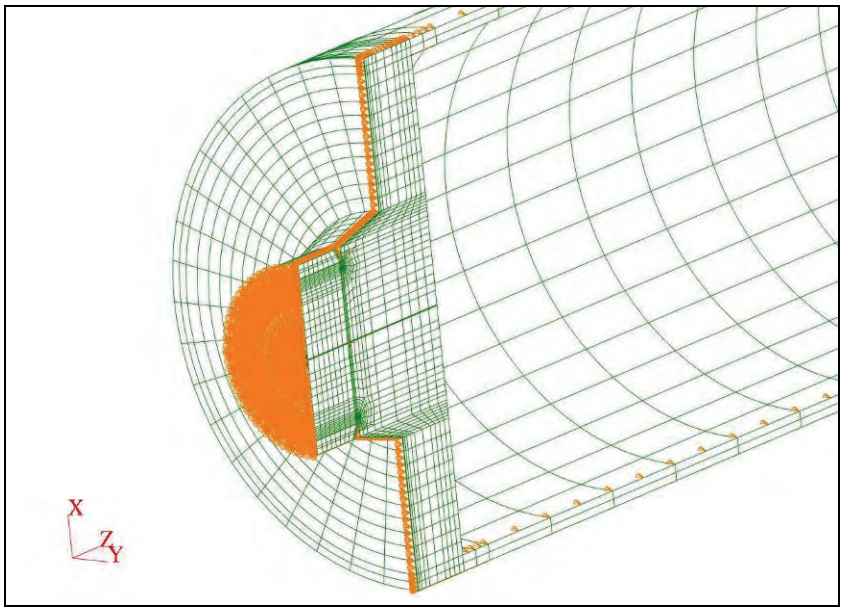

Figure Ac-13: Finite Element Model of a Fuel Bundle Element with a Circumferential Crack (Model IV-a)

Figure Ac-14: Opening/Closing Stress Component (MPa) (Model IV-a)

A11.10 FINITE ELEMENT MODEL IV-b

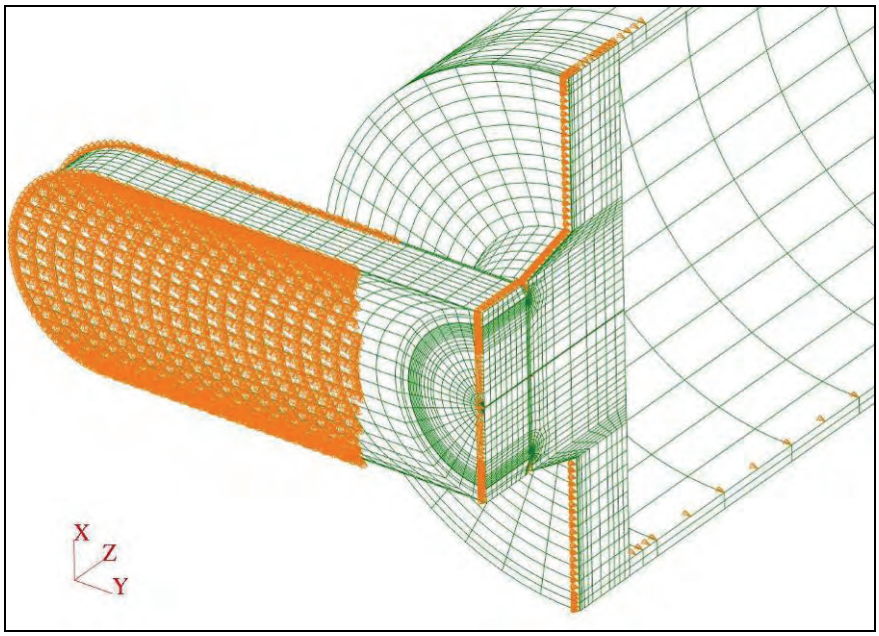

Figure Ac-15: Finite Element Model of a Fuel Bundle Element with a Circumferential Crack (Model IV-b)

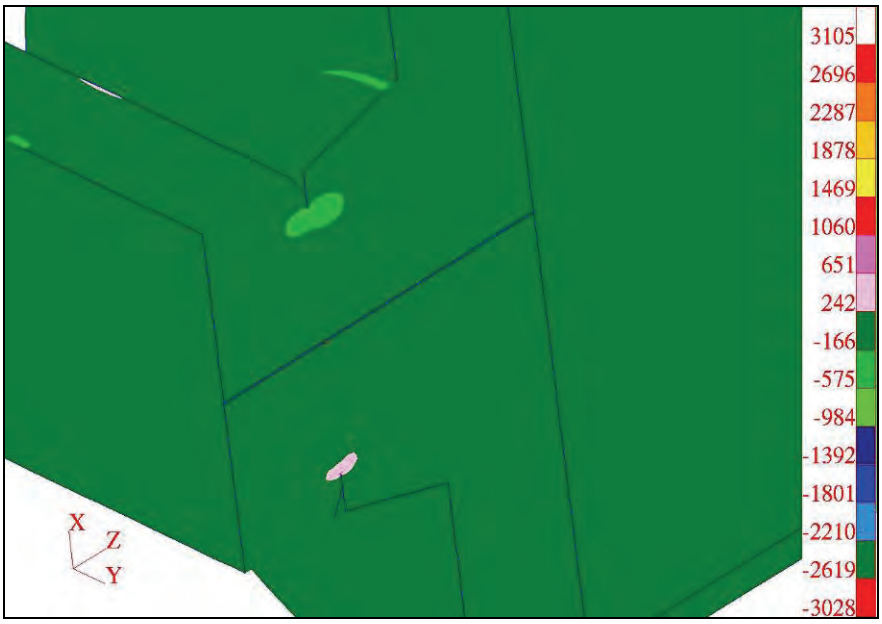

Figure Ac-16: Opening/Closing Stress Component (MPa) (Model IV-b)

A11.11 SUMMARY OF NUMERICAL RESULTS

Table Ac-1 presents computed crack driving forces from finite element models in terms of stress intensity factors and J-integrals. The highest stress intensity factor was 10.4 MPa√m obtained from Model III-a and IV-a. The lowest stress intensity factor, 7.8 MPa√m, was computed from Model I-b and II-b. The maximum difference in the computed stress intensity factors was 2.6 MPa√m. However, if only results from type 'a' or 'b' models are compared, then this difference is considerably smaller. The general trend is that the stress intensity factors from type 'a' models were higher than from type 'b' models. Since type 'b' models were more detailed and closer to the experimental setup, they should be used to determine the applied K_I in the experiments. Another observation is that stress intensity factors computed from Models III and IV type are very similar.

Table Ac-1: Crack Driving Force from Numerical Approach

FE Model	J [N/mm]	K_I [MPa√m]
Model I-a	0.887	10.0
Model I-b	0.538	7.8
Model II-a	0.893	10.0
Model II-b	0.543	7.8
Model III-a	0.962	10.4
Model III-b	0.610	8.3
Model IV-a	0.962	10.4
Model IV-b	0.575	8.0

A11.12 ADDITIONAL DISCUSSION ON TEST 07_104, TEST 07_140 AND TEST 07_164

Additional numerical simulations were conducted in order to determine the applied stress intensity factors at DHC initiation for tests 07_104, 07_140 and 07_164. The applied loading force at DHC initiation was 62 N for all these tests. For Tests 07_104 and 07_140, the initial crack depth was about 0.5 mm. For Test, 07_164, the crack depth was significantly larger at 0.85 mm.

The differences in crack depth under the same applied load resulted in a significant difference in the computed stress intensity factors. They were 7.9 MPa√m and 7.6 MPa√m for Test 07_104 and 07_140, respectively, and 13.6 MPa√m for Test 07_164 test. This difference may might be the result of several factors. One of them is variability in microstructure of the welded material throughout the cross-section. Another is a significant ovalization of the cross-section of the end-cap as in the sample from Test 07_164 which led to a stress redistribution that was not taken into account in the current finite element models. The models assumed a circular cross-section of the end-cap at the crack plane. The effect of plasticity, notch geometry and crack closure at the compressive side should also be considered. An assessment of the factors leading to the higher than expected differences in the estimated stress intensity factors for DHC initiation could be undertaken.